Student thesis series INES no. 295

Snowmelt and Runoff Assessment of Talas River Basin Using Remote Sensing Approach

Hammad Javid

2014
Department of
Physical Geography and Ecosystem Science
Lund University
Sölvegatan 12
S-223 62 Lund
Sweden

Hammad Javid (2014)
Snowmelt and Runoff Assessment of Talas River Basin Using Remote Sensing Approach
Master degree thesis, 30 credits in *Physical Geography and Ecosystem Analysis*
Department of Physical Geography and Ecosystem Science, Lund University

Snowmelt and Runoff Assessment of Talas River Basin Using Remote Sensing Approach

Hammad Javid
Master Degree Thesis, 30 Credits
M.Sc Physical Geography and Ecosystem Analysis
January 2014

Supervisors

Wolfgang Kinzelbach
Head of Groundwater & Hydromechanics Chair, Institute of Environmental Engineering, ETH Zurich

Tobias Siegfried
Hydrosolutions GmbH, Zurich. Affiliate: Center for Comparative and International Studies, ETH Zurich

Simone Fatichi
Chair of Hydrology & Water Resources Management, ETH Zurich

Haijing Wang
Hydrosolutions GmbH, Zurich. Affiliate: Institute of Environmental Engineering, ETH Zurich

Andreas Persson
Centre for Geographical Information Systems (GIS Centre), Department of Physical Geography and Ecosystem Science, Lund University

Department of Physical Geography and Ecosystem Science
Lund University, Sweden

Department of Civil, Environmental and Geomatic Engineering
Swiss Federal Institute of Technology, ETH Zurich

In the name of ALLAH, the Most Beneficent, the Most Merciful.

Contents

List of Figures

List of Tables

Abbreviations

AVHRR	Advanced Very High Resolution Radiometer
BIL	Band interleaved by line
CARs	Central Asian Republics
CT	Cloud Transmissivity
CTWC	Chu Talas Water Commission
CFC	Cloud Fractional Cover
CM	Climate Monitoring
CMORPH	CPC MORPHing
DEM	Digital Elevation Map
DWD	Deutscher Wetterdienst
ESA	European Space Agency
EOS	Earth Observing System
ESBN	European Soil Bureau Network
EUMETSAT	European Organization for the Exploitation of Meteorological Satellites
FAO	Food and Agriculture Organization
GHCN	Global Historical Climatology Network
GOES	Geostationary Operational Environmental Satellites
GPCC	Global Precipitation Climatology Center
GPCC FD	GPCC Full Data Reanalysis
GTS	Global Telecommunication System
HKH	Hindu Kush-Karakoram-Himalaya region
HWSD	Harmonized World Soil Database
IIASA	International Institute for Applied System Analysis
LCCS	United Nations Land Cover Classification System
LUC	Land Use Change and Agriculture Program
MERIS	Medium Resolution Imaging Spectrometer Instrument
MODIS	Moderate Resolution Imaging Spectroradiometer

NASDA	National Space Development Agency
NASA	National Aeronautics and Space Administration
NSIDC	National Snow and Ice Data Center
NDSI	Normalized Difference Snow Index
NMHS	National Meteorological and Hydrological Services
PCHIP	Piecewise Cubic Hermite Interpolating Polynomial
PR	Precipitation Radar
PMW	Passive MicroWave
SAF	Satellite Application Facility
SOTER	Global and National Soils and Terrain Digital Databases
SPEs	Satellite Precipitation Estimates
SYNOP	Surface sYNoptic Observations
TMI	TRMM Microwave Imager
TOPKAPI	Topographic Kinematic APproximation and Integration model
TRMM	Tropical Rainfall Measuring Mission
WISE	World Inventory of Soil Emission Potential

Abstract

Transboundary river basins provide inhabitance and water resources to millions of people around the globe and they are a source of dispute among neighbor countries also. This thesis focuses on the snow melt and runoff modeling of a small transboundary river, Talas; using a physically distributed rainfall-runoff model, TOPKAPI-ETH. Investigation on the use of remotely sensed precipitation estimates and MODIS snow cover images shows that they can be a key to model snowmelt and water resources of remote and un-gauged catchments. However the need of observed precipitation data from different regions and elevation zones of the basin is vital in generating the runoff with higher accuracy. Annual runoff prediction strategies from snow cover area is also proposed which can be of great help in efficient management of water resources and hence in resolving conflict between the riparian countries, Kyrgyzstan and Kazakhstan.

Keywords: *Talas River, Remotely Sensed Precipitation, TRMM, GPCC, MODIS, Chu-Talas River Basin, Transboundary Rivers, Central Asia.*

Chapter 1

1. Introduction

Transboundary waters play a key role in supporting life of millions of people in Europe, Central Asia, South Asia and Africa. Transboundary basins provide inhabitance to more than 50 % of population (approximately 460 million people) and occupy more than 40 % of surface of the European and Asian UNECE region[1] only (UNECE 2011). The five Central Asian Republics (CARs) have since independence been facing dispute about transboundary waters division. The upstream countries Kyrgyzstan and Tajikistan want to use water in winter for producing hydroelectric power. This sometime causes floods in the downstream countries and scarcity of water for irrigation when it is badly needed in the summer. During Soviet rule, the upstream countries were provided energy by central government and water was stored in dams for use in the later part of the year (Libert and Lipponen 2012). In order to meet the continually increasing demand of cotton or 'White Gold' by the central government in Moscow, the irrigated land increased by 4.9 million ha in 70 years of Soviet rule making the total cropland area to be 7.5 million ha. From 1950 onwards new projects were launched for developing highly integrated water distribution and irrigation networks. The agricultural production is more or less completely dependent on irrigation. The importance of agriculture can be understood from the fact that 40 % of population in CARs is directly employed in the agriculture sector and for a huge number it serves as major secondary income source (O'Hara 2000). Presently 93 % of total water resources are consumed for agricultural purposes but unfortunately this sector contributes least to the GDP mainly because of mismanagement (Porkka et al. 2012).

With the fall of the Russian Federation, there is no alternative energy source for upstream countries. Winter water releases, floods in low lying areas and water shortages are the outcomes of hydropower generation by Kyrgyzstan and Tajikistan. More than 90% of total electricity demand in these two countries is met through hydropower and they also export some (UNECE 2011). This causes increasing tensions between neighbor countries coupled with poor management, deterioration of infrastructure, lack of information system and distrust towards each other (Porkka et al. 2012; O'Hara 2000).

---

[1] http://www.unece.org/oes/nutshell/ecemap.html

Amu Darya is the largest river in Central Asia which originates from Tajikistan, Afghanistan and has a total length of 2540 km. The total catchment area of Amu Darya is 692, 300 km^2 with an average annual discharge of 78.5 km^3. The second largest river in Central Asia, Syr Darya, originates from Kyrgyzstan and is fed by Naryn and Kara Darya (Naryn Darya receives water from more than 700 glaciers in the Tien Shan mountain range). The total length of the river is 2200 km, with an average annual discharge of 37.2 km^3 (WARMAP 1996)**.** Amu and Syr Darya together account for almost 90 % of the total usable water resources in the Aral Sea Basin. The 10 % of the remaining water resources are generated from hundreds of small rivers and streams in the region.

The water use in Central Asia was small and most of the abstraction was made from small rivers and streams in the region until the first half of last century (O'Hara 2000). Diversion from large rivers was difficult and only 17 % of Amu Darya discharge was being used 50 years ago (Lewis 1962). With the rise in population and enormous increase in water demand for irrigation, hydro power, industrial use and ecosystem requirements, the harnessing of water resources and construction of large dams on big rivers is inevitable. But the importance of small rivers can still not be underestimated. The hundreds of small trans-boundary rivers, glacial lakes and ground waters are not only important in terms of water resources and sustainability of the communities living in their vicinity but they also pose a regular threat through calamities caused by floods or droughts to the same people. From unofficial sources around 2000 people died in Uzbekistan enclave of Shakimardan when a small dam broke in Kyrgyzstan after overfilling from a combination of high rainfall and high temperatures (O'Hara 2000). More recently on March 10, 2010, a small dam failed due to high rain and snow melt leaving 45 people dead, 300 injured and ruining hundreds of homes in a small village in Kazakhstan[2]. There are lots of similar cases of disasters caused by small dams and rivers.

There has been a large amount of research and practical work done on Amu and Syr Darya. Keeping in view the need of research on small transboundary rivers, this study focuses on Talas River, having a total length of 661 km and a catchment area of 44, 115 km^2. It is one example of the numerous small rivers and streams that generate 10 % of the water resources of the Aral Sea Basin. It originates from Kyrgyzstan and flows to Kazakhstan. Despite of its small size, the river is important to both of the countries and is a source of dispute among them also. The snowmelt and river runoff is simulated from 2000 to 2012 using TOPKAPI-ETH model. Most

---

[2] https://www.youtube.com/watch?v=Q00p_xKH4NQ

of the input data was obtained from remote sensing products. The simulated discharge and snow cover was compared with observed runoff from eight gauging stations and snow cover data supplied by MODIS. The accuracy assessment shows good correlation for the mountainous stations and fair correlation for floodplain gauging stations. In addition, the annual runoff prediction method is also proposed in the study that can be of great help in managing water resources of the river and preventing disasters caused by the floods or by below average discharge. The present study serves as a prototype of the bigger and complex problem faced by the Central Asian Republics regarding Transboundary Rivers.

1.1. Snowmelt Modeling

Snow cover has an important impact on earth’s energy balance and environment on a regional scale as 50 % of the Northern Hemisphere is covered by it in the winter (Dietz et al. 2013). The stream flow generated from snow melt is not only important for mountainous regions but it also provides water to the lowland areas. Mountains share 50 to 90 % (in extreme cases >95 %) of total rivers discharge in arid and semi-arid regions which make them one of the most important water towers of the world (Konz et al. 2010). Similarly the Hindu Kush-Karakoram-Himalaya (HKH) region is also called the third pole of the world due to the large amount of snow packs stored in their mountains and they provide water for drinking and agricultural purposes to some of the most populated countries in the world (Pellicciotti et al. 2012). Snow melt is a major source of fresh water for Aral Sea and Lake Balkhash catchments also. This makes the study of snow melt phenomena important. Variations in snow cover and spontaneous snow melt can result in natural calamities like droughts, floods, or landslides (Dietz et al. 2013).

Snowmelt models can be divided into two board categories; temperature index models (also called conceptual models by some authors (O'Hara 2000)) and physical energy balance models. The melt rate is calculated with an empirical formula with temperature as only input variable in the former model type. The latter may be defined as a model in which the melt rate is calculated from sum of energy fluxes taking place at the glacier surface. The individual fluxes are calculated from physically based measurements using direct computation of meteorological variables. Temperature index models have been widely used but they have the disadvantage that the melt rates can be calculated for the whole catchment in a lumped or semi lumped manner only (Pellicciotti et al. 2005). The physical energy balance models on the other hand have rigorous data requirements which are usually not met in remote catchments (like our study area) in developing countries.

Snowmelt is the major source of Talas river discharge. In this study, TOPKAPI-ETH model has been used which employs an enhanced temperature index method for estimating melt rates. It is an intermediate approach between the two categories described above and combines benefits of parsimonious data requirement and physical representation of important surface energy fluxes.

1.2. Study Area

Talas basin having a total area[3] of 44, 115 km^2, is located on the northern part of Tian-Shan Mountains and on the eastern corner of Turan lowland (Figure 1). The mountainous part of the basin lies in the Talas province of Kyrgyzstan where most of the river runoff is generated while the lowland area is in Jambyl province of Kazakhstan. There are 20 small rivers in Talas basin (UNECE 2007). The Karakol and Uch Kochoy rivers originating from Kyrgyz ridge and Talas Alatau meet at the tail end of Talas valley to form the Talas River proper. In the beginning, the river flows in the western direction and after entering Kazakhstan it flows in the north-western direction. The river runs through the cities of Talas, Kyrgyzstan and Taraz, Kazakhstan; and ends in the Moinkum sands before reaching Lake Aydyn forming small ponds and marshlands (UNECE 2011).

Talas River is 661 km long out of which 453 km (69 %) lie in Kazakhstan and 208 km (31 %) in Kyrgyzstan. There were 21 gauging stations on the river in Kyrgyzstan out of which only 13 are operational now (UNECE 2007). The runoff of Talas River is 1.616 km^3/year as stated in UNECE, Second Assessment of Transboundary Rivers, Lakes and Groundwaters (according to flows in 1983). The available water is equally divided between the two countries (CTWC 2006). There is only one reservoir on Talas River which is called Kirov reservoir. The designed storage capacity of Kirov is 0.55 km^3 (UNECE 2011). Analysis of last 13 years of data shows that the river has an average annual inflow of 0.87 km^3 at Kirov Reservoir. In Kazakhstan there is Tersashchibulak reservoir with a storage capacity of 158 million m^3 on the Ters River which is a tributary that runs into Talas (UNECE 2007).

Water is used for grazing and animal husbandry in the mountainous parts and it is abstracted for irrigation and animal husbandry in the foothills and lowlands of the basin. The irrigated

---

[3] The area of Talas Basin reported by Kyrgyz and Kazakh authorities is 52, 700 km^2 (UNECE 2011). The difference in area calculated by us occurred because the flat part of the catchment is difficult to delineate in ArcGIS. But this will not affect the results of present study whatsoever.

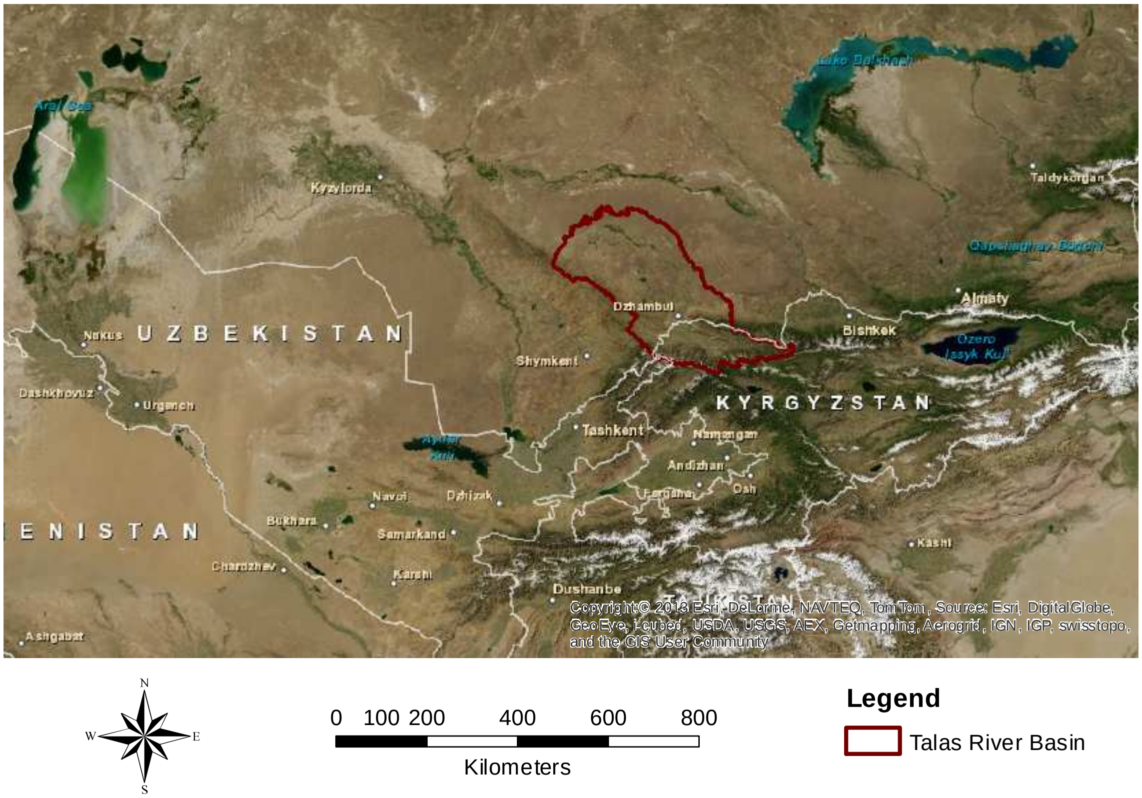

Figure 1: Geographical location of study area. Talas basin has borders with Chui and Jalalabad provinces of Kyrgyzstan on east and south side. It is connected to Uzbekistan by a small finger in the south-west direction.

land in Kyrgyzstan and Kazakhstan is approximately 137,600 ha and 105,000 ha (UNECE 2007). 95% of water resources are used for irrigation in the basin (CTWC 2008).

Application of pesticides and fertilizers on cropland is affecting water quality in both countries. The main sources of pollution in Kyrgyzstan are untreated industrial and residential waste water, mining waste in the mountains, animal breeding discharge and dumping of waste in open places close to the residential area. Ammonium-nitrogen and copper are the major pollutants and the concentration of iron is observed to be higher in water close to Talas city. An additional polluting factor in Kazakhstan is untreated waste water from sugar and alcohol factories (UNECE 2007). One important development in the recent years is gold and copper extraction from the mines in Kyrgyz ridge of Talas catchment[4]. This will bring economic prosperity as well as it will be a source of water pollution if necessary treatment methods are not adopted.

---

[4] http://www.tcg.kg/index.php?option=com_content&view=article&id=182&Itemid=184&lang=en

Contrary to most of the other transboundary waters, the cooperation on water resources management of Talas River is a success story. The delegations from the two countries agreed to resolve the problems through mutual understanding. The Chu-Talas Water Commission (CTWC[5]) was inaugurated on 26 July, 2006 in Bishkek to institutionalize the resources management and water management facilities in Chu-Talas basins. Kazakhstan agreed to pay part of the cost that it incurs in building new infrastructure and maintenance of the old (CTWC 2008). This is a good beginning to counter issues regarding sharing of water and has set example for other countries as well. The mutual distrust and lack of cooperation between experts' groups of the two countries are due to the following reasons (Rodina et al. 2008).

Figure 2: Pictorial view of 84 m high wall and discharge point of Talas Dam. The dam was constructed in 1975 (Rasskazchikov 2010). Image source (CTWC 2008)

- Timely assessment of water resources is not possible due to decaying infrastructure.
- The volume of water available from snow cover in Kyrgyzstan cannot be determined because of limited funds.
- The Kyrgyz officials cannot provide correct forecasts of precipitation in the vegetation season.
- Absence of accurate figures regarding water required for irrigation of cropland.

---

[5] http://www.youtube.com/watch?v=lVDxGCFR90s

All of this information is important for Kazakhstan to estimate the amount of water available for irrigation in summer and to take precautionary steps if there is a flood warning.

1.3. Aims and Objectives

The aim of the project is to investigate the relationship between snow melt and runoff in Talas River Basin. The runoff of Talas River is determined by snow melt in the mountains and precipitation. Snow cover and rainfall can be assessed by remote sensing. Together with a snow melt model and real time temperature data, the aim is to predict flows in the near future. The forecast will help in managing water storage and release from Kirov Reservoir.

1.4. Research Questions

1. Determine correlation between snow melt and runoff in Talas River.
2. Can remotely-sensed precipitation help in modeling runoff of the river?
3. How far can MODIS Snow Cover maps help in determining snow fall and snow melt timing in the study area?
4. Can one quantify the correlation between snow cover area in spring and annual water flow in the river?
5. What other methods can be used to predict summer runoff of the river three months in advance?
6. Can this knowledge be used in solving the conflict between the two countries?

1.5. Structure of thesis

The thesis is structured as follows. Chapter 2 introduces different datasets used in the study and their preparation steps briefly. A quick step by step working mechanism of TOPKAPI model and methods for assessing accuracy are also presented. Detailed analysis of the observed runoff, gauge precipitation, satellite precipitation estimates and bias correction methods are in the subjects of chapter 3.

Chapter 4 focuses on TOPKAPI modeled runoff and its comparison with the observed runoff. The accuracy of simulated snow cover, overestimation of modeled runoff due to bias in TRMM precipitation data, irrigation demand in the catchment, different ecosystem components of the model and distribution of water among them are also described in this section.

The annual runoff forecast method for Talas catchment along with its accuracy is proposed in chapter 5. And finally the thesis is concluded in chapter 6 by discussing the results presented in previous chapters and proposing some steps that can be helpful for future researchers working on Talas River or similar case studies.

Chapter 2

2. Data Preparation

2.1. Digital Elevation Model

The Digital Elevation Map (DEM) of the study area was extracted from ASTER (Advanced Spaceborne Thermal Emission and Reflection Radiometer[6]) Global Digital Elevation Map version 2 (GDEM). It is perhaps the highest resolution publicly available global DEM having spatial resolution of 30 m × 30 m (1 arc-second). The data is referenced to WGS-1984 Geographic Coordinate System and is available in GeoTIFF format that can easily be opened in ArcGIS.

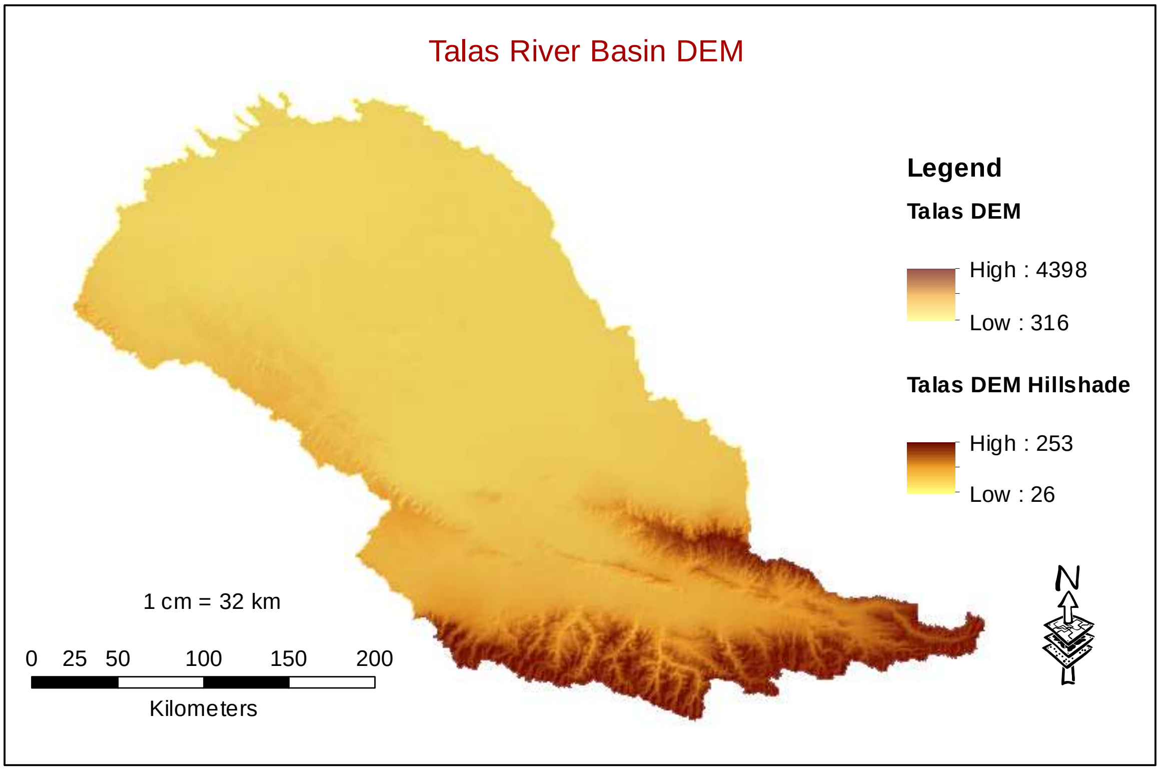

Figure 3: Digital Elevation Map of the study area showing height distribution. The map is made by overlaying DEM on to hill shade of the study area to make the mountains prominent.

---

[6] http://asterweb.jpl.nasa.gov/gdem.asp

Table 1: Percentage of area in different elevation classes in Talas River Basin. The first column shows contour interval of 500 m and height above sea level.

Elevation Range	Area (km^2)	Percentage
316 - 500	21313.25	48.31
500 - 1000	9749.5	22.10
1000 - 1500	4535.75	10.28
1500- 2000	2279	5.17
2000 - 2500	2033.5	4.61
2500 - 3000	1715.25	3.89
3000 - 3500	1678.5	3.80
3500 - 4398	813	1.84
Total	**44117.75**	**100**

As a first step, fifteen tiles were mosaicked to contain the study site with 1 degree of buffer area on all sides. The catchment area and stream network of Talas River was generated through standard GIS procedures. This includes use of tools like sink, fill, flow direction, flow accumulation, stream order, basin, stream to future etc. under ArcGIS Hydrology toolbox. Because the snow cover maps generated by the model were to be compared with MODIS Snow Cover maps available at resolution of 500 m × 500 m, the model was run at the grid size of 500 m and the DEM was also resampled from 30 m to 500 m resolution.

70.4 % of the basin lies between an elevation range of 316 m and 1000 m above sea level. This part is the comparatively flat and dry portion of the basin and 97 % of this is within Kazakhstan. A contour map of the study area with an interval of 500 meters was made and Table 1 shows the percentage of area present in each contour interval.

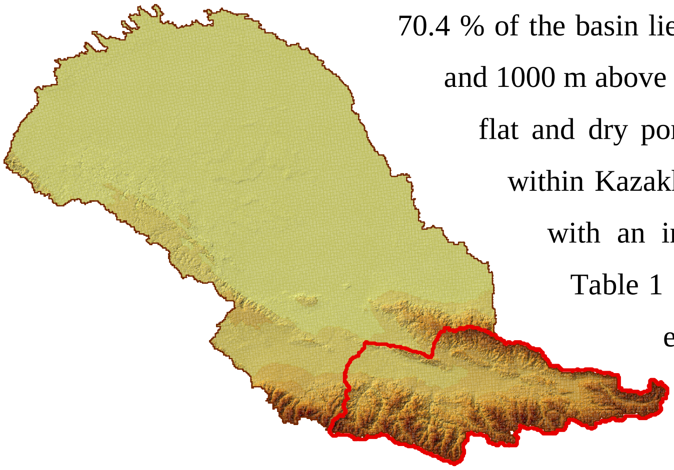

Figure 4: Outline of Talas basin upstream of Kirov Reservoir. The present study focuses on this area only.

2.1.1. Talas Upper Valley

As the major portion of river runoff is generated in the mountains by snow melt in the summer, we decided to focus on this region only and study the basin upstream of Kirov reservoir. Only this part of the basin is relevant for the operation of Kirov Reservoir. The area lies on North – West corner of Kyrgyzstan between coordinates 42 to 43 North and 71 to 74 East. It is only 19 % of the total catchment covering an area of 8957 km^2 which also includes 1142 km^2 of irrigated land.

The DEM of Talas basin upstream of Kirov reservoir is shown in Figure 5. Please note that this region will be referred to as study area and Talas River Basin in the report now unless stated otherwise. A Landsat image of the basin can be seen in Figure 80 Appendix A. The percentage of area present in each contour interval of 500 meters is shown in Table 2.

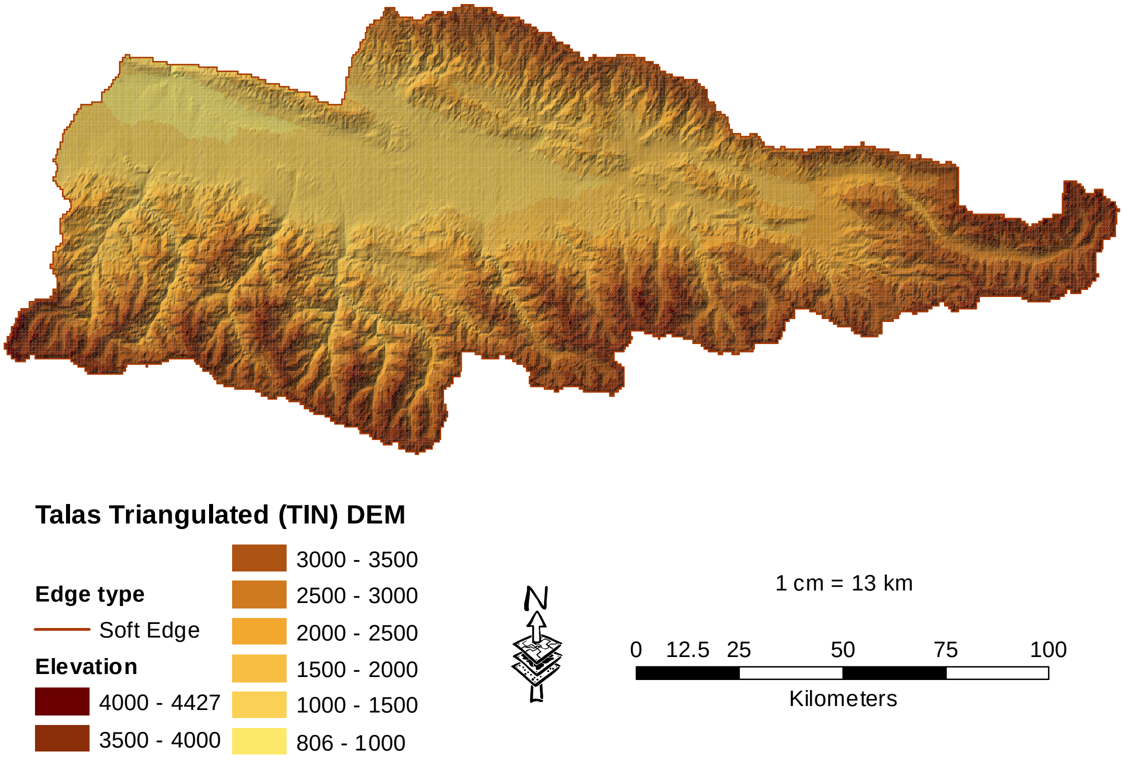

Figure 5: Triangulated Digital Elevation Map of Talas river basin upstream of Kirov Reservoir. Talas valley is located in north of Talas-Alatau mountain range which forms the southern and eastern border of Talas Province. On the northern side of the valley is Kyrgyz Alatau mountain range which forms natural border between Kyrgyzstan and Kazakhstan. Kyrgyz Alatau and Talas Alatau are part of the famous Tien Shan mountain range.

Table 2: Percentage of area in different elevation classes in Talas upper valley. The first column shows contour interval of 500 m and height above sea level.

Elevation Range	Area (km^2)	Percentage
806 - 1000	251	2.80
1000 - 1500	1489	16.62
1500 - 2000	1592.25	17.78
2000 - 2500	1605.5	17.92
2500 - 3000	1480.25	16.53
3000 - 3500	1640	18.31
3500 - 4000	853.5	9.53
4000 - 4497	45.5	0.51
Total	**8957**	**100**

The contour map can be seen in Figure 82 in Appendix A.

2.2. TOPKAPI Model

The project was carried out using the hydrological model **“Topographic Kinematic APproximation and Integration model”** (**TOPKAPI**). It is a fully distributed model representing major hydrological processes physically based and is mainly developed for flood prediction and routing. The model is based on solving the kinematic wave equation for water at three levels. (1) Horizontal drainage in the soil, (2) Overland flow on saturated soil and (3) Channel flow.

TOPKAPI is used as research tool in ETH Zurich and is not available commercially. It has been successfully applied in Italy, China and Switzerland. The model can efficiently simulate snow cover, snow melt, glacier melt; under natural flow conditions and steep areas and is suitable for water management operations analysis. The model was run at hourly time step and at a grid size of 500 m × 500 m. All of the input data is required hourly except cloud transmissivity which should be provided at a daily time step. The model requires six fields of input data in order to run.

1. Digital Elevation Map (DEM) is required to generate river and streams network. The geometric properties of channels like length and width together with roughness coefficients are also needed to feed the model.
2. TOPKAPI requires the land cover map of the study area which is a key to calculate potential evapotranspiration depending on cropping factor and vegetation.
3. Soil depth and hydraulic conductivity both in horizontal and vertical directions are the most important data required for the model. The hydraulic conductivity can be found by FAO soil type maps of the world and tables for hydraulic conductivity of each type. The soil depth has proven to be the trickiest part of data required so far for this model.
4. Air temperature is required and it should be adjusted for high altitudes according to the lapse rate. This is important for simulating snow cover and snow melt.
5. Precipitation is one of the most important input data required by the model as it is the main source of water either in liquid or solid form and contributes to river flow.
6. Cloud transmissivity is also required which is used to calculate global irradiance.

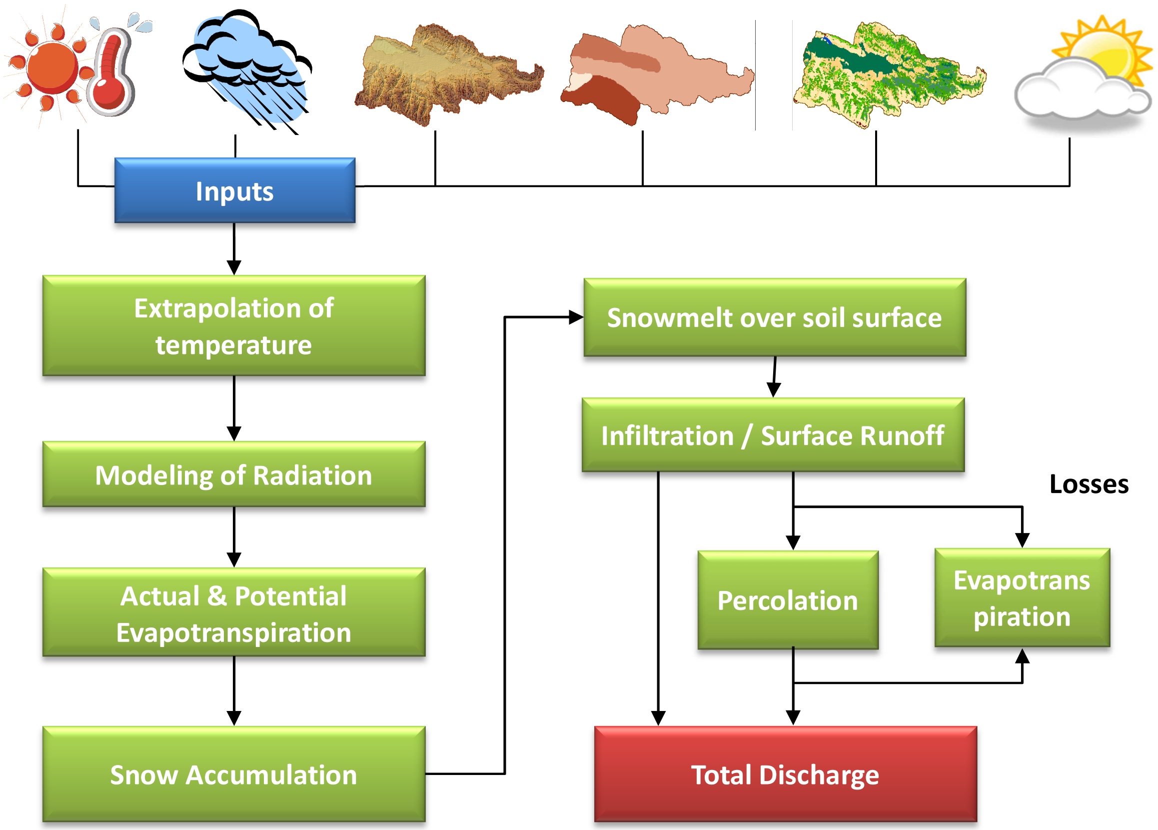

Figure 6: Simplified flow chart of TOPKAPI-ETH model structure.

2.3. Talas Meteorological Station

There is only one meteorological station in the study area which is located in the center of Talas valley. The data go back to 1975 and are available on NCDC NOAA website[7]. There are 13 different climatic factors available in the data but only temperature and precipitation are used in this project. Snow height data is also available but there are only two or three readings from each month with unusual peaks in summer in some cases which makes the data unreliable and hence they are not used in the project.

2.3.1. Temperature

Temperature data is available at temporal resolution of three hours. Missing values for a particular day and time were filled by taking the average of temperature for the same day and time from all other years. It was then interpolated to hourly time step using the Piecewise Cubic Hermite Interpolating Polynomial (PCHIP) method in MatLab.

2.3.2. Precipitation Data

Precipitation is one of the most important inputs to the model. The observed precipitation data is available at daily time step from Talas meteorological station. This data is also available from 1975 and the missing values were processed in the same way as temperature. The mean yearly precipitation is 196 mm only and the area is classified as semi-arid region because of its lower precipitation compared to potential evapotranspiration.

Data from precipitation gauges can have shortcomings. Most importantly they do not have dense coverage in a watershed especially in developing and semi-arid countries. Gauge observations usually underestimate precipitation because of turbulence introduced by wind at the gauge orifice, blowing of snow / rainfall in windy climate, wetting losses on gauge walls, splashing and evaporation (Smith et al. 2006; Boushaki et al. 2009; Huffman et al. 1997). Gauge measurements can have a bias range of 4 – 5 % with the largest error possibility in snowfall. They can also have systematic and representative error. Representative error occurs because the amount of precipitation observed at a point may not effectively represent rainfall in its neighborhood due to a localized rainfall event (Boushaki et al. 2009).

---

[7] http://www.ncdc.noaa.gov/data-access/land-based-station-data/land-based-datasets/global-historical-climatology-network-ghcn

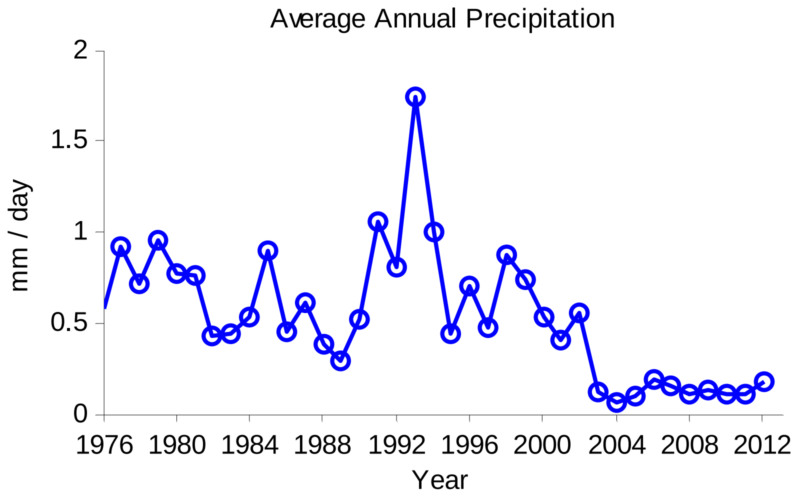

Figure 7: Average annual gauge observed precipitation from 1976 to 2012. The graph shows daily precipitation averaged for each year from (1976 to 2012). The gauge is not working since 2002.

Figure 7 shows mean daily precipitation in Talas Valley since 1976. The precipitation declines suddenly in 2002 and onwards because the precipitation gauge malfunctioned.

The aim of the project was to use remotely sensed precipitation products in order to have distributed rainfall data over the entire catchment. As gauge data is incomplete for the last ten years to be modeled, this favored the decision of using remotely sensed precipitation estimates which are described in the next section.

.

2.4. Remotely Sensed Precipitation Products

Satellite products provide a good alternative for un-gauged catchments. Since two decades, huge progress has been made in this domain and remotely sensed products have become an inevitable data source in many areas of science. Satellites offer better spatial coverage especially over mountainous areas as compared to radar and gauge measurements. Satellite Precipitation Estimates (SPEs) are derived either from infrared and visible radiations range of GEO satellites establishing a relationship between cloud characteristics and rainfall rate at the surface or from active / passive microwave data of low earth satellites measuring the precipitation rate by analyzing hydro-meteoric distribution of clouds (Boushaki et al. 2009). They have less spatial sampling and random errors as compared to gauge sampling.

On the other hand, satellites also have a major problem of bias because they measure processes in the atmosphere remotely. The problem can arise due to improper tuning of satellite instruments, diurnal sampling bias, problems in the software code, unexpected surface or atmospheric phenomena which the code cannot understand (Smith et al. 2006). Satellites also have bias because they measure thermal radiance of clouds instead of measuring precipitation directly from the surface. And in case of radar observations bias can occur due to unaccounted evaporation losses and beam blockage over mountainous regions (Boushaki et al. 2009). The newer instruments and algorithms have less bias in comparison to their predecessors. But still it is very important to develop bias correction methods to correctly quantify data available from initial satellite sensors (Smith et al. 2006). The satellite data used in this project was also bias corrected which is explained later.

We decided to use TRMM and CMORPH precipitation products in the project. The idea behind using two datasets was that although TRMM is an older product and much research studies have been made and published using TRMM data. It is known to have some errors. And as good quality of observed data was not available, it was important to check different datasets available to see which one has a precipitation closer to reality at the gauging station and produces realistic runoff. CMORPH is a relatively newer product and is also available in better resolution compared to TRMM.

2.4.1. TRMM Precipitation Data

TRMM is the abbreviation of Tropical Rainfall Measuring Mission which is a collaborative program between National Space Development Agency (NASDA) in Japan and National

Aeronautics and Space Administration (NASA) in United States. The primary mission of TRMM is to measure precipitation in tropics and tropical oceans (Bowman 2005). Latent heat released during precipitation accounts for three-fourth of heat energy received by the atmosphere and approximately two-third of earth's precipitation falls in the tropical region (± 35 degrees) which makes it one of the main drivers of global atmospheric circulation. 75 % of the tropical region is covered with oceans (Kummerow et al. 1998). Most of the oceanic rain gauges are located on islands which due to different topographic and surface heating features have different precipitation than the ocean around them. TRMM was launched to provide good spatial coverage over tropics especially tropical oceans to compensate for absence of gauge precipitation there. It has TRMM Microwave Imager (TMI) and Precipitation Radar (PR) instruments for measuring precipitation on board. TMI is a passive microwave radiometer which measures precipitation by differentiating warm raindrops emitting microwaves from the cold ocean background. Due to changing surface emissivity, TMI is less efficient over land. PR is the first space-based radar which provides three dimensional (especially vertical) profiles and near surface estimates of precipitation at high resolution (Bowman 2005).

2.4.1.1. Pre-processing of TRMM Data

TRMM data is available from 1998 at different temporal and spatial scales. The TRMM 3B42 daily product having spatial resolution of 0.25° × 0.25° is used in this project. TRMM data can be downloaded[8] in Hierarchical Data Format (HDF), NetCDF and ASCII formats. Since ASCII was not available for large downloads, data was obtained in NetCDF format. The images were downloaded for the whole world and the study area was extracted using a small iterative model in ArcGIS performing the following steps.

1. Import data in ArcGIS using "Make NetCDF Raster Layer" command.
2. Define geographical reference system of the file as WGS-1984.
3. Extract study area from raster image using "Extract by Mask" command.
4. Save the extracted image as text file (.txt) with unique date number.
5. Divide study area into a set of virtual stations for precipitation depending on the spatial resolution of TRMM and give them a unique ID. This resulted in 31 virtual stations.
6. Assign a unique virtual station ID to each of the smaller grid cells of 500 m × 500 m. Hence all smaller pixels residing in a particular TRMM virtual station area will have the

---

[8] http://disc.sci.gsfc.nasa.gov/giovanni, http://pmm.nasa.gov/node/158

same precipitation as that of the TRMM pixel. Make a map of this to be given as input to TOPKAPI. This is shown in the figure below for better understanding.

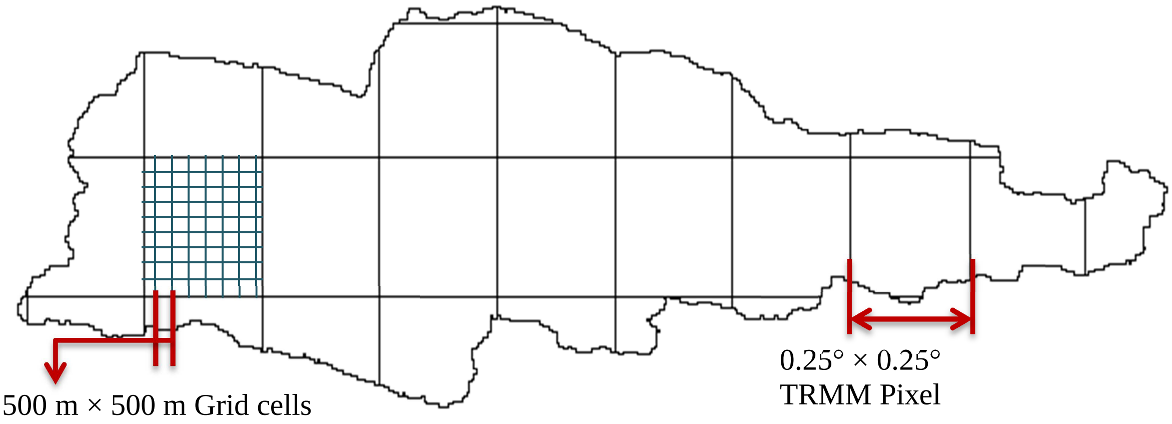

Figure 8: Study area divided according to TRMM spatial resolution where each pixel will act as a Virtual station.

The text files prepared in ArcGIS were later imported to MatLab for further processing. This included downscaling from daily to hourly time step by dividing by 24, making time series of data and saving in a single CSV file with a header to make it compatible with TOPKAPI input requirements.

2.4.2. CMORPH Precipitation Data

CMORPH[9] (CPC MORPHing technique) is a gridded and relatively new product compared to TRMM. It incorporates Passive MicroWave (PMW) data from low orbiting satellites and Geostationary Operational Environmental Satellites (GOES) infrared (IR) imagery data (Joyce et al. 2004). The algorithm uses precipitation estimates that have already been derived from microwave observations. In case of missing data for a location, spatial lag correlations are computed by using series of geostationary satellite IR images to produce propagation vector matrices. These matrices are then used to propagate precipitation estimates derived from microwave observations. This helps in producing precipitation estimates at relatively higher spatial and temporal resolution (Joyce et al. 2004).

---

[9] http://www.cpc.ncep.noaa.gov/products/janowiak/cmorph_description.html

CMORPH has three different data sets available depending on temporal and spatial resolution. The daily product with 0.25° × 0.25° latitude / longitude resolution was used and it was prepared in a similar way as TRMM i.e. full images were downloaded and the study area was extracted in ArcGIS.

2.5. Bias Correction

As explained in the last two sections, satellite sensors can have biases. This means that although the sensor is a good instrument, its instantaneous or average values are not exactly equal to the observed ones. The difference between the instrument's and the true value is called bias. When an instrument has this kind of error, it is possible to estimate the bias and improve the data by subtracting or adding the estimated bias from the observed readings. This procedure is called bias correction.

As indirect methods are used to derive satellite based rainfall measurements, they are prone to higher biases compared to radar based rainfall products. Scientists have been using different techniques for bias correction. e.g. merging radar and satellite based rainfall estimates and quantifying the bias to make data consistent (Tesfagiorgis et al. 2011). A simple covariance method is used here for applying bias correction to TRMM data. Covariance can be defined as correspondence between two random variables. Mathematically the covariance between two random variables is given by

$$\sigma\,(x,y) \;=\; \frac{\sum_{i=1}^{n}\;(x_i\;-\;\bar{x}) \times (y_i - \;\bar{y}\,)}{n-1} \tag{1}$$

Where $\bar{x}$ and $\bar{y}$ are averages of variables x and y. In MatLab “$lscov$” command is used to generate the least sum of squared errors between two variables in presence of known covariance by optimizing the bias factor $1/a$.

$$a = lscov\;(G_M, S_M) \tag{2}$$

where G_M is a gauging station observed or actual precipitation and S_M is satellite estimated value. The above equation gives the least squares solution to the linear system of equations $G_M \times a = S_M$. Then the corrected data is given by

$$Bias\ Factor = 1/a \tag{3}$$

$$Corrected\ Data = Raw\ Data\ \times Bias\ Factor \tag{4}$$

GPCC Full Data Reanalysis Version 6.0 data and rain gauge observed data was used for bias correction. GPCC was used because the observed precipitation data is not available for last ten years. Another benefit was to have variable and distributed correction factors. This was not possible with observed precipitation as the data is available from only one gauge which is not enough to correctly interpolate the precipitation to each grid cell considering sharp topographical changes in the catchment.

2.5.1. GPCC Bias Correction

Global Precipitation Climatology Center (GPCC) provides one of the world's finest and largest gridded area mean rain gauge precipitation dataset. They have four different products available with a fifth coming soon, each one suitable for different research requirements at a spatial resolution of 2.5, 1 and 0.5 degrees. It combines data from two broad classes depending on availability. The near-real-time data from SYNOP-DWD[10], CLIMAT[11] bulletins, monthly totals from SYNOP-CPC[12] obtained through Global Telecommunication System (GTS) and non-real-time data which forms the bigger portion obtained from National Meteorological and Hydrological Services (NMHS) supplied by WMO, data collected regionally and globally and monthly sums calculated from Global Historical Climatology Network (GHCN) daily data. This is pictorially shown in Figure 84 (Appendix A). GPCC only uses data from a gauging station that has at least 10 years of uninterrupted time-series. In total, approximately 65, 200 stations pass this barrier and hence have been used to produce different precipitation products. The data gathered from different sources is stored in eight different slots in a Relational Database Management System (RDBMS). This helps in cross comparison and pre-processing of data according to different source and initial errors present in each source by a specific set of

---

[10] SYNOP data received at Deutscher Wetterdienst, Germany. SYNOP is abbreviation of surface synoptic observations encoded in SYNOP (FM-12) data format. For more information visit http://weather.unisys.com/wxp/Appendices/Formats/SYNOP.html

[11] Name for monthly averages or sums compiled from SYNOP reports

[12] Monthly precipitation data compiled by Climate Prediction Center, Washington DC using SYNOP data

algorithms (Becker 2013). It is followed by area averaged precipitation estimates on to grid cells from gauge readings performed in three steps which are (i) the data is interpolated from point observations to 0.25 degree latitude / longitude grid cells using a robust and empirical SPHEREMAP interpolation method, (ii) estimation of area averaged precipitation for 0.25 or 0.5 degree grid cells, (iii) and calculation of area averaged precipitation for coarser resolution of 0.5°, 1° or 2.5° grid mesh (Becker 2013; Huffman et al. 1997).

GPCC Full Data Reanalysis Version 6.0 (GPCC FD) provides highest accuracy and is used in this project. The temporal coverage ranges from 1901 to 2010 and the data is available as total monthly precipitation having spatial resolution of 0.5° × 0.5°. GPCC data was prepared for the study area in a similar manner as explained for TRMM and CMORPH. In order to compare the two products the monthly sum of TRMM data was taken. Since GPCC has coarser spatial resolution, more than one TRMM pixel can be accommodated in a single GPCC pixel. Hence all TRMM pixels present in the area of one GPCC pixel were bias corrected after comparing with that single pixel. This is shown in the figure below.

2.5.2. Observed Precipitation Bias Correction

Observed precipitation bias correction was carried out using data from four overlapping years before the gauge stopped working i.e. 1998 to 2001. The covariance matrix between observed precipitation and TRMM precipitation for the pixel where Talas meteorological station is located was produced which gave a bias factor of 0.6690. This single bias factor was used for correction of all TRMM data. This is a draw back in gauge bias correction due to availability of data from only one gauge which is not enough to correctly interpolate the precipitation to each grid cell considering sharp topographical changes in the catchment. The idea behind using GPCC was to have variable and distributed correction factors for each grid cell. Another problem with the observed precipitation data is that it is not available for the last ten years. But surprisingly the gauge bias correction gave better results compared to GPCC bias correction which is discussed in chapter 3.

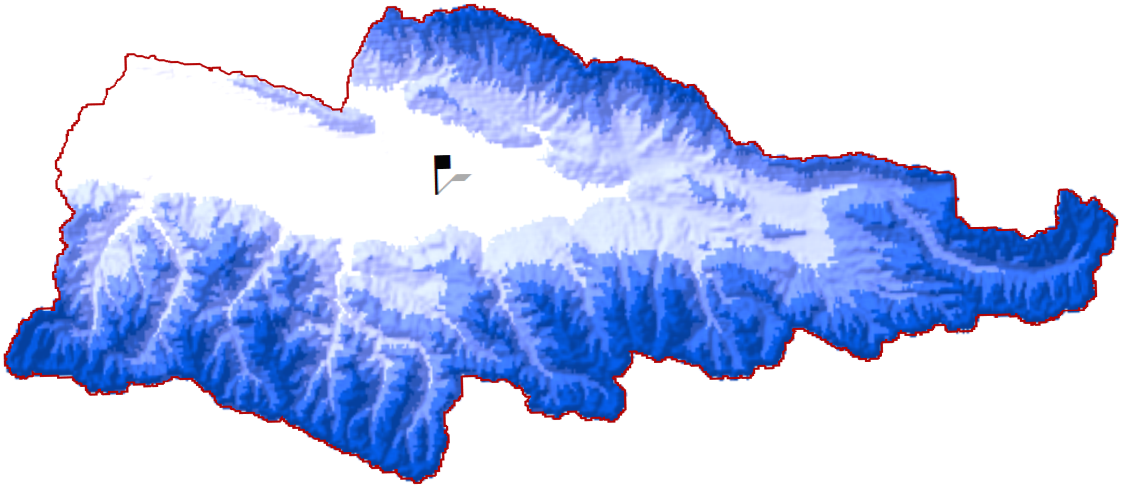

Figure 9: Location of Talas meteorological station in the valley.

2.6. FAO Harmonized World Soil Database

The Harmonized World Soil Database (HWSD)[13] is produced by joint efforts of the Food and Agriculture Organization (FAO) and the Land Use Change and Agriculture Program (LUC) of the International Institute for Applied System Analysis (IIASA), Austria. They combined data from 5 different sources namely (i) FAO soil maps of the world (ii) regional studies made by SOTER (Global and National Soils and Terrain Digital Databases) (iii) data from the European Soil Bureau Network (ESBN) (iv) the 1:1 million scale soil map of China obtained through Institute of Soil Science, Chinese Academy of Sciences and (v) soil parameter estimates based on the World Inventory of Soil Emission Potential (WISE) database. The data is available at spatial resolution of 1 km (30 arc seconds) provided in "Band interleaved by line" (BIL) format. It has 1600 different soil mapping units with information on soil parameters like organic carbon, pH, water storage capacity, soil depth, total exchangeable nutrients, lime and gypsum contents, sodium exchange percentage and textural class (Nachtergaele et al. 2009).

The data is provided in WGS-1984 Geographic Coordinate System projection which is consistent with the projection used in our case study. However the study area was extracted using ArcGIS in a quite similar manner as for other datasets explained earlier (Figure 10). The percentage of different soil types and area covered by them in the catchment is presented in Table 3.

---

[13] http://www.fao.org/nr/land/soils/harmonized-world-soil-database/en/

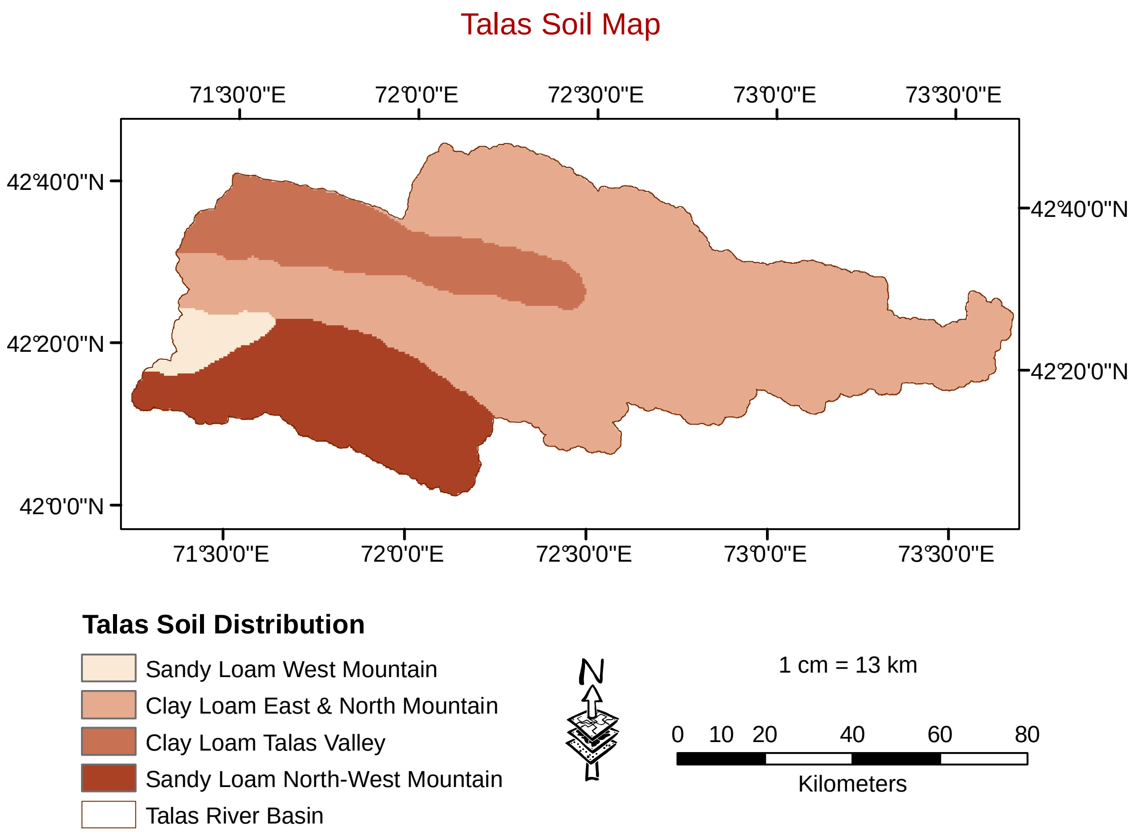

Figure 10: Soil map of Talas basin made from FAO Harmonized World Soil Database.

Table 3: Percentage of different soil types in Talas River Basin.

Soil Type	Area (km^2)	Percentage
Sandy Loam West Mountain	244.25	2.727
Clay Loam Talas Valley	1278.15	14.270
Sandy Loam South-West Mountain	1651.25	18.435
Clay Loam East & North Mountain	5782.75	64.561
Total	**8957**	**100**

2.7. Cloud Transmissivity

Cloud Transmissivity (CT) is used to estimate global irradiance. The CM-SAF[14] remotely sensed mean daily Cloud Fractional Cover (CFC) data was used to calculate CT for the study area.

Climate Monitoring (CM) is a dedicated center for research on global climate change within the Satellite Application Facility (SAF) of the European Organization for the Exploitation of Meteorological Satellites[15] (EUMETSAT). In short it is called CM-SAF. The center is hosted by the German Meteorological Service (Deutscher Wetterdienst, DWD) in Offenbach and is run in collaboration with meteorological institutes of Belgium, Finland, Netherlands, Sweden, Switzerland and United Kingdom (Karlsson and Hollmann 2012).

CM-SAF uses data from NOAA satellites observations made by Advanced Very High Resolution Radiometer (AVHRR) on board. The time series ranges between 1982 - 2009 (first NOAA-7 satellite and last NOAA-18 satellite). CFC data is available at spatial resolution of 0.25 degree latitude / longitude grids in NetCDF format (Karlsson and Hollmann 2012).

2.7.1. Pre-processing of Cloud Fractional Cover Data

The pre-processing of cloud fractional cover was also carried out in MatLab and ArcGIS. The data was available till end of 2009. In order to fill the gap for the last three years i.e. 2010 – 2012, data from 2007 – 2009 was repeated. CT was then calculated from CFC by using the relation below (Kasten and Czeplak 1980).

$$CT = 1 - (a \times CFC^{b}) \qquad (5)$$

Where $a = 0.75$ and $b = 3.4$ are parameters. Cloud transmissivity values can range between > 0 and ≤ 1 with 0 as a sky completely covered with clouds and 1 as 100% clear sky. The lowest possible mean daily CT was limited to 0.20 because values lower than this will mean a completely dark day.

---

[14] http://www.cmsaf.eu/bvbw/appmanager/bvbw/cmsafInternet

[15] http://www.eumetsat.int/website/home/index.html

CT was also used like TRMM within the concept of virtual stations. All of the smaller 500 m × 500 m pixels residing in a big pixel of CT were given the same value. For this purpose a CT pixel ID map was created in ArcGIS.

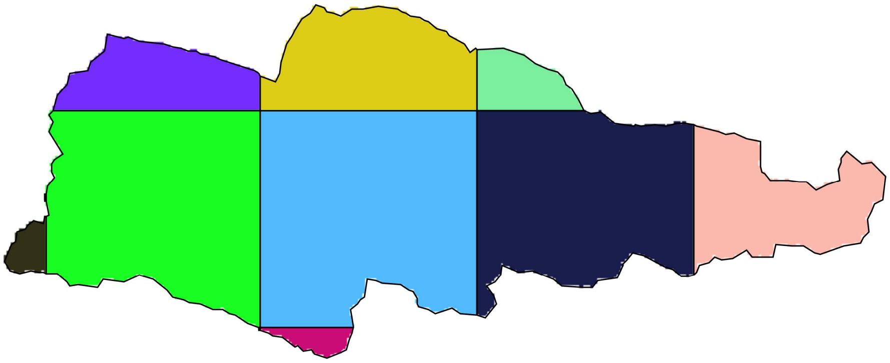

Figure 11: Study area divided according to spatial resolution of Cloud Fractional Cover grid size.

2.8. Land Cover Map

The land cover map of the region was made from GLOBE Cover data which is also a remotely sensed product. Globe Cover[16] is one of the projects run by the European Space Agency (ESA) in order to provide a global land cover map, bimonthly and annual surface reflectance mosaics at fine resolution. The data is derived from Medium Resolution Imaging Spectrometer Instrument (MERIS) on board the ENVISAT satellite launched in 2002. MERIS measures reflected solar radiations from earth surface in 15 spectral bands between 412.5 nm to 900 nm. Raw data is pre-processed to apply geometric correction, atmospheric correction, cloud screening and Land / Water reclassification. The measured reflectance is associated with signatures of different land covers in a classification module comprised of supervised and un-supervised classification together with other refinements. The final map is based on 22 land cover classes defined by United Nations Land Cover Classification System (LCCS) that are widely used and accepted in the world. The overall class weighted accuracy of the map is 67.5 % when using 2190 globally distributed points for validation (Bontemps et al. 2011).

---

[16] http://due.esrin.esa.int/globcover/

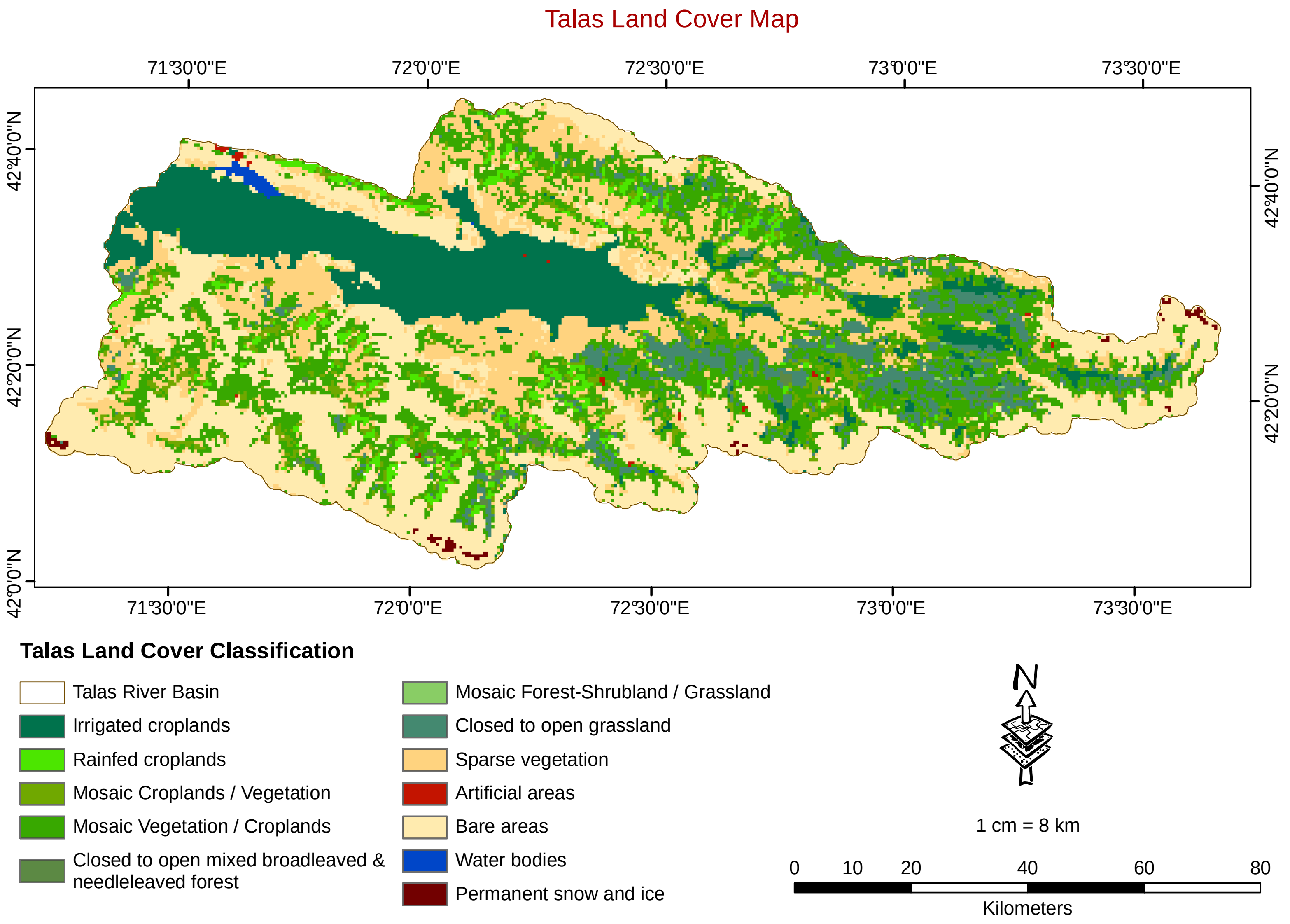

Figure 12: Land cover map of Talas basin showing distribution of 12 land cover classes in the study area.

The product is provided at spatial resolution of 300 meters and in Plate-Carrée projection with geographic latitude / longitude grids referenced to WGS-1984 ellipsoid. A colored version of map is available in TIFF format that was imported to ArcGIS and projected to the Geographic Coordinate System. The map was then resampled to 500 meter resolution and the study area was extracted.

Table 4: Different land cover classes and their percentages of total area in Talas River Basin. The data is derived from land cover map of the study area made from GLOBE Cover product.

Land Cover Class	Area (km2)	Percentage
Irrigated croplands	1364	15.23086
Rain fed croplands	248.75	2.777623
Mosaic croplands / vegetation	469.5	5.242588
Mosaic vegetation / croplands	2031.25	22.68159
Closed to open mixed forest [17]	35.5	0.396404
Mosaic forest-shrub land / grassland	5.25	0.058623
Closed to open grassland	554.75	6.194517
Sparse vegetation	1824.25	20.37016
Artificial areas	12.5	0.139579
Bare areas	2359	26.34135
Water Bodies	23.25	0.259617
Permanent snow & ice	27.5	0.307074
Total	**8955.5**	**100**

2.8.1. Water Abstraction Map

Talas basin has a valley in its center which is mainly an agriculture area. Farming and animal husbandry are the major sources of income of communities living there. A large volume of river water is being used in the valley and this fact has to be incorporated in the model. The globe cover land use map mentioned in the last heading was used to produce the agricultural area map. It was done in ArcGIS using topology and parcel fabrics toolboxes. These tools offer

---

[17] Closed to open mixed broadleaved & needle leaved forest

efficient creation, editing and management of contiguous blocks e.g. split a big area into small blocks according to desired size or proportion, give each new block a unique ID and associate desirable properties with it, prevent overlapping of area, boundaries and rule out gaps within blocks. A brief step by step procedure of making a water abstraction map includes (i) Two of the land cover classes namely irrigated croplands and mosaic cropland / vegetation (>70 % agriculture area) were merged to make one big polygon. This gave a total cropland area of 114,200 ha (ii) The area was divided in 71 blocks called irrigation districts. (iii) Each district was assigned a unique outlet point from the nearest stream in order to supply water to that area. (iv) Water abstraction schedule was made starting from March to October. (v) Hourly irrigation rate and minimum soil moisture content above which irrigation will start was also set for each district.

Figure 13: Talas Irrigation districts map. The 71 districts are shown here in unique colors.

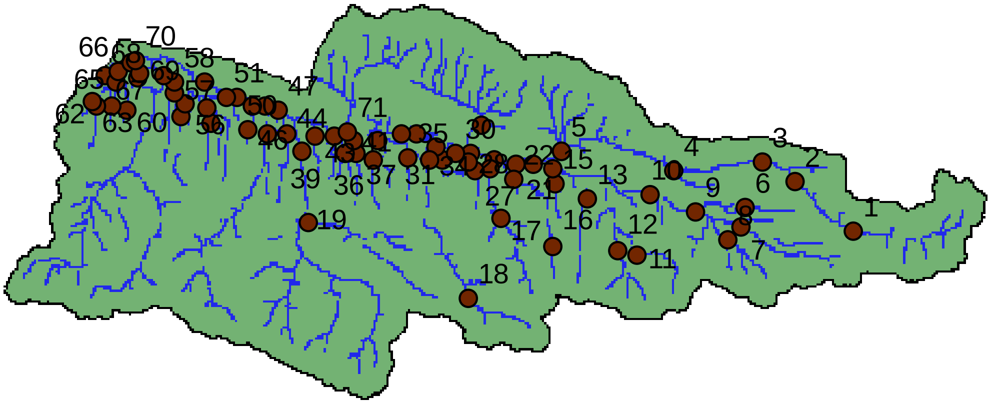

Figure 14: Outlet points for irrigation of cropland in the catchment. The 71 irrigation districts were supplied water from unique outlet points in the river or stream.

2.9. Accuracy Assessment

The model results are validated against observed runoff in the river at eight gauging stations and the MODIS snow cover product. These two datasets are explained in the next two sections.

2.9.1. Runoff Gauging Stations

The runoff data was obtained from Kyrgyz Water Resources Department for eight gauging stations at different locations in the catchment. It is in the form of decadal means. i.e. ten days averages and hence three readings from each month. The data was obtained from January, 2000 to December, 2012 with exception of Uch Kochoy gauging station. The station was closed from October, 2005 until the end of 2006 because the flow was directed to another stream due to road construction. The missing data for year 2005 was filled by taking average runoff of the same months in other years. The station had a defect in September 2009. The data is not available after that time and it was left untreated. Figure 15 shows the locations of gauging stations in the catchment. A generalized map of the river in the whole Talas basin is presented in Figure 85, Appendix A.

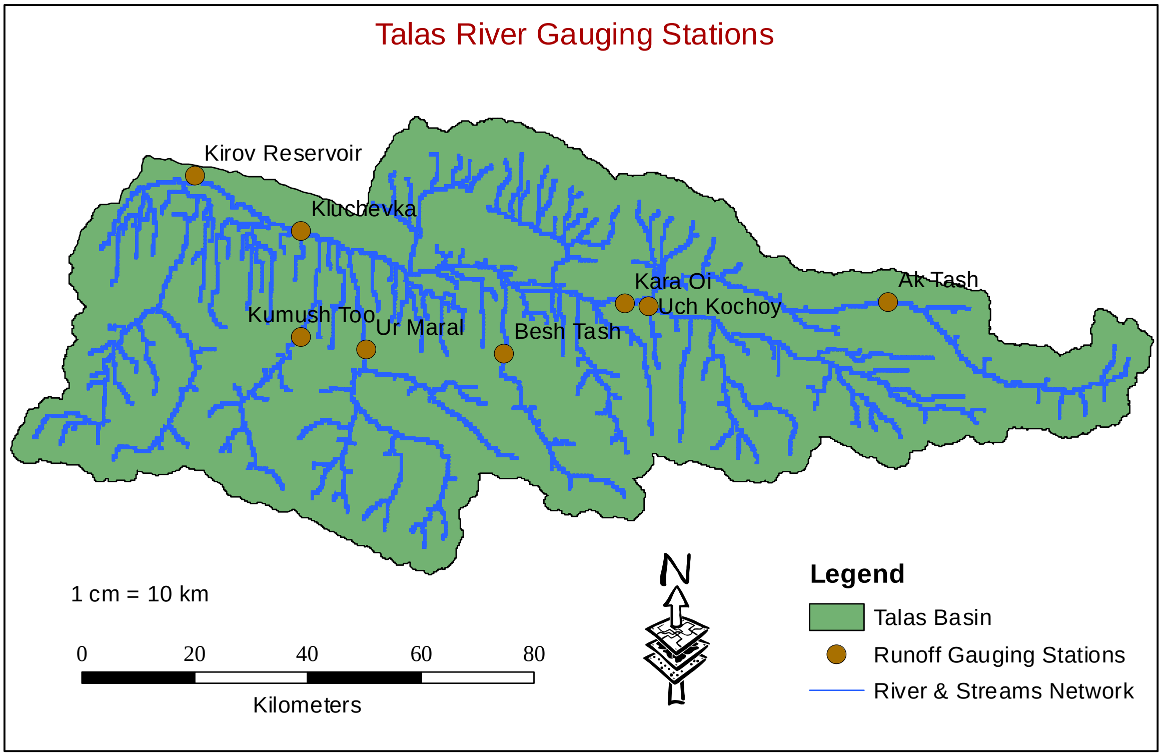

Figure 15: Location of mountainous and flood plain gauging stations. Ak Tash, Besh Tash, Kumush Too and Ur Maral are mountainous stations while Uch Kochoy, Kara Oi, Kluchevka and Kirov are in the flood plain.

The stations are divided in two broad classes; mountainous and floodplain gauging stations. The former stations are located on the mountains with little or no agriculture area in the sub-catchment while the latter stations are present in the valley or flat part of the basin with some agriculture area in the sub-catchment.

2.9.1.1. Sub-catchments

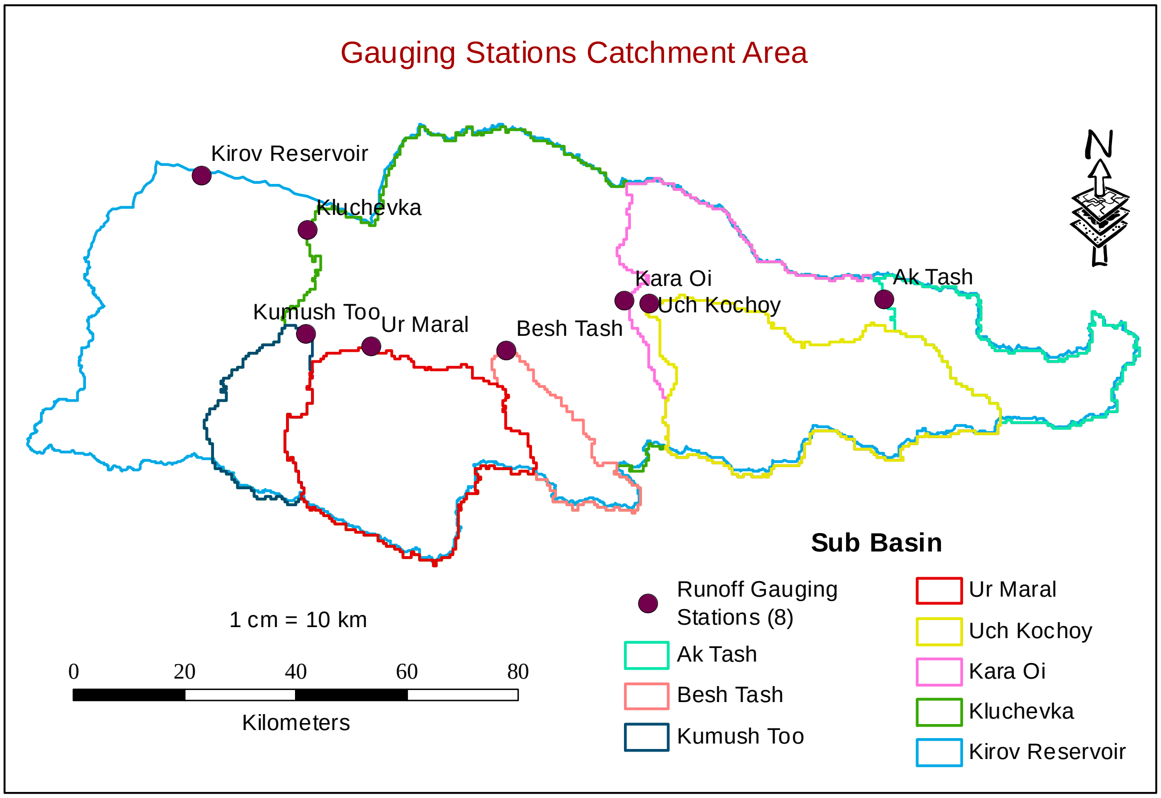

Figure 16: Location of runoff gauging stations and sub catchment area of each station.

Table 5: Sub-catchment areas of gauging stations.

Gauging Station Name	Area (km^2)
Besh Tash	307.188
Kumush Too	391.678
Ak Tash	557.630
Ur Maral	1101.388
Uch Kochoy	1241.363
Kara Oi	2532.663
Kluchevka	6717.786
Kirov Reservoir	8954.119

2.9.2. MODIS Snow Cover

The Earth Observing System (EOS) Terra and Aqua satellites launched in December, 1999 and May, 2002 are equipped with Moderate Resolution Imaging Spectroradiometer (MODIS) along with other sensors. MODIS is capable of providing images of earth surface and clouds in 36 spectral bands ranging between 0.4 – 140 µm. The MODIS band 4 (0.545 – 0.565 µm) and band 6 (1.628 – 1.652 µm) are used to calculate Normalized Difference Snow Index (NDSI) by automatic snow map algorithms using the formula shown in eq. (6). The data time series of Terra and Aqua satellites starts from 24 February, 2000 and 4 July, 2002 which is made publicly available by National Snow and Ice Data Center (NSIDC) (Hall et al. 2002).

$$NDSI = \frac{Band\ 4 - Band\ 6}{Band\ 4 + Band\ 6} \tag{6}$$

Snow cover is a major source of fresh water in Central Asia (Dietz et al. 2013). As the network of the weather stations with information about snow cover, height are not available in the study area and the data collected at one station is also inconsistent, the adaptation to remotely sensed data is a good alternative. In this project MODIS Terra Daily Snow Cover (MOD10A1) and MODIS Aqua Daily Snow Cover (MYD10A1) products are used. The datasets have global coverage at spatial resolution of 500 meter grids and are available in Sinusoidal Map Projection. In clear sky conditions the accuracy of snow cover extent is 93 % (Riggs et al. 2006). The study area is covered by H23V04 tile as shown in Figure 87 in Appendix A.

2.9.2.1. Terra versus Aqua

NDSI is calculated by taking the difference between infrared reflectance of snow in visible and shortwave radiations. The difference is calculated between MODIS band 4 (0.55 µm) and band 6 (1.6 µm) in case of data from Terra satellite. As the band 6 detector failed on the Aqua satellite shortly after the launch, band 7 (2.1 µm) is used to calculated NDSI for Aqua. Another drawback with Aqua data is that the NDSI / NDVI estimation of snow cover in vegetated regions was cancelled due to large overestimation of snow resulting from the use of band 7 (Riggs et al. 2006).

Cloud coverage is a main problem in analyzing snow cover maps and it is difficult to find clear sky conditions especially in winter when it is most important to estimate snow cover extent.

2.9.2.2. Pre-processing of MODIS

Pre-processing of the raw data was performed to extract the study area out of world images in ArcGIS. Missing days and clouds were removed by sensor and temporal combination in MatLab before finally using it for accuracy assessment. These methods are further explained under the next three headings.

2.9.2.2.1. Study Area Extraction

The data was initially processed in ArcGIS to extract the study area and change the projection system with the help of a small iterative model designed to carry out the following steps. A sketch of the model can be seen in Figure 88.

1. Make a raster catalog and load raw data into the catalog.
2. Read raster images from the catalog by Raster Iterator.
3. Calculate date of each file from the original name using Calculate Value tool and give it as precondition to Project Raster tool.
4. Project files from sinusoidal projection to Geographic Coordinate System WGS-1984. Use "MAJORITY" as resampling technique to keep pixel value intact. Set a unique output name for each file by giving date number calculated in previous step as part of name.
5. Extract study area from world image using Extract by Mask tool and Talas boundary file.
6. Convert the file from raster to text format and save with unique date numbers.

2.9.2.2.2. Sensor Combination

The next step was to have a sensor combination. If MODIS Terra data was missing for a day, it was replaced by data from MODIS Aqua sensor. In case data was available from both sensors, Terra data was preferred because of errors present in Aqua time series as described before. The sensor combination method has been used in studies before and is reported to reduce accuracy by 1.4 % for a pixel (Dietz et al. 2013). The missing data for 18 different days was substituted from Aqua satellite. The data from both sensors was missing for 50 days in the years 2000, 2001 and 2002. These days were ignored in the snow cover accuracy assessment.

2.9.2.2.3. Temporal Combination

Clouds were removed by performing a three day temporal combination of the data. It was done in MatLab using a small model that checked each pixel for presence of clouds. In case clouds were present on a particular day, the pixel value was checked for the previous and future days for land, snow or lake information. If any of the mentioned three code values had occurred, the pixel code of cloud was replaced by that value. The data for this day was overwritten and saved so that while examining cloud cover for the upcoming day, the overwritten data was used instead of raw data for the previous day. In case the model did not find other information, the cloud value was left unchanged.

2.9.2.2.4. Snow Cover Efficiency

The accuracy of simulated snow cover was found by comparing it with MODIS snow cover images on a pixel to pixel basis. The model generates snow cover maps at daily time step. The accuracy was also calculated for each day by comparing every pixel of the modeled snow cover image with corresponding MODIS image pixel and classifying it as correctly predicted or not correctly predicted. The correctly predicted pixels are added to find the total number. The snow cover efficiency is calculated by using equation (7).

$$S_{eff} = \frac{No.of\ Correctly\ Predicted\ Pixels}{Total\ Pixels\ in\ Catchment - No.of\ cloudy\ pixles} \times 100 \qquad (7)$$

Where S_{eff} is snow cover efficiency, the numerator is the total number of correctly predicted pixels, the first element in the denominator is the total number of pixels in the catchment and the second element is the number of pixels covered with clouds in MODIS observed data. A full time series of daily snow cover efficiency was created in this way and mean snow cover efficiency was calculated.

Chapter 3

3. Input Data Analysis

3.1. Monthly Temperature

Variation in the maximum, minimum and average temperatures observed at Talas meteorological station is shown in Figure 17. A quick look on the graph shows colder winter periods in the years 2001, 2006, 2008 and 2012.

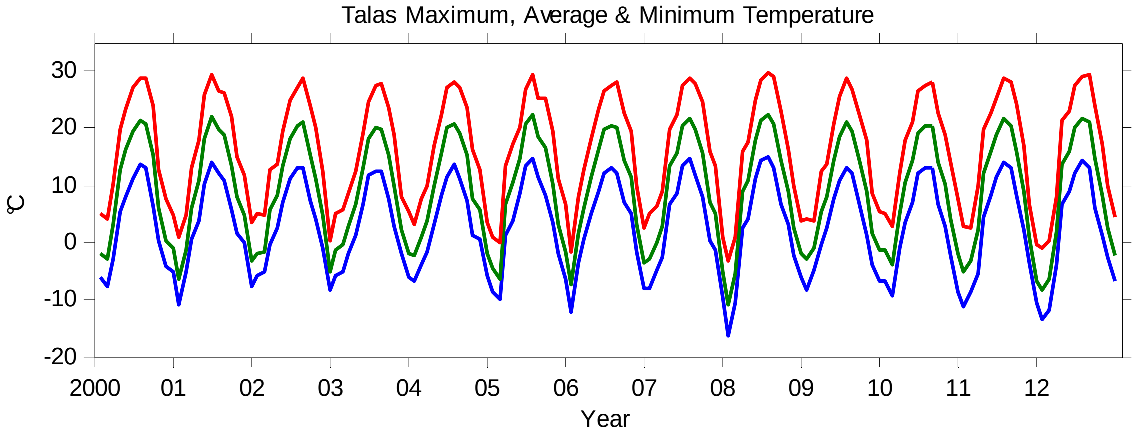

Figure 17: Annual cycle of maximum, minimum and average temperatures in Talas Valley from 2000 to 2012. The maximum temperature is shown by red line, average temperature by green line and minimum temperature by blue line. The graph is made by taking monthly averages of each temperature category.

The average temperature slowly rises from -2 °C in February to 21 °C in July followed by a constant decline to below freezing point in December. It reaches its lowest value in January when the average temperature is -4 °C. This is shown in the bar graph in Figure 18 made by calculating long term monthly means from 2000 to 2012. The mean maximum temperature occurs in July when it is 28 °C and the mean lowest temperature is -9 °C observed in the month of January.

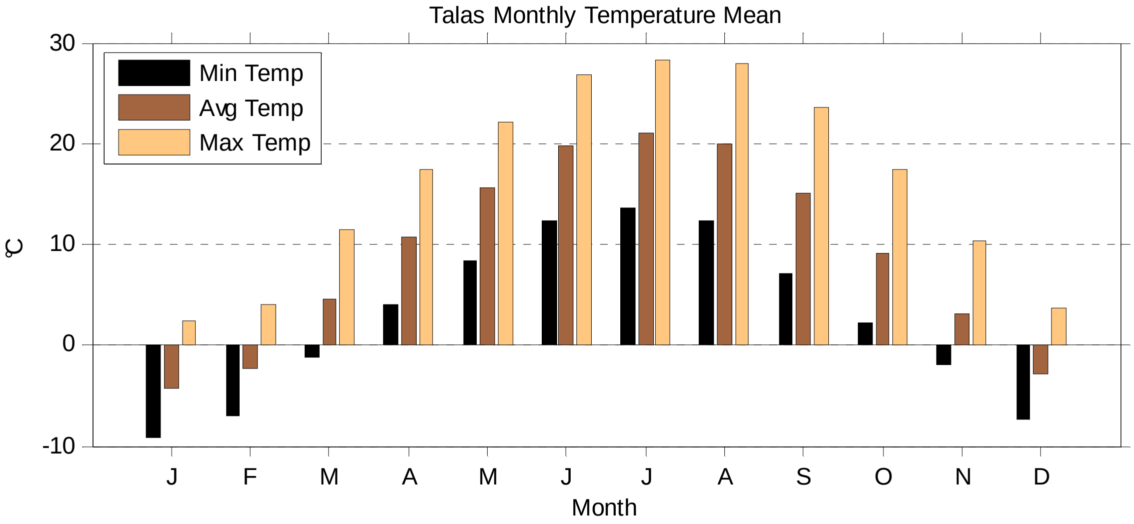

Figure 18: Long term mean of maximum, minimum and average temperatures in Talas Valley. The values are monthly averages for a period of 13 years starting from 2000 to 2012.

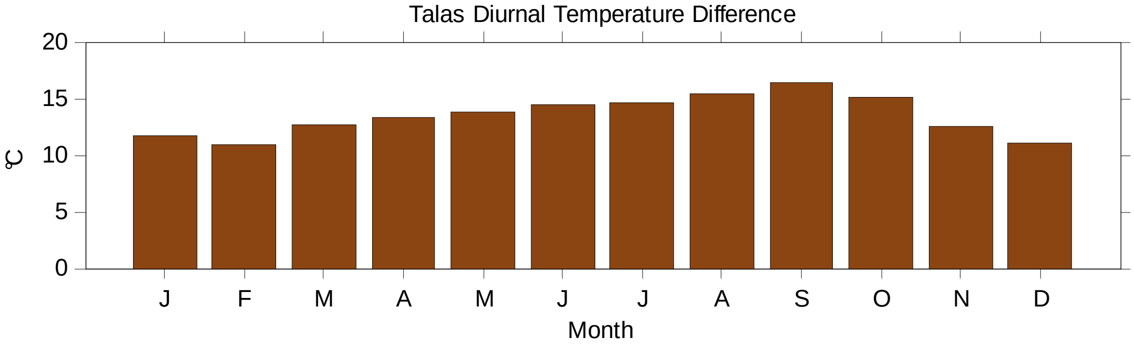

Figure 19: Diurnal temperature difference for each month in Talas Valley. The graph is made by subtracting long term means of the minimum temperature from the maximum temperature on monthly basis.

The mean diurnal temperature difference in each month is shown in Figure 19. It is highest in September with a temperature difference of 16 °C and lowest in February with a temperature difference of 10.9 °C. The strong diurnal variation in daily temperature results in snow melt at temperature higher than the melting point of ice.

3.2. MODIS Snow Cover

The MODIS data was prepared for accuracy assessment by sensor and temporal combinations as explained in the data preparation chapter. The extent of clouds removed is shown here with the help of a bar graph representing percentage of clouds present in the data before and after temporal combination. Figure 20 shows that the method adopted serves well in removing clouds and only few days with clouds are left.

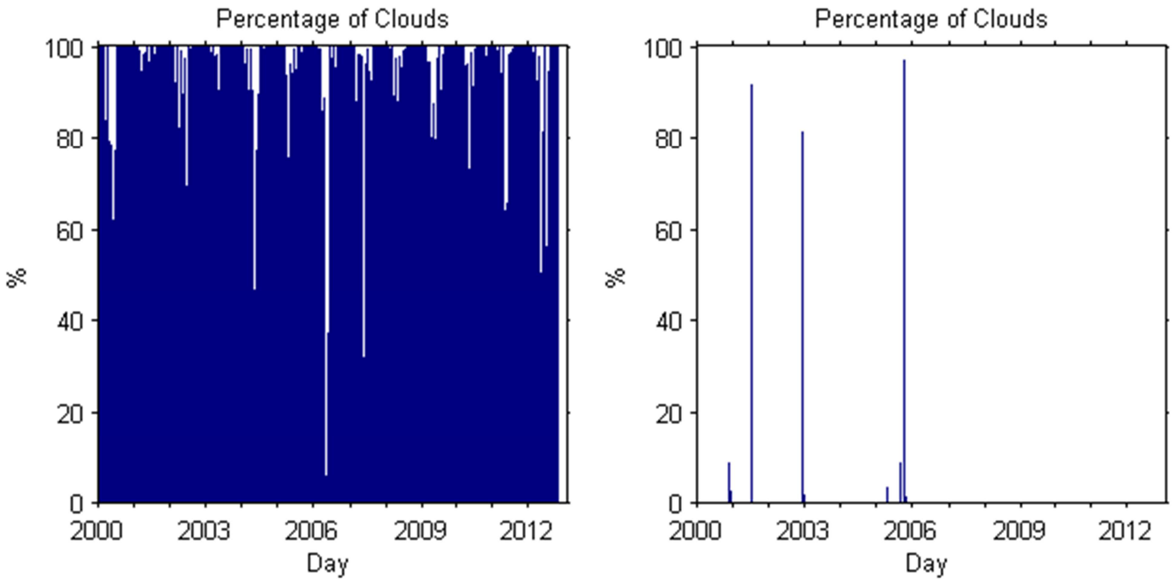

Figure 20: Percentage of clouds in MODIS data after sensor combination (left graph) and temporal combination (right graph).

The extent and distribution of clouds in the study area is pictorially presented in Figure 21 to Figure 23. They are generated after calculating “MODE” for each pixel from 2000 to 2012 i.e. the most repeated value for each pixel throughout the time series. The study area was largely covered with clouds with the exception of four months from July to October. But these months are least important in determining seasonality of snow covered area as the catchment is mostly snow free during this time of the year. Hence it was important to process and remove the clouds from MODIS data in order to have accuracy assessment of snow covered area.

One problem with this method is that if there is an error in the previous or the future day information, it will be propagated into the data. But because each day there is a new picture available and the model continuously checks for the future day information also, the error will not persist for long time unless there is a long series of cloudy days.

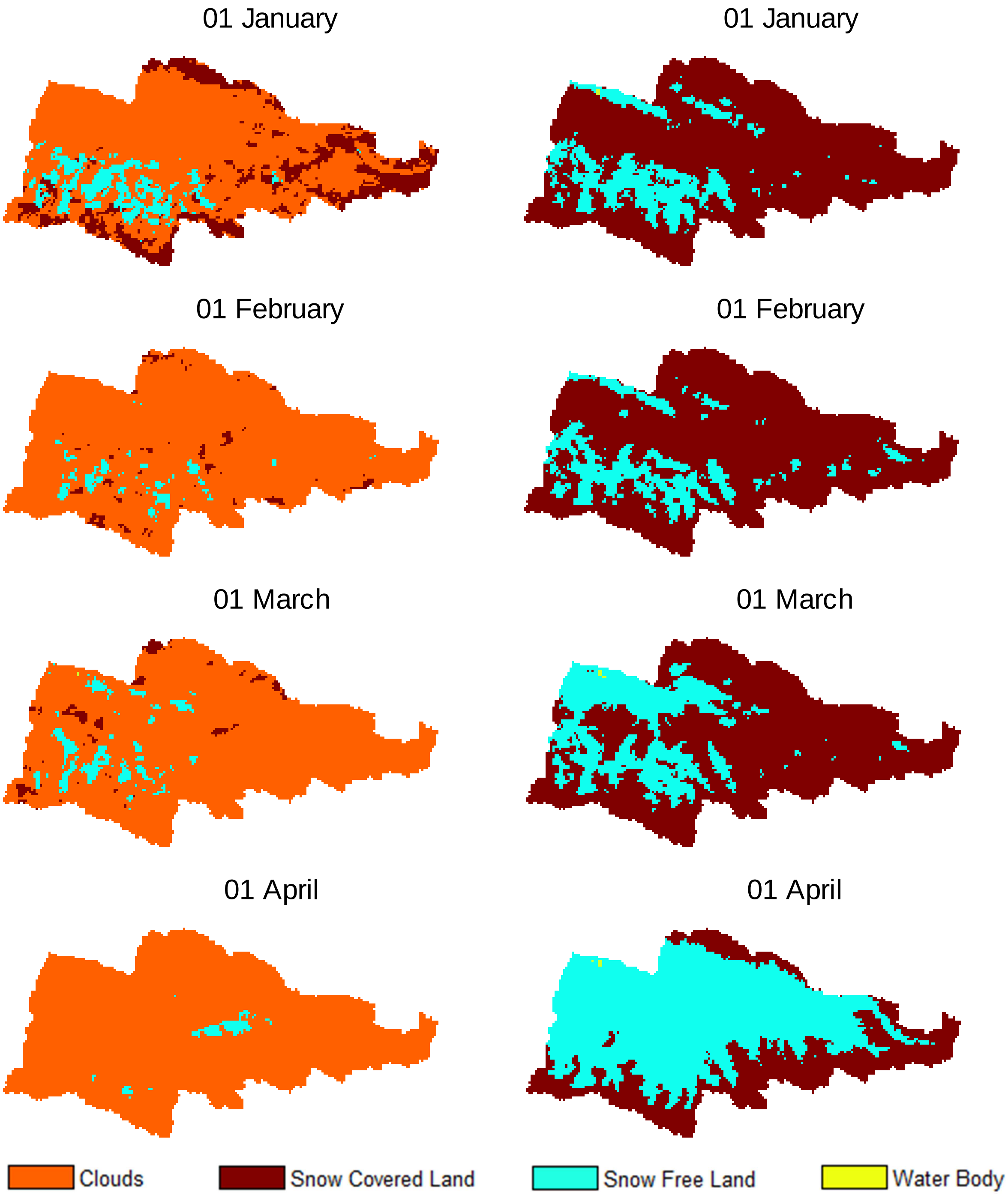

01 January

01 January

01 February

01 February

01 March

01 March

01 April

01 April

Figure 21: MODIS Snow Cover before (left column) and after Temporal Combination (right column) from January to April. The graphs are made after calculating mode for each pixel from 2000 to 2012.

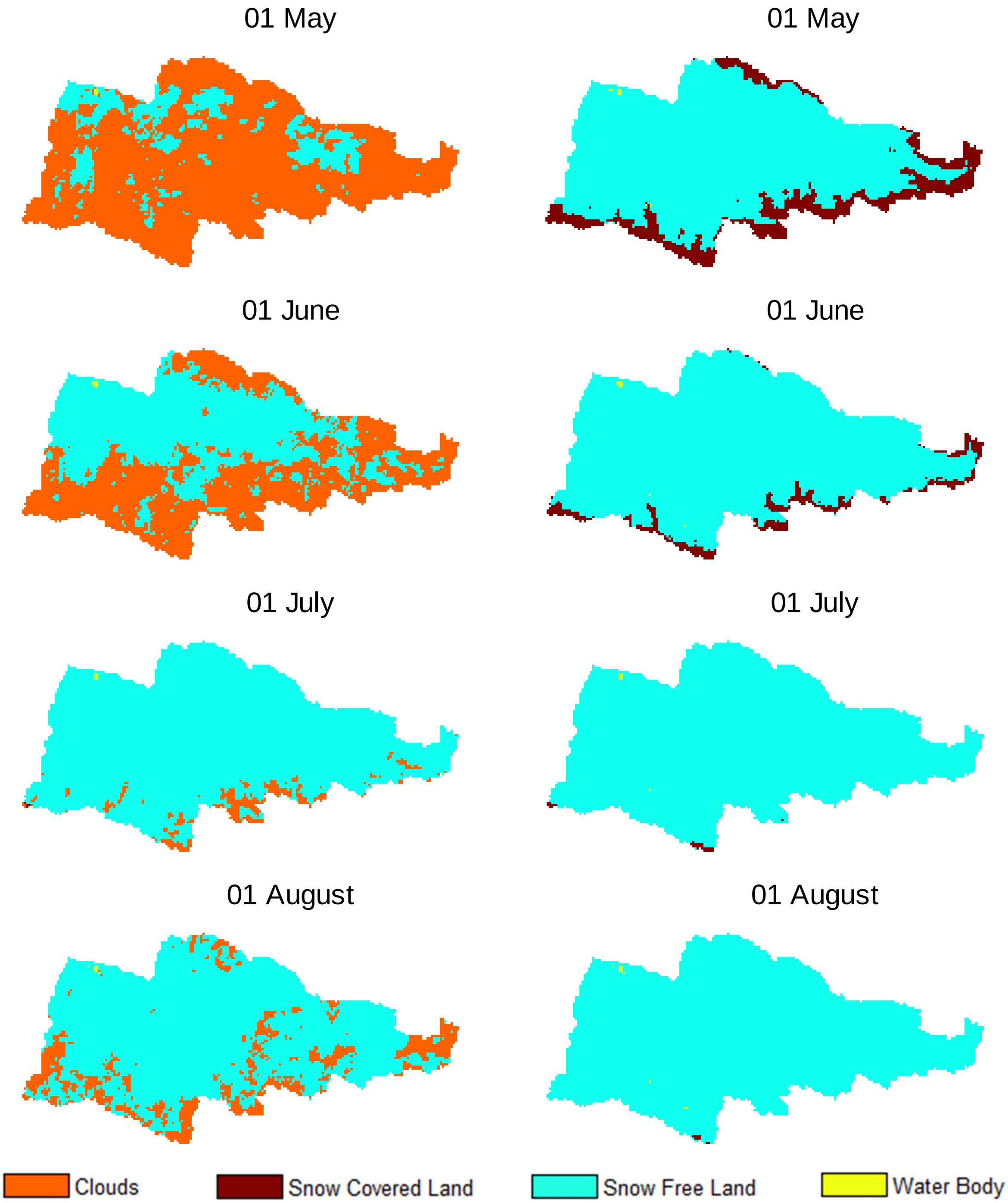

Figure 22: MODIS Snow Cover before (left column) and after Temporal Combination (right column) from March to August. The graphs are made after calculating mode for each pixel from 2000 to 2012.

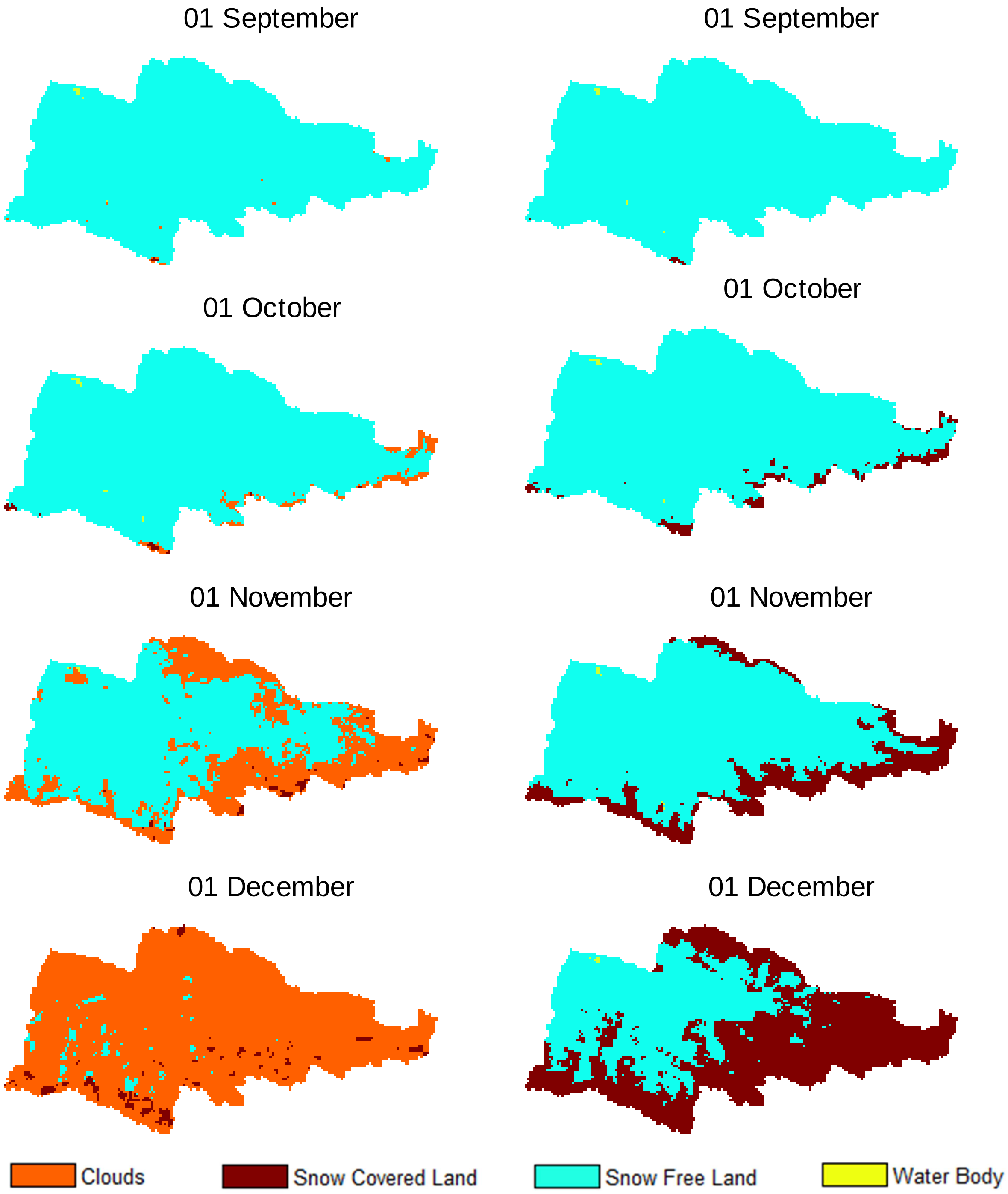

Figure 23: MODIS Snow Cover before (left column) and after Temporal Combination (right column) from September to December. The graphs are made after calculating mode for each pixel from 2000 to 2012.

3.3. Global Irradiance

The global irradiance (I_G) is calculated from a combination of global clear sky irradiance (I_{GCS}) and cloud transmissivity (CT) correction. TE employs methods explained in (Corripio 2002, 2003) to calculate I_{GCS} and CT parameterizations as described in (Pellicciotti 2004).

I_{GCS} depends on several parameters like position of sun relative to the study area, extraterrestrial solar radiation, direct and diffuse sunlight depending upon zenith angle, shading effect depending upon solar position, topography of the area etc. The estimation of CT from CFC is described in the data preparation chapter. The CT is further parameterized for each grid cell by a relation depending upon temperature of the grid cell and empirical factors. The decadal average of I_G before and after cloud transmissivity correction is shown in Figure 24 and its spatial distribution is further presented in Figure 25. The average I_G (Figure 25) analysis shows that in general, the I_G is higher at the top of the mountains and is subjected to variations as compared to its consistent intensity in the valley. The hills facing south direction receive

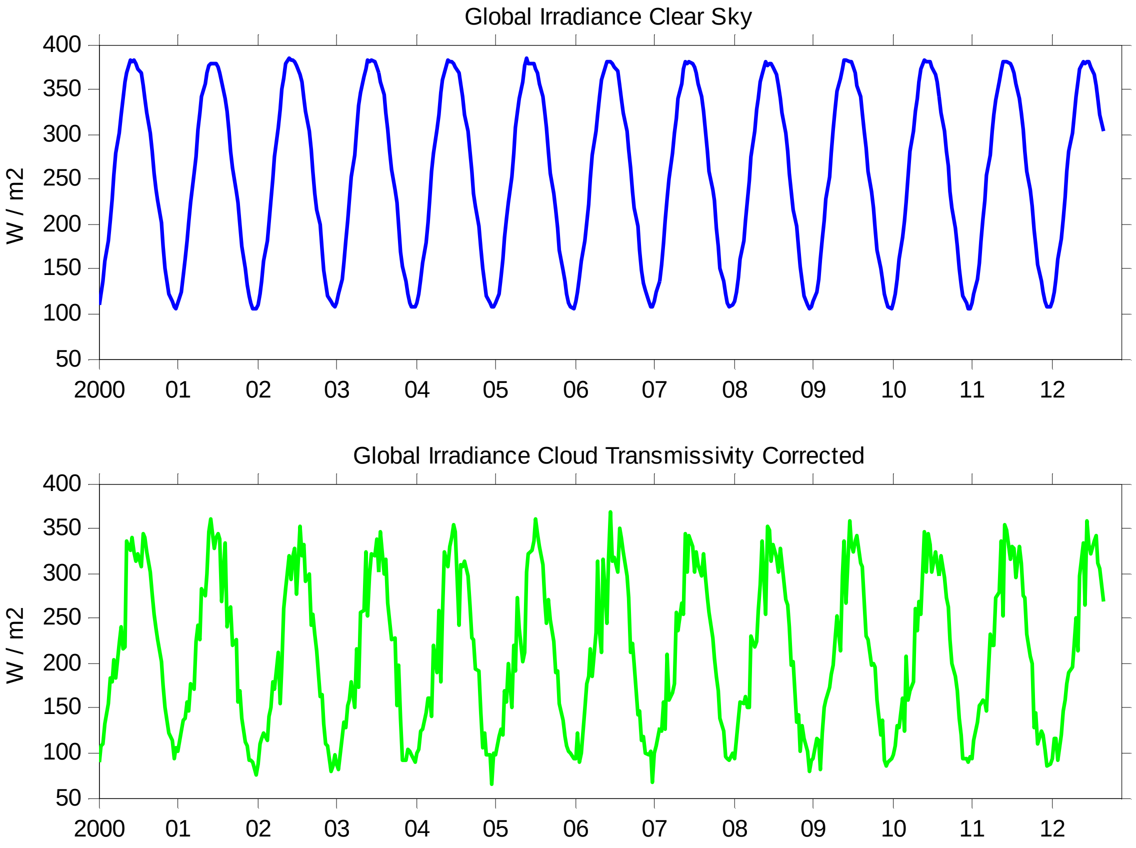

Figure 24: Global Irradiance from 2000 to 2012 plotted as 10 days average. The top graph shows irradiance calculated with clear sky conditions. The bottom graph shows irradiance estimated after correction of cloud transmissivity.

higher sunlight. Regions deprived of I_G are depicted by red spots in the images. They occur due to sunlight blockage and shading effect caused by the hills. There is slight decrease in I_G after taking into account the CT correction.

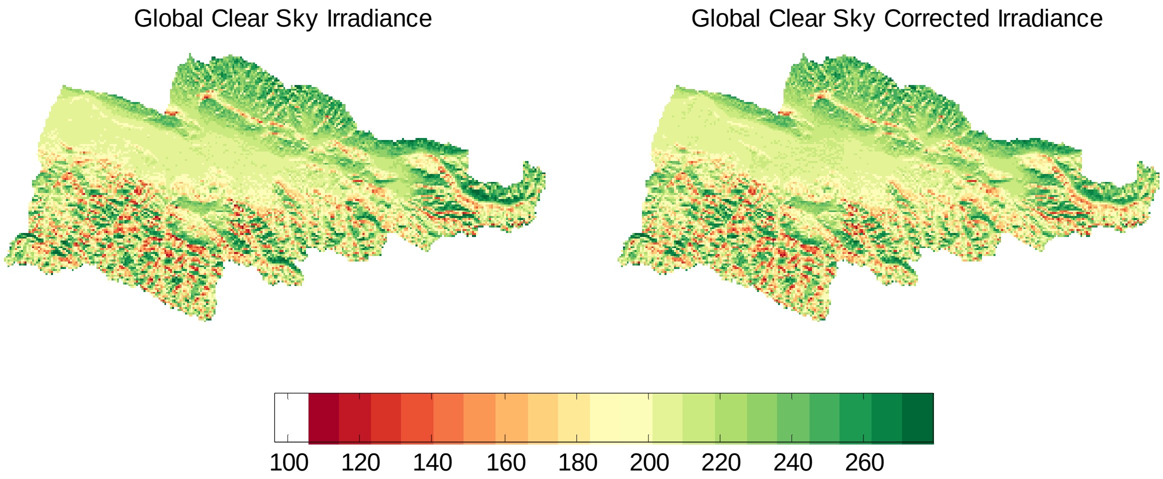

Figure 25: Global irradiance with clear sky and after including cloud transmissivity. The figure shows average daily global irradiance for each grid cell in W/m^2 from 2000 to 2012.

3.4. Mean Decadal Observed Runoff

The long term mean of the observed runoff at mountainous and flood plain gauging stations is presented in this section. The results are compiled after calculating average runoff for each decade from 2000 to 2012.

3.4.1. Mountainous Gauging Stations

The mountainous stations have snow melt as main runoff source. The flow starts to increase with summer rain in April and May with a contribution of water coming from snow-melt. The flow reaches its peak in June and starts declining in the month of July. There is no flash flow from rainfall in October. Please note that the y-axis is different in all of the plots. The flow is highest for Ur Maral post followed by Ak Tash, Besh Tash and Kumush Too. The stations are important in the same order depending on their percentage contribution to the runoff of Talas River.

Mean Decadal Observed Runoff

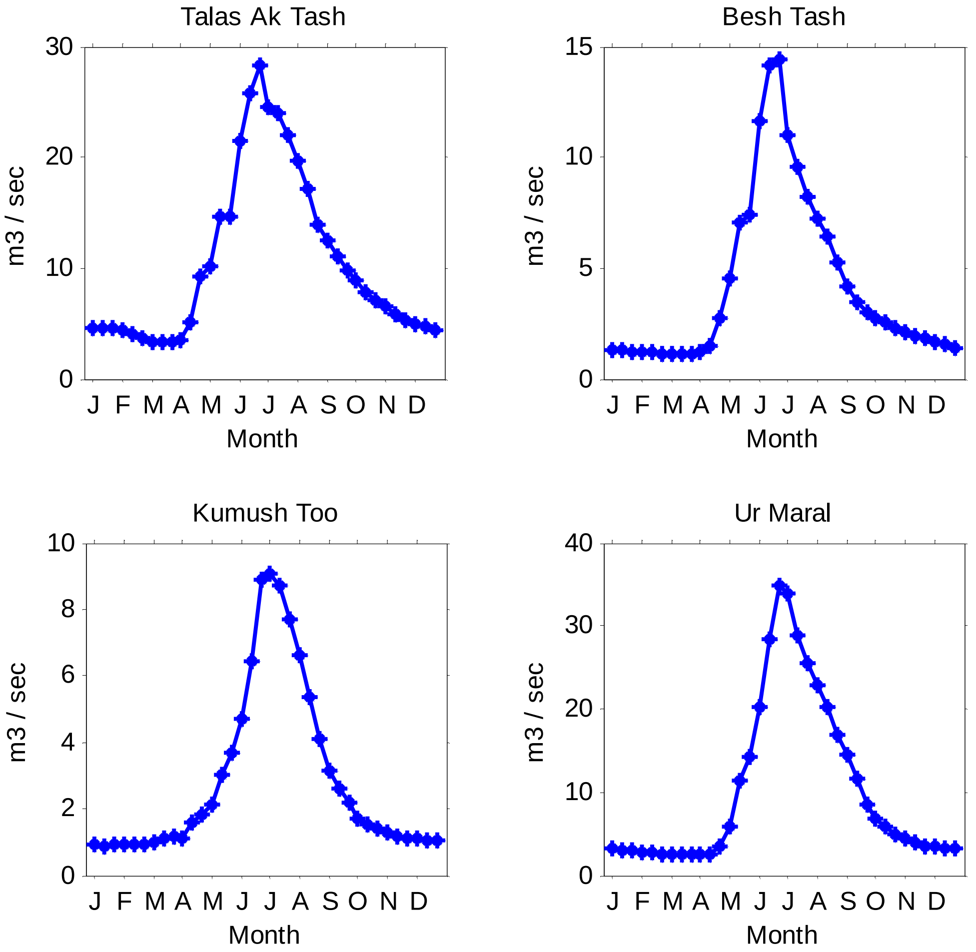

Figure 26: Long term decadal mean of observed runoff for mountainous gauging stations. The plots have been made after estimating average runoff for each decade throughout the time series from 2000 to 2012.

3.4.2. Floodplain Gauging Stations

The floodplain gauging stations include Uch Kochoy located at the tail end of the valley with little agricultural area upstream. It has Kara Oi just 2 kilometers downstream with relatively bigger agricultural area on North-East side of the catchment. The Kara Oi station is located downstream of the confluence point of two streams coming from North-East and South-East direction. This can be seen in Talas River Gauging Stations map shown in the Figure 15. The stream coming from North-East side has higher flow and it includes sub-catchment of Ak Task gauging station also. The flow from South-East side is little less than the other stream and Uch Kochoy post is located before the confluence of the two streams. The reason for higher flow at Kara Oi compared to Uch Kochoy, despite of the fact that it is situated only two kilometers downstream of Uch Kochoy, is the addition of water coming from North-Eastern streams.

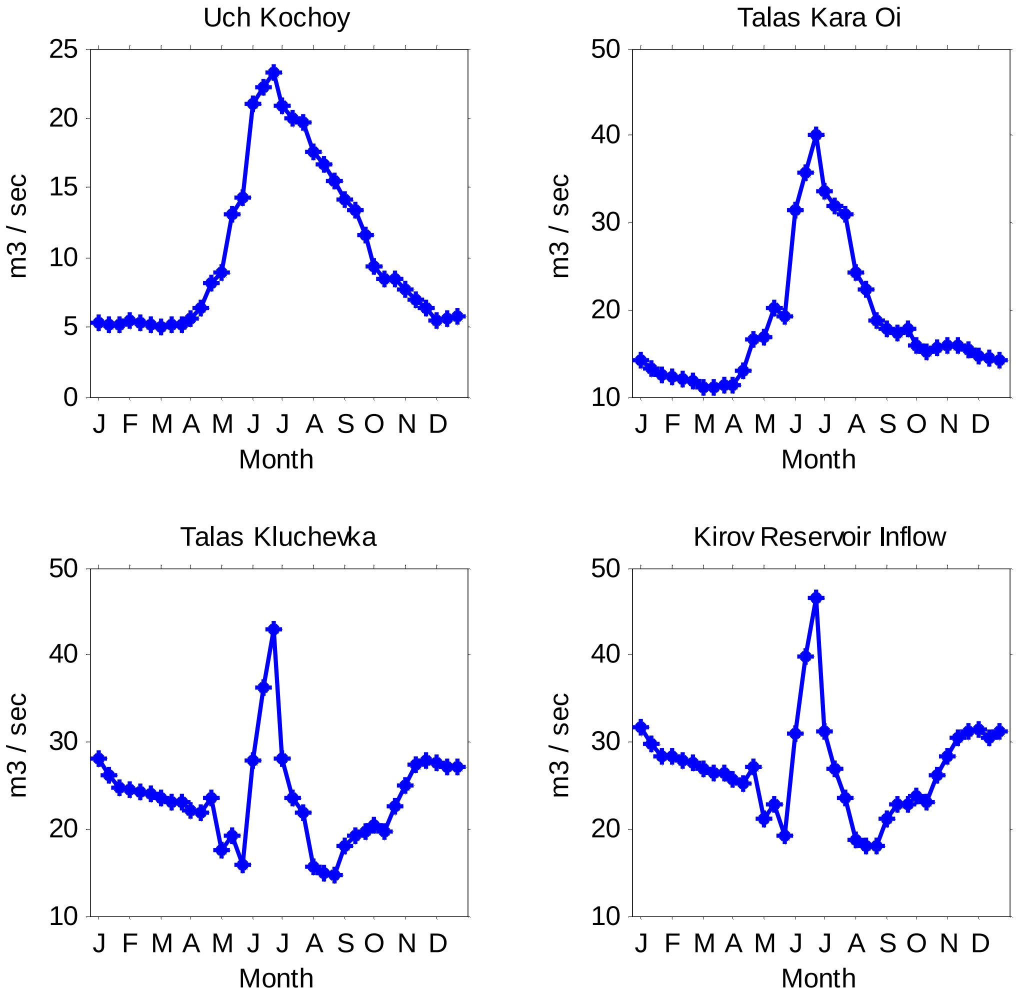

Figure 27: Long term decadal mean of observed runoff for floodplain gauging stations. The plots have been made after estimating average runoff for each decade throughout the time series from 2000 to 2012.

The valley has a huge agricultural area downstream of these two stations where river water is used for irrigation purposes. The Kirov Reservoir is the ultimate destination of water coming from all big or small streams. The runoff measured at Kirov gauging station includes the total loss of water in the catchment due to evapotranspiration. Kluchevka gauging station is located 20 km upstream of Kirov Reservoir. These two stations have identical flow pattern with higher flow at the latter station. The runoff recorded at mountainous posts do not show decline in May and August. This necessarily points towards water abstraction from the river to meet the irrigation and household demands of the communities living in Talas Valley.

The difference in runoffs recorded at Kara Oi and gauging stations located upstream of Kara Oi is shown in Figure 28. The runoff should increase at the Kara Oi station because of water addition from precipitation and groundwater in the area between upstream and downstream stations. The difference in the figure shows that this is not the case because of water abstraction in the agricultural area in the North-East side of Kara Oi sub-catchment. The difference in observed and expected runoffs is small because of little agricultural area in the sub-catchment. Cropland is mainly concentrated in the Kluchevka sub-catchment which results in large difference in observed and expected runoffs for this station as shown in Figure 29. Hence the depression in flow curves in May and August for Kara Oi, Kluchevka and Kirov Reservoir stations is due to water abstraction.

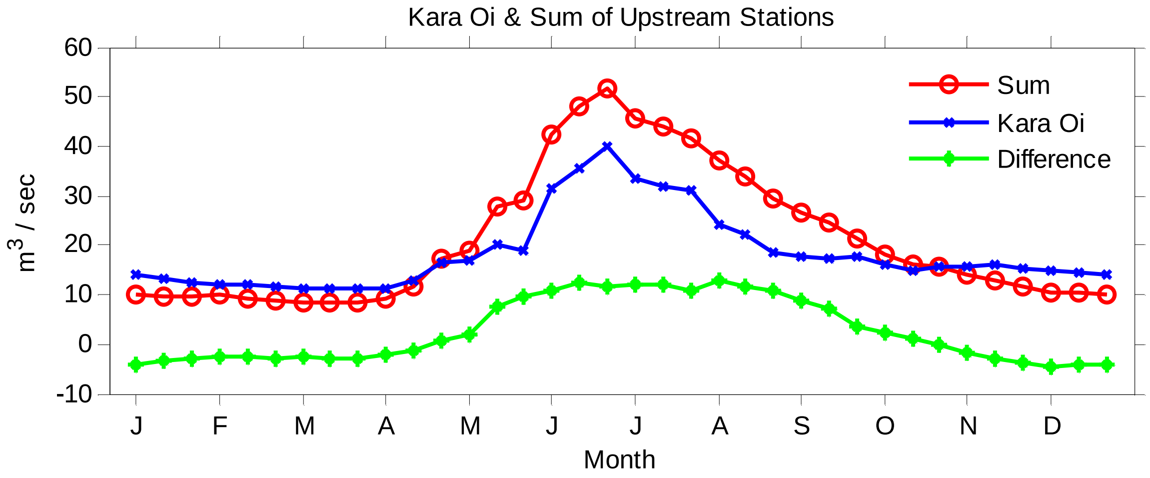

Figure 28: Mean decadal observed and expected runoffs at Kara Oi gauging station. The observed runoff is shown by the blue line. The expected runoff which is sum of the runoffs observed at Ak Tash and Uch Kochoy gauging stations is presented in the red line. The difference in the observed and expected runoffs is shown in the green line.

However the sum of runoffs from upstream stations decreases in winter because of precipitation in solid form there in contrast to precipitation in liquid form in the flood plain area (Figure 62). A big proportion of winter precipitation falling as snow is stored in the snow packs while all of the precipitation in liquid form contributes to runoff of the river which eventually reaches Kluchevka and Kirov Reservoir gauging stations. The water stored in groundwater aquifers and soil layers also contributes to the flow of flood plain stations. This is higher in Kluchevka because of the bigger catchment area meaning that more area can contribute through groundwater and as the station is located in the center of the valley with more chances of precipitation as rainfall.

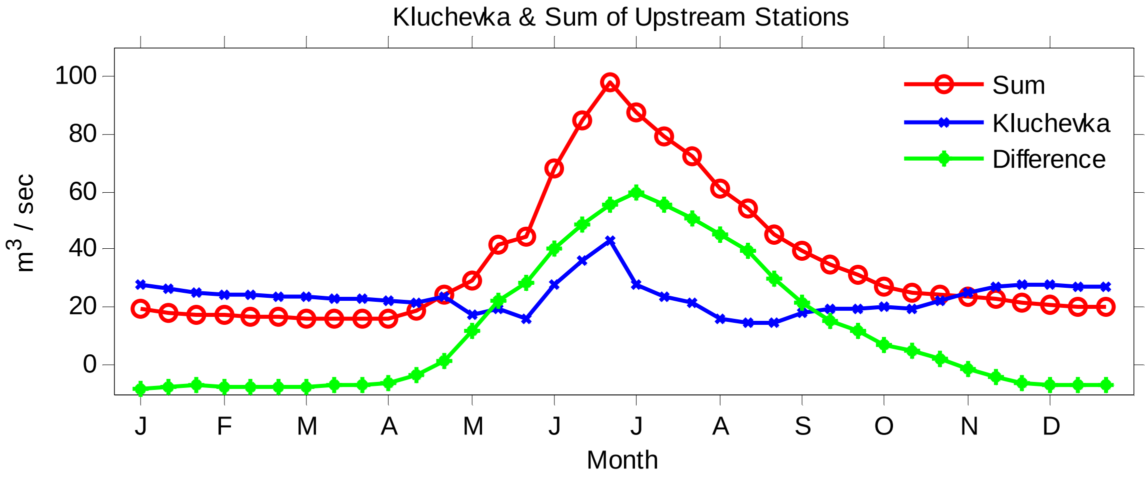

Figure 29: Mean decadal observed and expected runoff at Kluchevka gauging station. The observed runoff is shown by the blue line. The expected runoff which is sum of the runoffs observed at Kara Oi, Besh Tash, Ur Maral and Kumush Too gauging stations is presented in the red line. The difference in the observed and expected runoffs is shown in the green line.

The same graph made for Kirov Reservoir reveals that the difference is either zero or negligible. The expected runoff is calculated by adding the runoffs observed at Kluchevka, Bakianskie, Beisheke, Chimkentskie, Kara Buura and Kirovskie Rodniki gauging stations. The five stations mentioned here are located on the small streams on the north-west side of the catchment. The runoff data was obtained for these stations also but it is unreliable and is not used in the project except at this place only to show that the observed and expected runoffs overlap. This indicates a possibility that the inflow to Kirov Reservoir is calculated by simply adding the runoffs of these stations instead of recording real time flows with a gauge. This cannot be said for sure because according to a personal communication, the inflow to Kirov Reservoir is measured by calculating differences in the volume of the lake with the help of a scale bar which is not a precise method in itself (Mr. Andrey Yakovlev, former KGZHydromet).

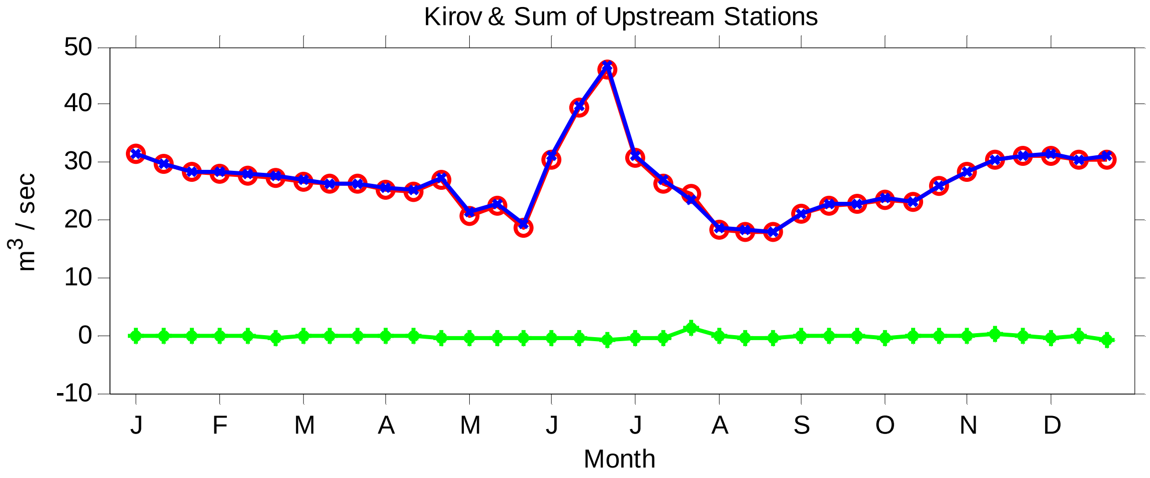

Figure 30: Mean decadal observed and expected runoffs at Kirov Reservoir. The observed runoff is shown by the blue line. The expected runoff and the difference in observed and expected runoffs are shown in the red and green line. These two lines exactly overlap.

3.4.3. Observed Runoff Anomalies

The observed long term decadal means presented in the Figure 26 and Figure 27 were subtracted from the yearly runoffs to produce anomalies graphs. The runoffs time series for all stations can be seen in the Figure 89 to Figure 92 in Appendix B. The figures include graphs for Bakianskie, Beisheke, Chimkentskie, Kara Buura and Kirovshie Rodniki gauging stations also.

The anomalies graphs show that low discharge was observed in the years 2000, 2001, 2006, 2008 and 2012 at all stations. (The data for the year 2006 and 2010 to 2012 is missing for Uch Kochoy station). And the highest runoff was recorded in the year 2002. This has to do with precipitation in the sub-catchment of the gauging stations. The low runoff years are further discussed in details in Chapter 4.

3.4.4. Runoff Seasonality Comparison

The rise in summer flow does not occur at the same time for all stations. A monthly comparison of runoffs is shown in Figure 32 where the differences in start of summer flow and peak flow timing can be observed. The three stations Ak Tash, Uch Kochoy and Kara Oi located on the eastern side of the study area show increase in runoff in April. It continues to rise till the month of June and starts declining in July. The runoff increases one month later for the stations Ur Maral, Kumush Too and Besh Tash located on the southern side.

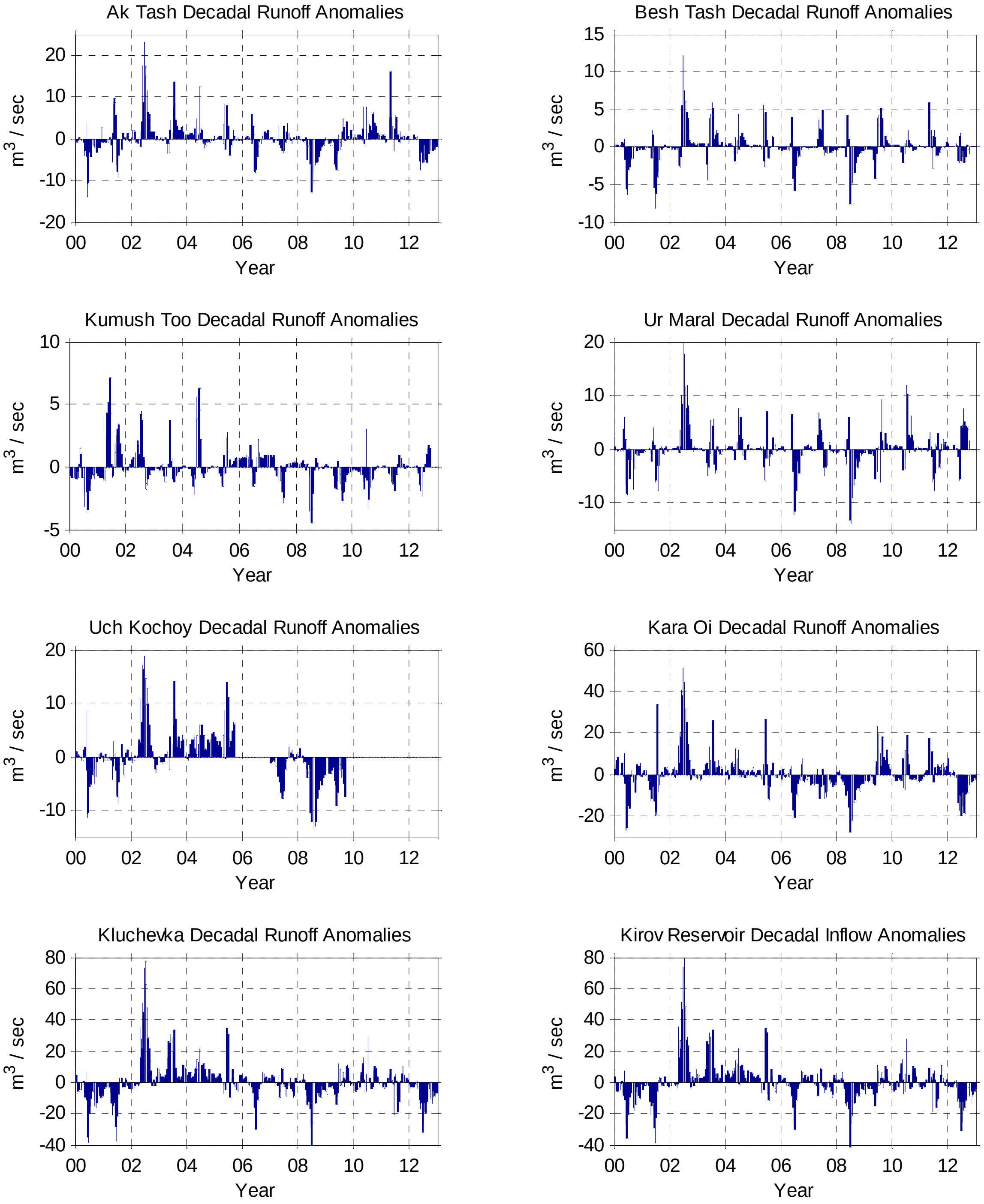
Ak Tash Decadal Runoff Anomalies

Besh Tash Decadal Runoff Anomalies

Kumush Too Decadal Runoff Anomalies

Ur Maral Decadal Runoff Anomalies

Uch Kochoy Decadal Runoff Anomalies

Kara Oi Decadal Runoff Anomalies

Kluchevka Decadal Runoff Anomalies

Kirov Reservoir Decadal Inflow Anomalies

Figure 31: Anomalies in average decadal observed runoff at all stations. The bars represent ten days average values in m^3 / sec. Negative anomalies are significant in the years 2000, 2001, 2006, 2008 and 2012. And year 2002 shows high positive anomaly for all stations.

The peak runoff time for Kluchevka, Kara Oi, Uch Kochoy, Ak Tash and Besh Tash is same and occurs in the month of June. While the peak runoff occurs in the month of July in case of Kumush Too and Ur Maral which are located in a different soil zone. The water volumes of mountainous stations are dependent on their catchment area. The bigger the catchment size, the larger is the water volume. This can be seen in Figure 32 also. Ak Tash and Ur Maral have higher flows because they have larger catchment areas while Besh Tash and Kumush Too have comparatively less flow because their catchment areas are small. The location of gauging stations and their catchment areas can be seen in Figure 16 and Table 5.

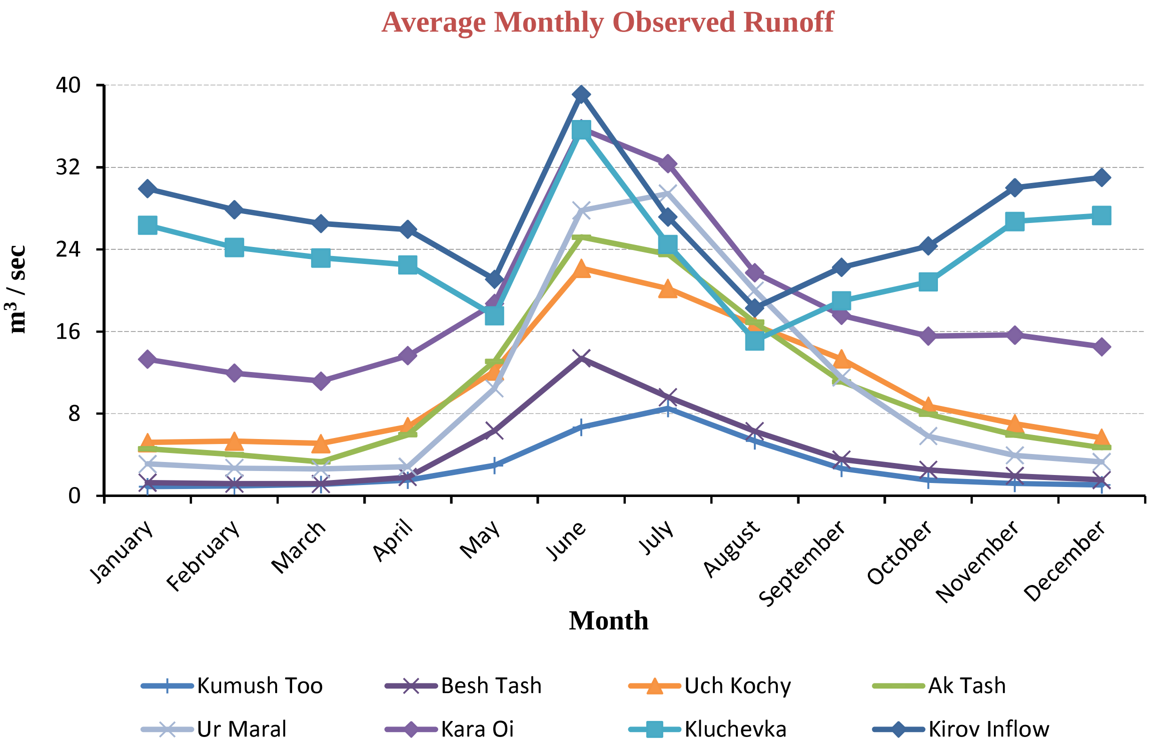

Figure 32: Monthly averages of observed runoff in 13 years. The graph shows seasonality comparison of increase and peak time of summer runoff among different stations.

The difference in summer runoff start time between Ak Tash and Ur Maral is because of their location in different regions. These two stations have higher flow as compared to the other mountainous stations. Ak Tash is located on north-east side while Ur Maral lies on the southern side. The east side of study area generally receives higher precipitation in the summer and winter that can be seen in TRMM precipitation spatial distribution maps (Figure 44).

3.4.5. Kirov Reservoir Inflow and Outflow

The decadal inflow observed at Kirov Reservoir is shown in the last section together with runoff observed at other gauging stations. This section presents a comparison of inflow, outflow and water volume observed at Kirov Reservoir on the basis of monthly averages. The outflow from Kirov is little in the beginning of the year and increases gradually till summer. It is maximum in the months of May, June, July and August and decreases again with time to merely 8 m^3/sec in December. As Kirov Reservoir is built to meet irrigation demands of a huge agricultural area downstream in Kazakhstan, water is released form the dam in summer when the irrigation demand is at its peak. The outflow is small during winter and is mainly used to prevent salinization. The study area is semi-arid and the large evapotranspiration rate causes the salts to rise to the soil surface by capillary transport and accumulate there. Water is released in winter to flush or leach these salts out of the soil.

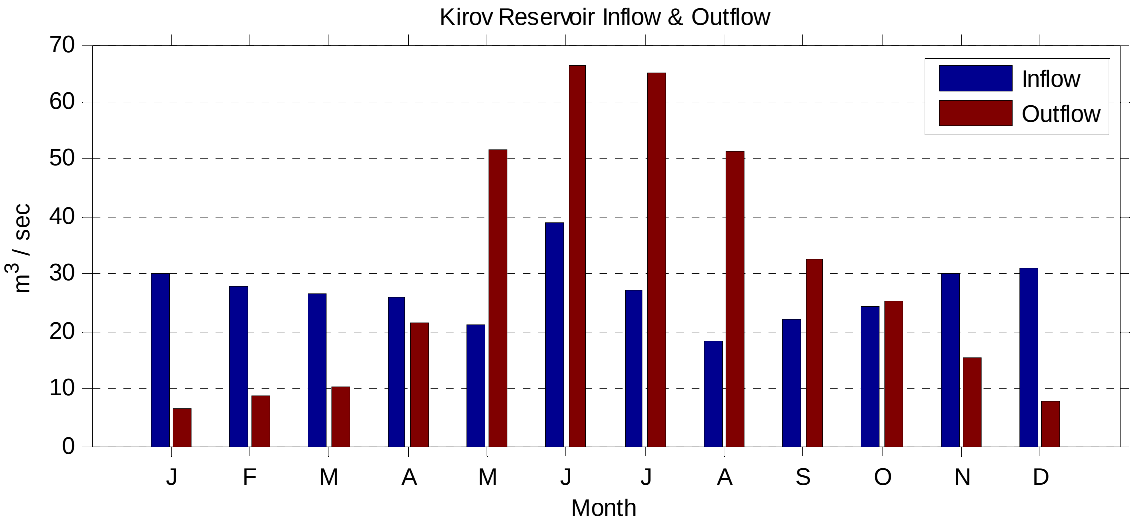

Figure 33: Observed inflow and outflow at Kirov Reservoir. The values represent monthly averages of data from 2000 to 2012. The outflow is higher in summer for irrigation of agricultural land in Taraz city, Kazakhstan.

This is in agreement with the water volume recorded at the reservoir as shown in Figure 34. The inflow to the reservoir is high in winter and this water is stored in the dam. The water volume continuously rises from November to April in the reservoir. From May to August a large volume of water is released to the downstream agricultural area. The inflow is also not very high in these months because of water use for irrigation in Talas Valley. Therefore the water volume stored in the reservoir slowly declines to the minimum level in October.

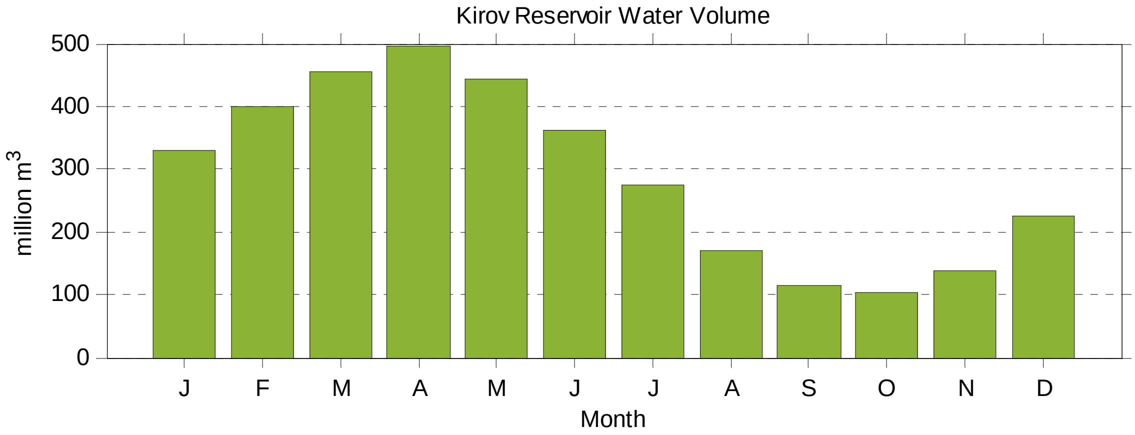

Figure 34: Water volume recorded at Kirov Reservoir. The values represent monthly averages of data from 2000 to 2012. The volume reduces in summer due to water release for irrigation.

3.5. Observed and Remotely Sensed Precipitation

3.5.1. Daily and Monthly Correlation

A comparison between observed precipitation and TRMM precipitation for the pixel where Talas meteorological station is located was done. The data was analyzed for the overlapping period of four years from 1998 to 2001 and scatter plots were made. The results show that there is low correlation between the two datasets at daily time scale and the RMSE is high. The values are also concentrated corresponding to precipitation of 1, 2 and 3 mm etc. as shown in the top left plot in Figure 35. A scatter plot between monthly averaged precipitations on the other hand gives good correlation and low RMSE. The same trend was observed when scatter plots between CMORPH and gauge observed precipitations were made. The correlation and RMSE are 0.0093 and 3.9 for daily precipitation respectively. The correlation increases to 0.3 and RMSE decreases to 2 when average monthly precipitation is compared (Figure 36). The correlation is not strong but still it is better than the correlation at daily time scale.

The accumulated monthly observed and TRMM precipitation was also calculated in order to compare it with GPCC data. Scatter plots were made between GPCC and observed precipitation (left plot, Figure 37) and TRMM and observed precipitation (right plot, Figure 37). The correlation is good in both cases.

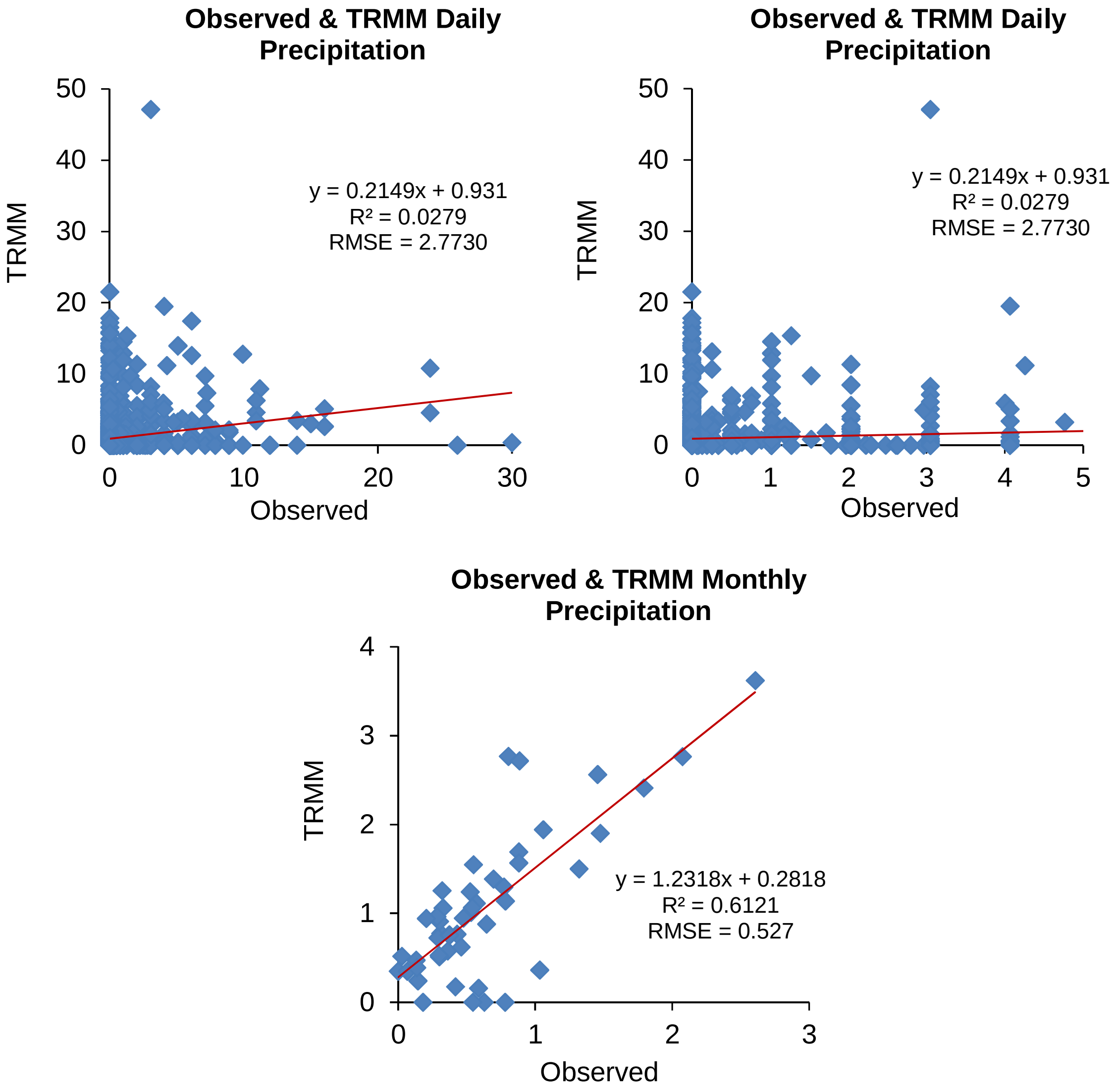

Figure 35: Scatter plots between gauge observed and TRMM precipitations using four years of data from 1998 to 2001. The top scatter plots are between daily values. The x-scale is limited in the top right plot. The bottom scatter plot is between monthly averaged precipitations.

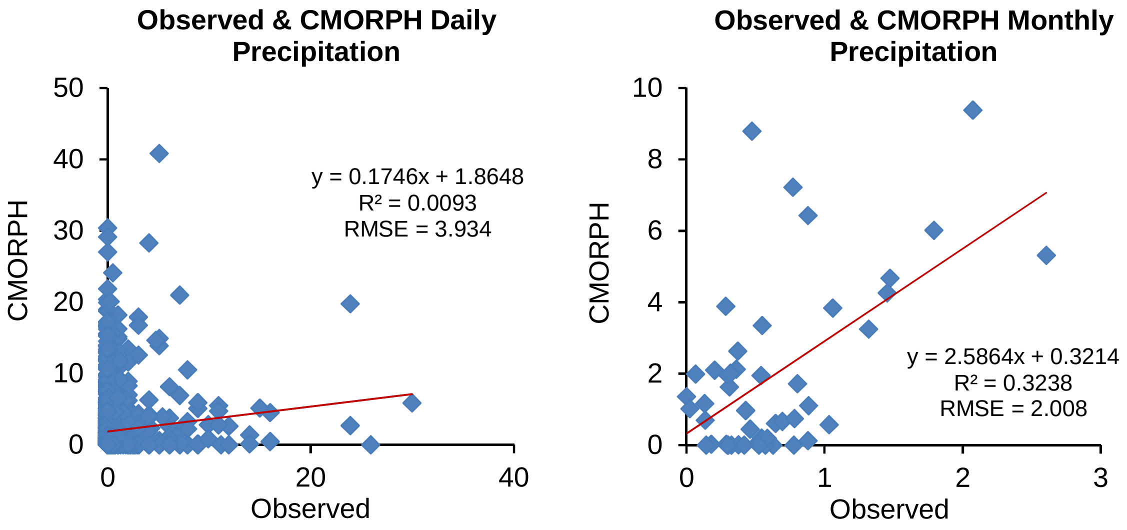

Figure 36: Scatter plots between gauge observed and CMORPH precipitations using four years of data from 1998 to 2001. The left plot is between daily values while the right one is between monthly averaged precipitations.

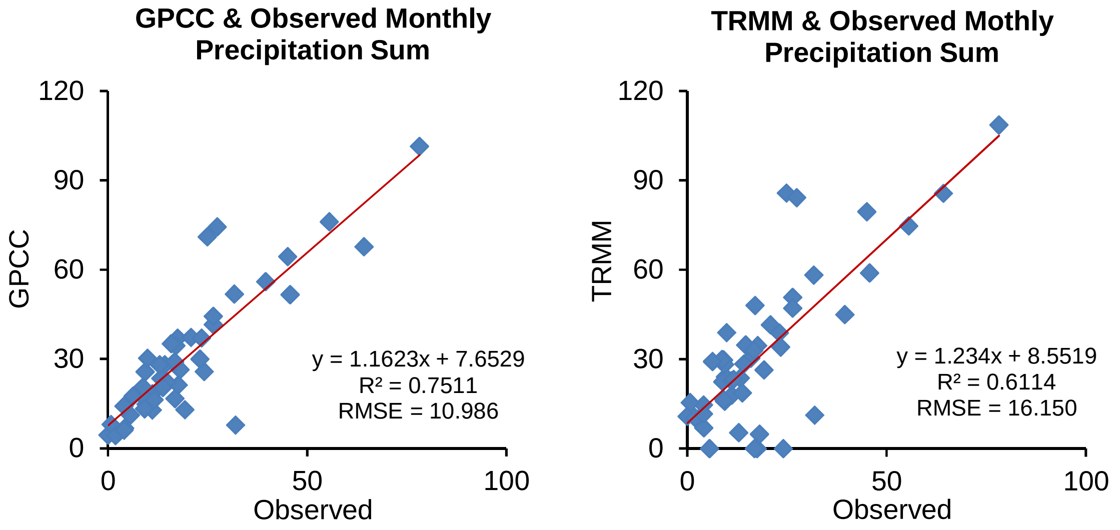

Figure 37: Scatter plots between observed, GPCC and TRMM precipitations using four years of data from 1998 to 2001. The plots are made between accumulated monthly precipitations of each dataset.

3.5.2. Mean TRMM and CMORPH Precipitation

Figure 38 shows a comparison of daily precipitation averaged for each month over a four year period. It is clear from the figure that CMORPH has large overestimation error. TRMM is also overestimating but the difference is less and it is following the seasonality of the observed precipitation which CMORPH fails to do.

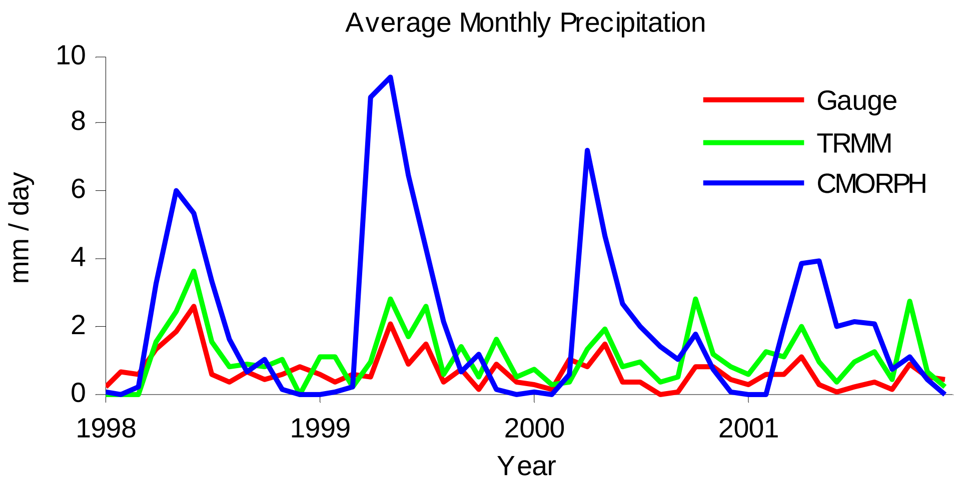

Figure 38: Monthly averaged daily precipitations from gauge, TRMM and CMORPH datasets. The data is compared for an overlapping period of four years. CMORPH has large overestimation error.

A further comparison of TRMM and CMORPH average daily precipitations from 1998 to 2012 is shown in the map in Figure 39. The map is made by using the same legend and it can be seen that the result obtained from these two products is different. CMORPH is overestimating precipitation in most of the region. For example, if the North-East region of the study area is considered, the precipitation from TRMM in this area is 1.12 mm / day while from CMORPH it is 1.77 mm / day. The overestimation is 0.65 mm / day which means it will be 19.5 mm / month and 237.25 mm / year of extra precipitation. This is even larger than the actual precipitation recorded in Talas valley which is 196 mm / year.

Hence these two comparisons clearly show that the CMORPH product has an overestimation error which makes it unsuitable for further use in the project. However a bias correction was applied to the TRMM data as it is also overestimating.

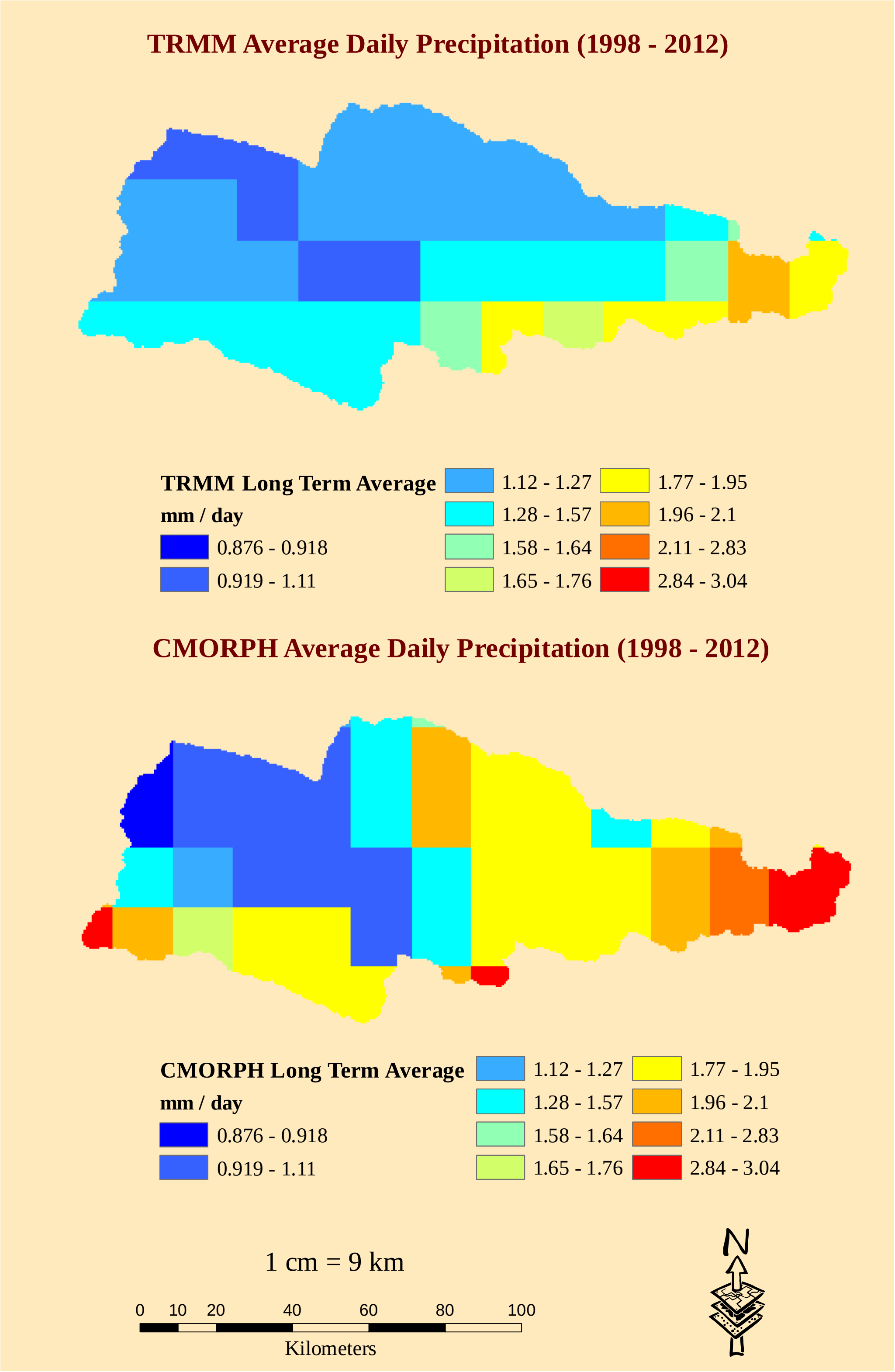

Figure 39: Spatial distribution of TRMM & CMORPH mean daily precipitations from 1998 to 2012. The map shows comparison between satellite precipitation estimates form the two products. CMORPH has considerable overestimation error that is significant on the north-east corner of the catchment in this map.

3.5.3. Bias Correction

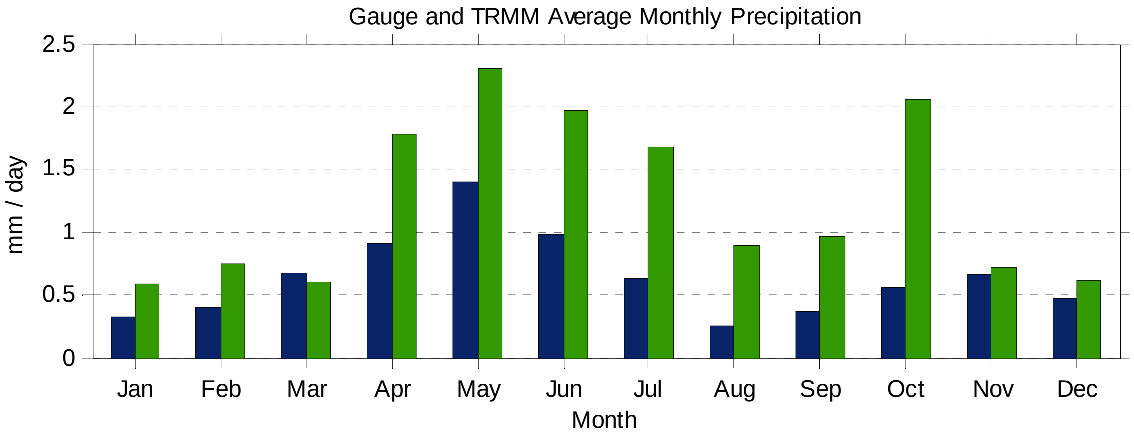

Figure 40: Average daily precipitation in each month according to rain gauge and TRMM data. The average is taken for a time period of four years from 1998 to 2001. The observed and TRMM data are represented by blue and green bars.

Bias correction was done using GPCC and gauge observed data. The concept of bias correction was explained in the second chapter. It was important to bias correct the TRMM data to account for overestimation observed in it. The average monthly precipitation from gauge and TRMM is shown by a bar graph in Figure 40. The study area receives higher early summer and winter precipitation. The overestimation is high from April to October.

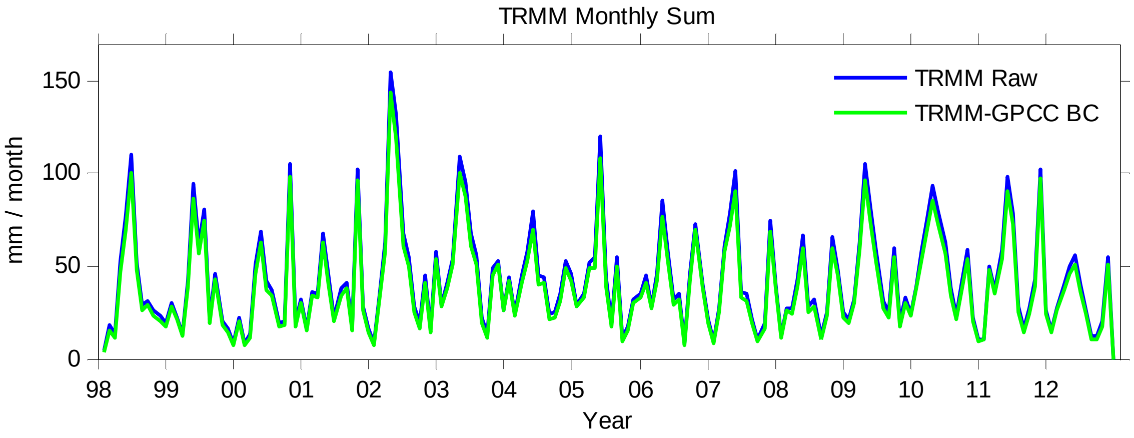

Figure 41: Accumulated monthly precipitation before and after GPCC bias correction. TRMM raw and corrected precipitations are represented by blue and green lines.

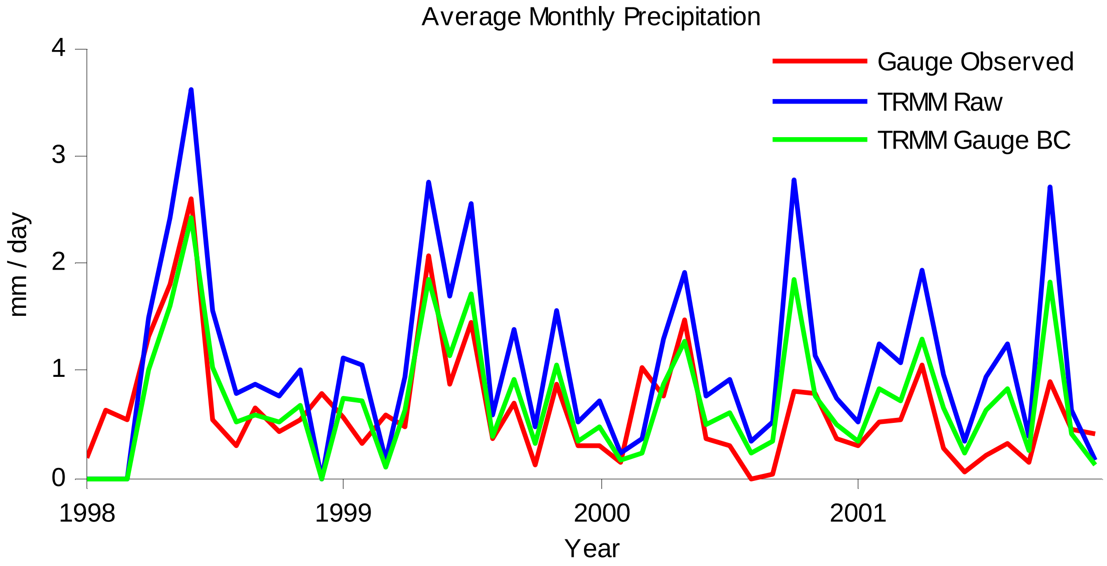

Figure 42: TRMM monthly averaged daily precipitation before and after gauge bias correction.

The reduction brought about by GPCC bias correction is little and the corrected average is largely overlapping the raw average. This is because GPCC is also overestimating the precipitation. The accuracy of GPCC rain gauge precipitation analysis depends on weather stations density in the grid cells. For example there should be 8 to 16 stations in a grid cell of 2.5° × 2.5°, depending on the variability of the precipitation in the region in order to estimate monthly area mean precipitation (Becker 2013). Unfortunately Talas catchment lacks a good density of rain gauges which is the main reason for erroneous precipitation estimates.

The monthly average precipitation obtained after gauge bias correction is better as shown in Figure 42. The comparison is made for one pixel only where the gauging station is located.

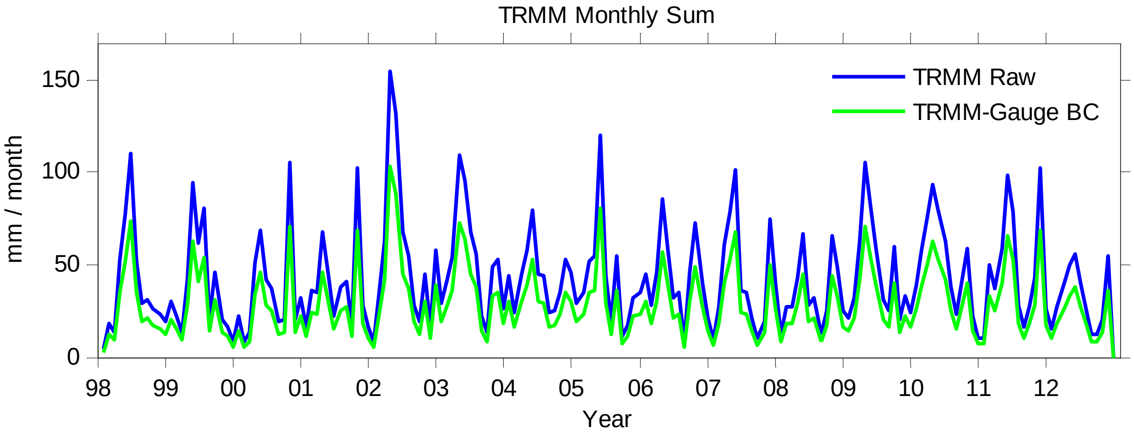

Figure 43: TRMM accumulated monthly precipitation before and after gauge bias BC.

Table 6 shows results for TRMM accumulated monthly precipitation with gauge and GPCC bias correction. The observed monthly sum is 19.4 mm but the TRMM and GPCC monthly sum is 42.6 and 40.3 mm which is two times the observed precipitation. As explained in the last paragraph GPCC also overestimated and the monthly sum after its correction just decreased by 3 mm of precipitation. The precipitation is still higher after gauge correction but it is definitely preferable to GPCC correction.

Table 6: Accumulated monthly precipitation before and after bias correction. Observed precipitation bias correction was carried out using four years data. GPCC correction was done with 15 years of data and the reduction achieved is shown in 3rd and 4th columns.

	Observed (1998 – 2001) mm / month	**GPCC (1998 – 2012) mm / month**	**TRMM Gauge BC[18] (1998 – 2012) mm / month**	**TRMM GPCC BC (1998 – 2012) mm / month**
Raw value	19.4147	40.3	42.614	42.614
Bias corrected	_	_	28.509	39.05

3.5.4. Spatial Distribution of Precipitation

The spatial distribution of TRMM-Gauge bias corrected precipitation is shown in Figure 44. In general, the precipitation gradient increases from north-west to east and south in the study area. The gradient is small during winter from November to February. The difference in precipitation over mountains and valley gradually increases from March to May and then decreases again till September. The precipitation is high in the eastern and southern regions of the study area which mainly constitute the mountainous part of the catchment. While it is low in the center and north-west part which contain the flood plain and Talas valley. The precipitation is the maximum in the month of May with high concentration in the east and south-east part. The gradient is also highest in this time of year. The second high precipitation event takes place in October but the gradient is not as high as in May. The mean daily precipitation in each month can also be seen in bar graph already presented in Figure 40. In essence it can be concluded that the precipitation is greater in high altitude regions of the study area.

---

[18] Bias Corrected

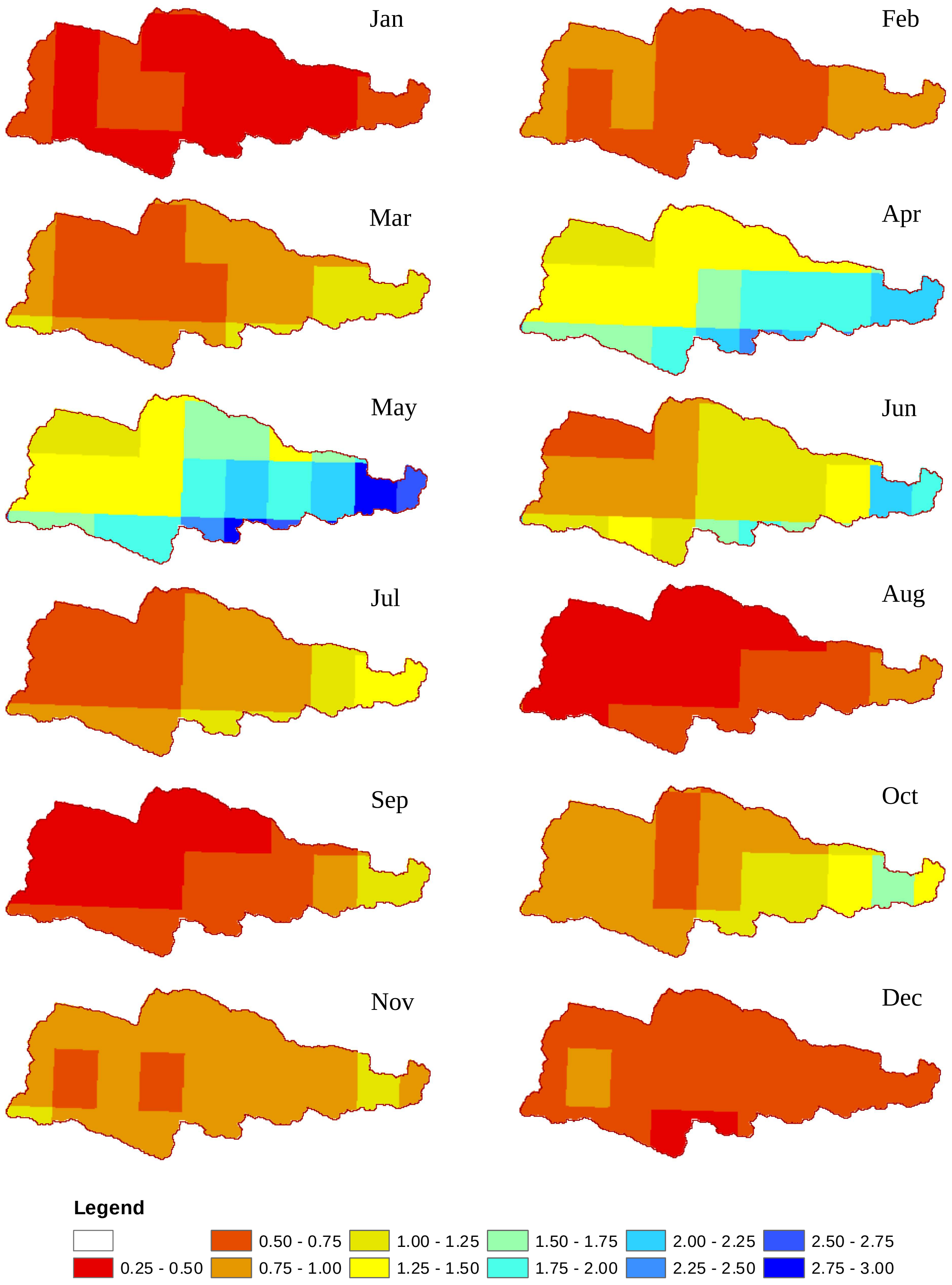

Figure 44: Spatial distribution of precipitation in Talas River Basin. The maps represent average daily precipitation in each month for 15 years. Average is calculated using TRMM-Gauge bias corrected data from 1998 to 2012.

Chapter 4

4. TOPKAPI Modeled Runoff

4.1. TRMM simulated runoff

The modeled runoff after correcting TRMM data with GPCC data and gauge observed precipitation is shown here from Figure 45 to Figure 52 together with observed runoff at the gauging stations. The simulated results are better for GPCC bias corrected precipitation for mountainous stations and the runoff difference in peak season is small. The discharge is less than observed for mountainous stations with gauge bias corrected precipitation. This is opposite when the results for flood plain gauging stations are analyzed and the runoff generated with gauge corrected precipitation is better. The benefit of using observed precipitation for bias correction is prominent here as the flow is much higher with GPCC corrected precipitation.

The annual volumetric difference is high and negative (underestimation of runoff) for station corrected precipitation in the mountainous region as compared to GPCC corrected precipitation. While the difference is less and positive (overestimation of runoff) in flood plain region where the runoff generated from GPCC bias corrected precipitation is much higher. Since all of the water either coming from snow melt or rainfall eventually reaches the flood plain and Kirov reservoir, the total water balance can be better analyzed by comparing results at Kirov. The volumetric difference is 1.073 km^3 per year (123 % overestimated) from GPCC corrected precipitation while it is 0.219 km^3 per year (25 % overestimated) from gauge corrected precipitation. It means that the total precipitation in the study area is higher from GPCC corrected data which results in higher runoff at catchment outlet.

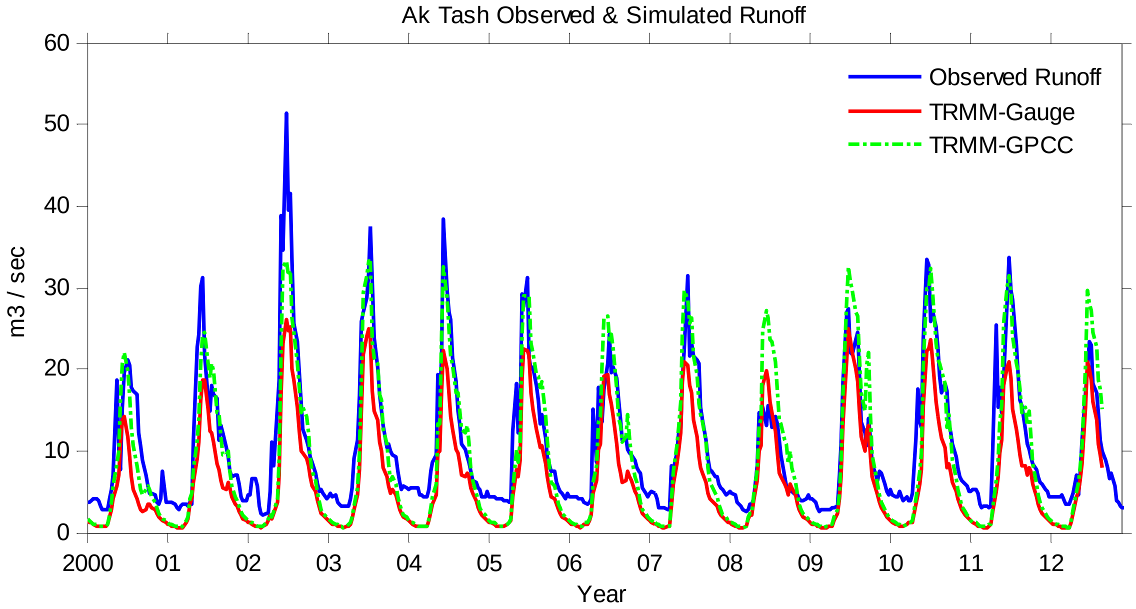

Figure 45: Observed and simulated runoffs at Ak Tash gauging station. The observed, TRMM-GPCC and TRMM-Gauge BC runoffs are shown by continuous blue, dashed green and continuous red lines respectively. The time series is from 2000 to 2012 plotted as ten days averages.

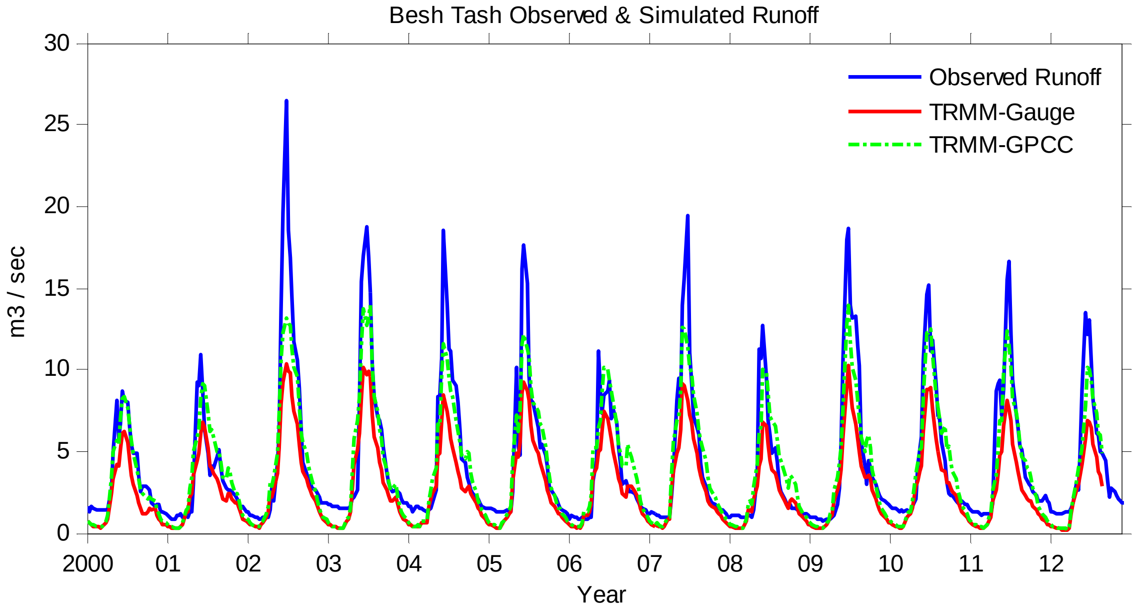

Figure 46: Observed and simulated runoffs at Besh Tash gauging station. The observed, TRMM-GPCC and TRMM-Gauge BC runoffs are shown by continuous blue, dashed green and continuous red lines respectively. The time series is from 2000 to 2012 plotted as ten days averages.

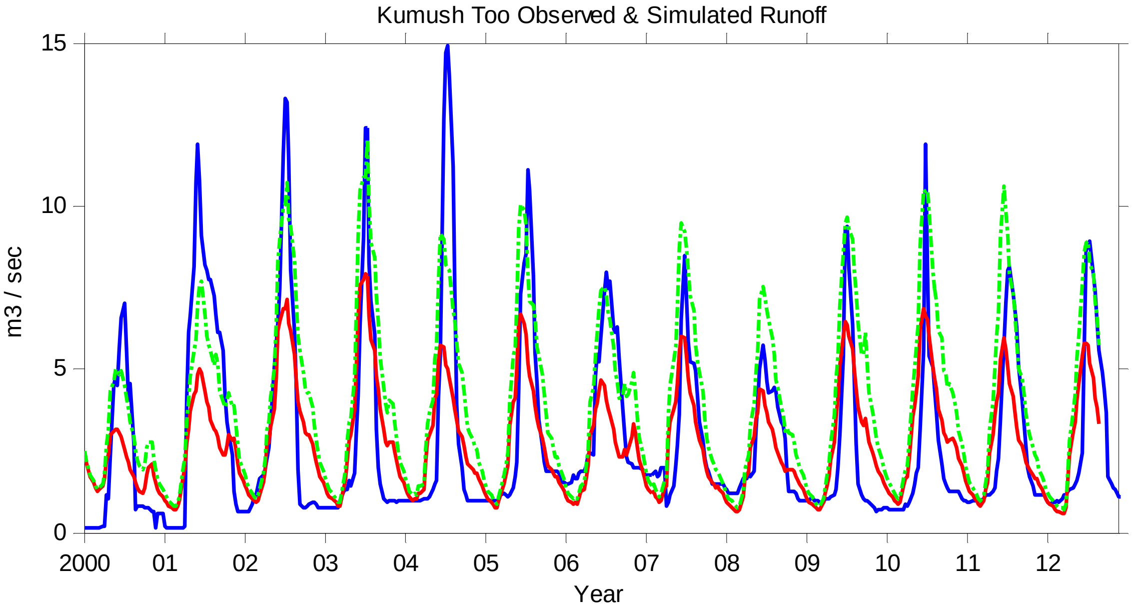

Figure 47: Observed and simulated runoffs at Kumush Too gauging station. The observed, TRMM-GPCC and TRMM-Gauge BC runoffs are shown by continuous blue, dashed green and continuous red lines respectively. The time series is from 2000 to 2012 plotted as ten days averages.

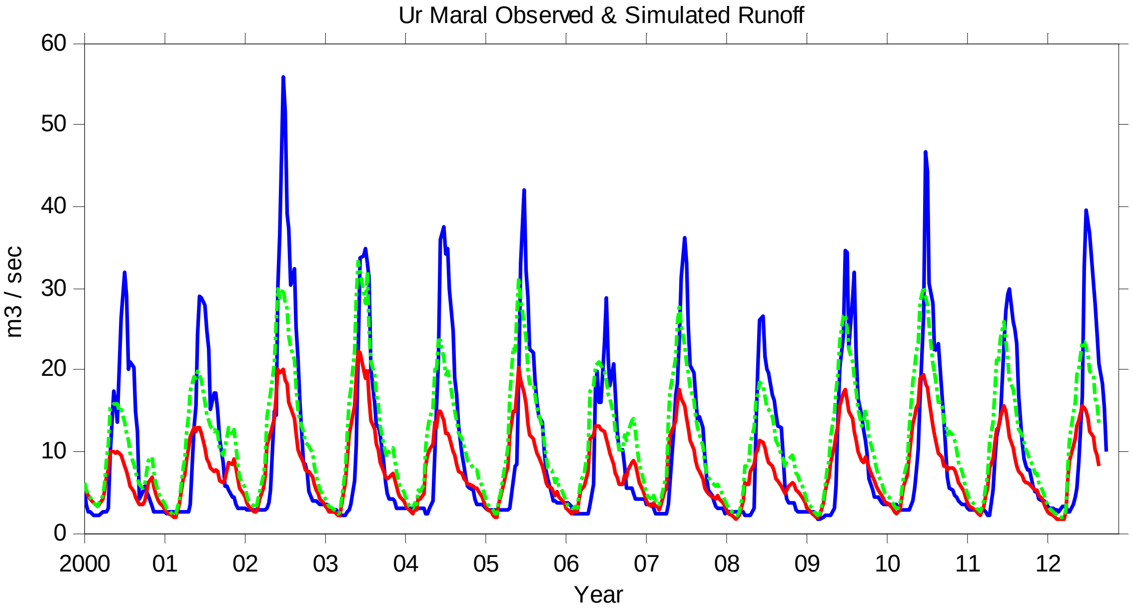

Figure 48: Observed and simulated runoffs at Ur Maral gauging station. The observed, TRMM-GPCC and TRMM-Gauge BC runoffs are shown by continuous blue, dashed green and continuous red lines respectively. The time series is from 2000 to 2012 plotted as ten days averages.

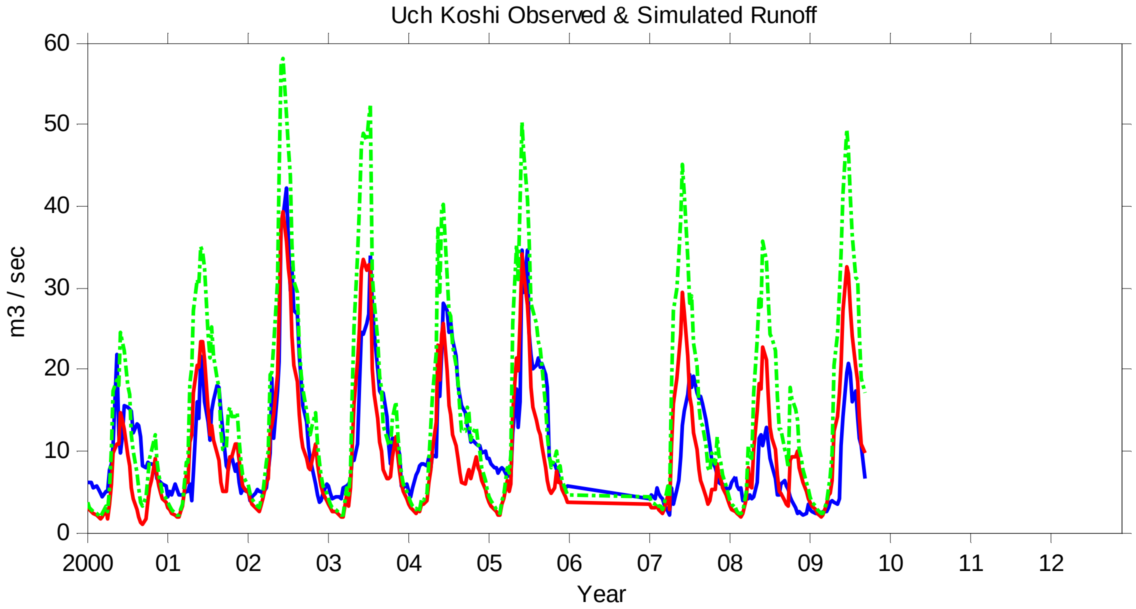

Figure 49: Observed and simulated runoffs at Uch Kochoy gauging station. The observed, TRMM-GPCC and TRMM-Gauge BC runoffs are shown by continuous blue, dashed green and continuous red lines respectively. The time series is from 2000 to 2012 plotted as ten days averages. Uch Kochoy observed runoff is missing for the year 2006.

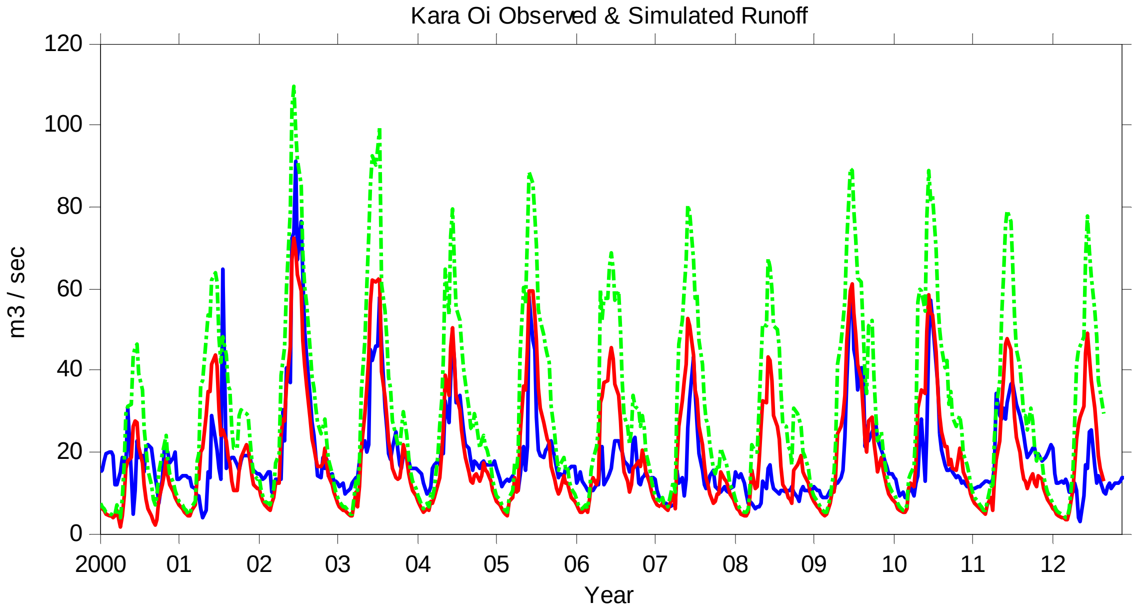

Figure 50: Observed and simulated runoffs at Kara Oi gauging station. The observed, TRMM-GPCC and TRMM-Gauge BC runoffs are shown by continuous blue, dashed green and continuous red lines respectively. The time series is from 2000 to 2012 plotted as ten days averages.

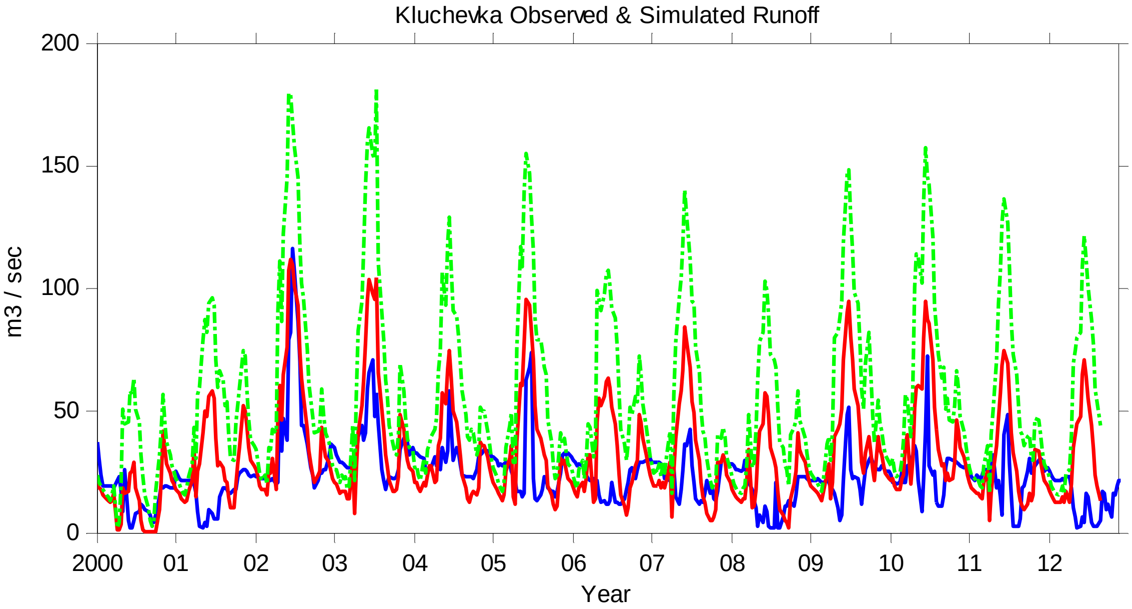

Figure 51: Observed and simulated runoffs at Kluchevka gauging station. The observed, TRMM-GPCC and TRMM-Gauge BC runoffs are shown by continuous blue, dashed green and continuous red lines respectively. The time series is from 2000 to 2012 plotted as ten days averages.

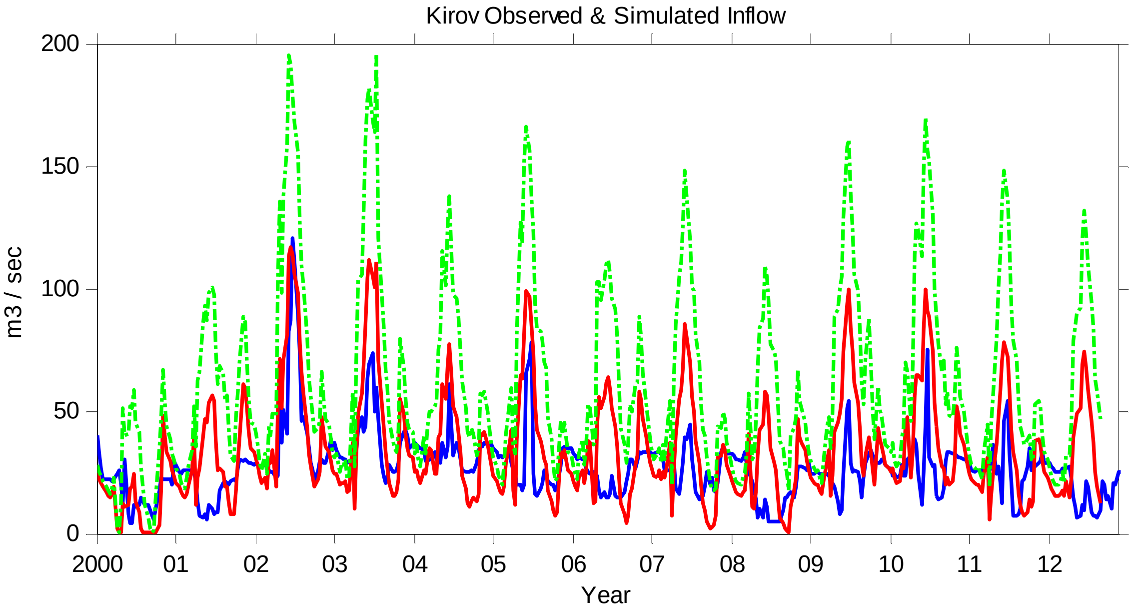

Figure 52: Observed and simulated runoffs at Kirov Reservoir gauging station. The observed, TRMM-GPCC and TRMM-Gauge BC runoffs are shown by continuous blue, dashed green and continuous red lines respectively. The time series is from 2000 to 2012 plotted as ten days averages.

The model is underestimating runoff at Ak Tash and Besh Tash stations which is because of inadequate soil information from FAO map. 64 % of study area is characterized as clay loam. A small change in properties of this soil region has relatively small effect on flow of mountainous stations but the impact is large on flood plain gauging stations. If the properties like soil depth, residual soil water content are reduced, the water holding capacity of the soil reduces which results in higher flow in the channel. Hence the runoff at Ak Tash and Besh Tash improves but on the other hand this causes large increase in runoff at the downstream stations especially Kluchevka and Kirov reservoir. The volumetric difference increases by large amount at Kirov reservoir. Therefore a compromise had to be made between runoff at upstream stations Ak Tash, Besh Tash and floodplain Kluchevka and Kirov Reservoir stations.

The Ur Maral and Kumush Too gauging stations have different runoff characteristics. Although they are present in a separate region which is composed of sandy loam soil type but soil has proven not to be the only important factor in modeling the runoff of these stations. The problem is that the simulated runoff peak occurs one month earlier than the observed runoff peak. To control this, the hydraulic conductivity of soil was reduced and soil depth was increased which delayed the simulated runoff peak in the summer. But this decreased the total water flowing through the stations and increased the volumetric difference. The factors other than soil properties that can be important in delaying the simulated runoff for Ur Maral and Kumush Too can be roughness of the terrain and flow partition coefficient. The Manning's roughness coefficient and flow partition coefficient depend on Strahler order of the stream in TOPKAPI. They are constant for one stream type and change with varying stream order.

A brief summary of runoff results on annual scale is shown in Table 7. If a box model is considered where precipitation is input, evapotranspiration and water abstraction for irrigation are losses and Kirov reservoir is taken as the outlet point of the catchment (in truth the outlet point is few pixels downstream Kirov gauge) where the total discharge is measured, the precipitation corrected with observed data give better results.

Table 7: Correlation coefficient, coefficient of determination and volumetric difference between observed and simulated runoff. The results are averaged for 13 year period (2000 to 2012). The table shows comparison between results of model run from TRMM-Gauge and TRMM-GPCC bias corrected precipitation datasets.

Station Name	Correlation Coefficient (R)		Coefficient of Determination (r^2)		Volumetric Difference (km^3 / year)	
	Gauge	*GPCC*	*Gauge*	*GPCC*	*Gauge*	*GPCC*
Talas Ak Tash	0.92	0.91	0.91	0.80	- 0.132	- 0.043
Besh Tash	0.94	0.93	0.96	0.91	- 0.049	- 0.012
Kumush Too	0.76	0.80	0.87	0.70	- 0.006	0.034
Ur Maral	0.76	0.80	0.92	0.82	- 0.084	0.033
Uch Kochoy	0.77	0.79	0.52	- 0.11	- 0.016	0.130
Kara Oi	0.75	0.72	0.33	- 0.91	0.019	0.375
Kluchevka	0.51	0.39	-0.85	- 5.17	0.254	0.997
Kirov Reservoir	0.55	0.41	-0.95	- 5.82	0.219	1.073

4.1.1. Snow Cover Efficiency

The accuracy of simulated snow cover was calculated by comparing it with MODIS snow cover images on a pixel to pixel basis. **The mean snow cover efficiency is equal to 80 %.** The snow melt starts from Talas valley and cropland area in North-West of the basin. With the rise of temperature in summer, the snow in the nearby mountains starts melting gradually in south and east direction. The southern part shows relatively quick snow melt as compared to eastern part. This is because of higher mountains in the eastern side which have a higher temperature gradient. By the end of May more than 90 % of area becomes snow free as shown in MODIS images. The eastern part receives higher precipitation and the snow accumulation starts earlier there as compared to mountains in the south and north direction. Hence this area shows late snow melt and early snow accumulation. The snow melt occurs few weeks late in the model and the snow does not melt as quickly as observed in the MODIS data. This is a drawback in the present study as more time was required to calibrate the model. A comparison of snow cover area on the first day of each month is shown in the next three figures. The comparison is shown for the year 2003.

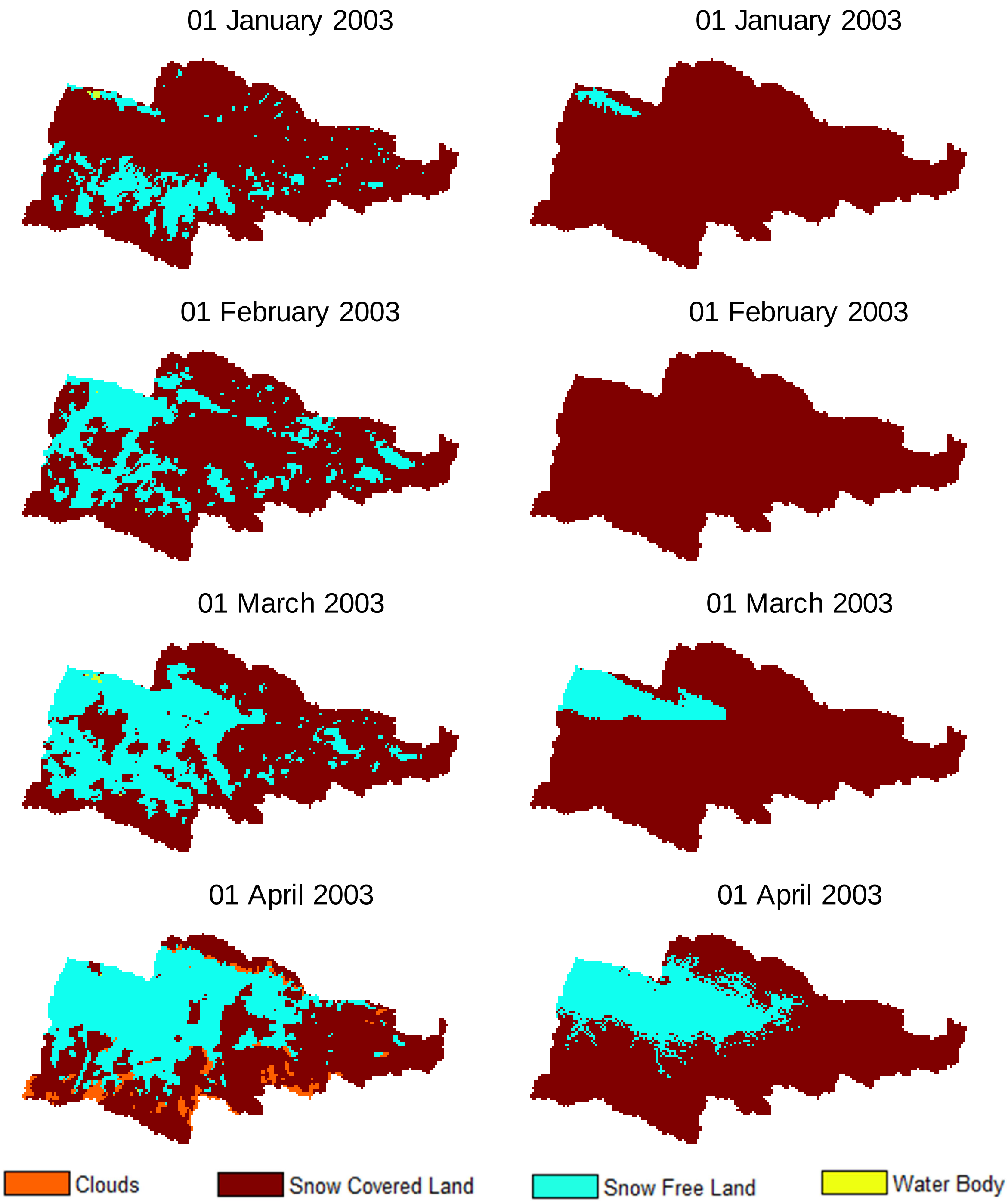
01 January 2003

01 January 2003

01 February 2003

01 February 2003

01 March 2003

01 March 2003

01 April 2003

01 April 2003

Figure 53: Comparison between MODIS observed Snow Cover after temporal combination (left column) and modeled snow cover by TOPKAPI (right column) from January to April, 2003.

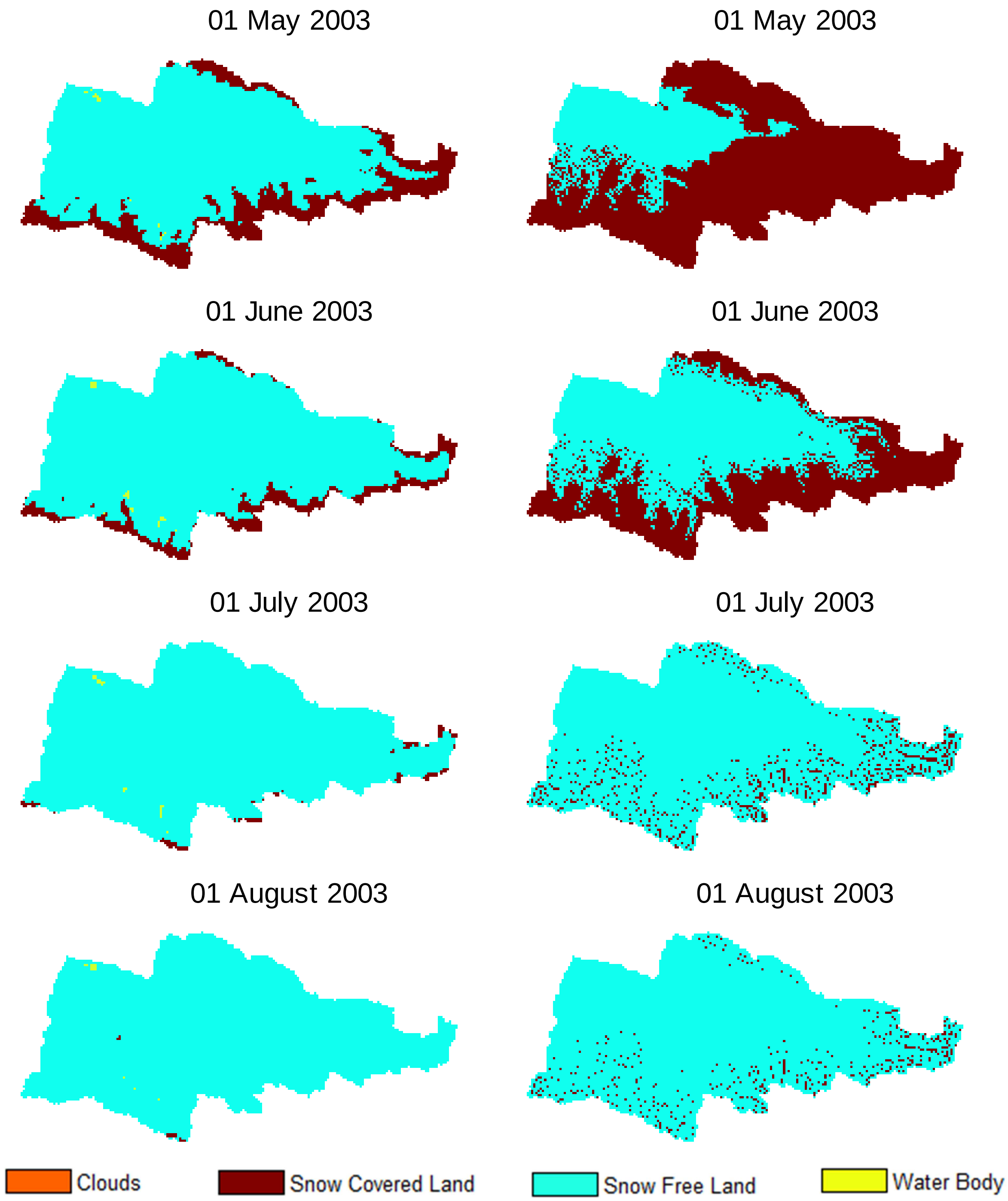

Figure 54: Comparison between MODIS observed Snow Cover after temporal combination (left column) and modeled snow cover by TOPKAPI (right column) from May to August, 2003.

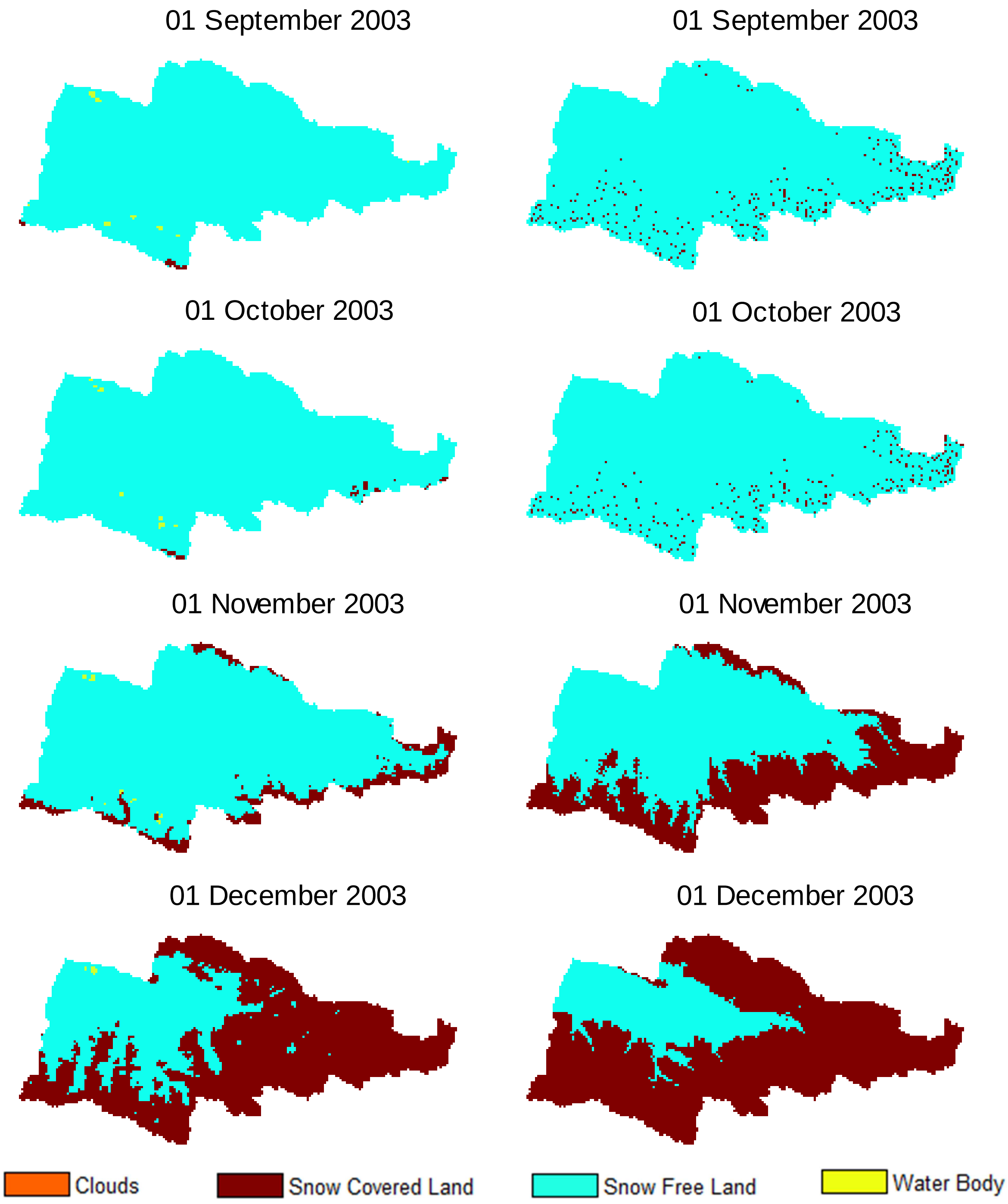

Figure 55: Comparison between MODIS observed Snow Cover after temporal combination (left column) and modeled snow cover by TOPKAPI (right column) from September to December, 2003.

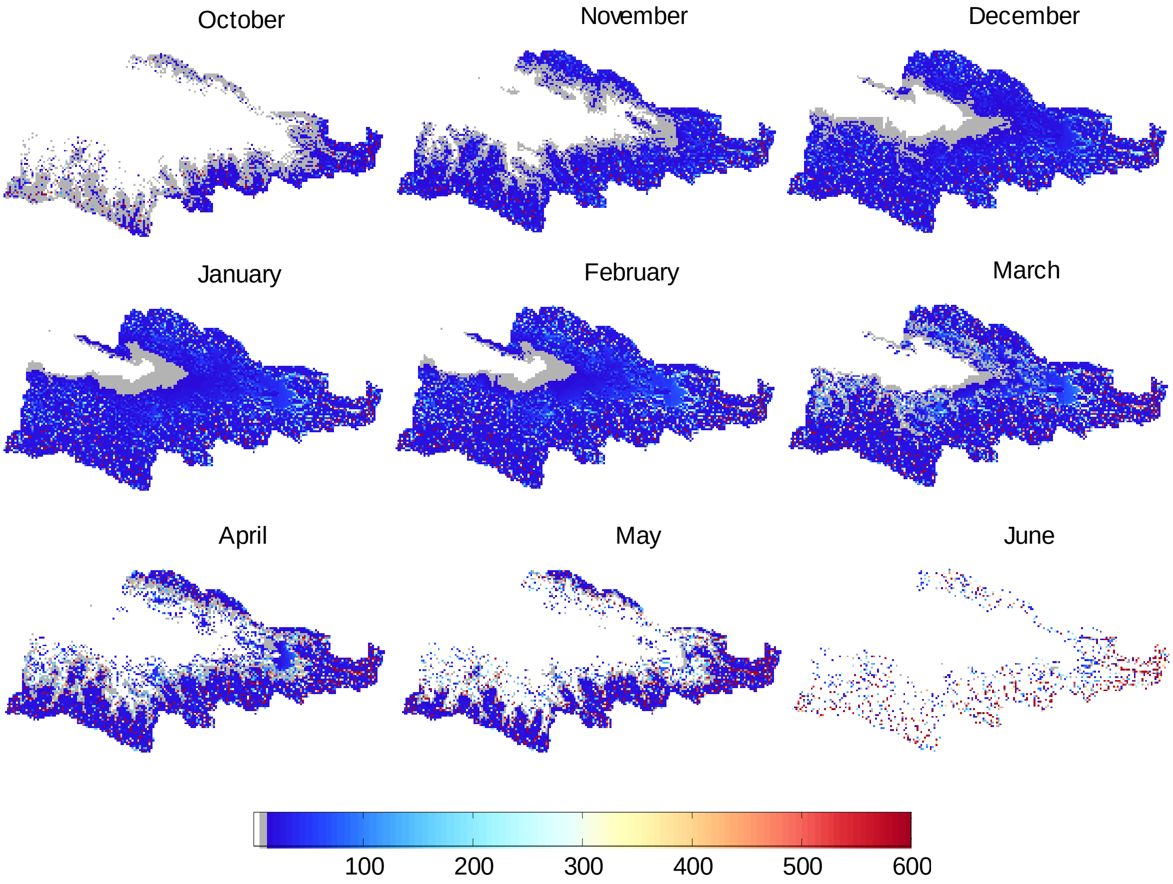

Figure 56: Monthly average of snow water equivalent from 2000 to 2012. The maps show snow height measured in mm of water equivalent and its monthly cycle averaged for a period of 13 years.

The monthly average of simulated snow water equivalent is shown in Figure 56. The snowfall starts in the month of October with higher intensity over the eastern mountains. The whole basin is then gradually covered by snow which reaches its maximum extent in February. The snow height is small in the valley represented by the white and the grey colors. The snow height starts decreasing from March and roughly 90 % of the area becomes snow free in June.

4.1.2. Low runoff years

The observed runoff is quite low in 2000, 2001, 2006, 2008 and 2012 which is not correctly predicted by the model. The simulated runoff is lower than in other years but still higher than observed discharge in the low runoff years. The possible reasons for low observed discharge can be (1) Low precipitation, (2) High temperature or (3) Increase in water abstraction for irrigation.

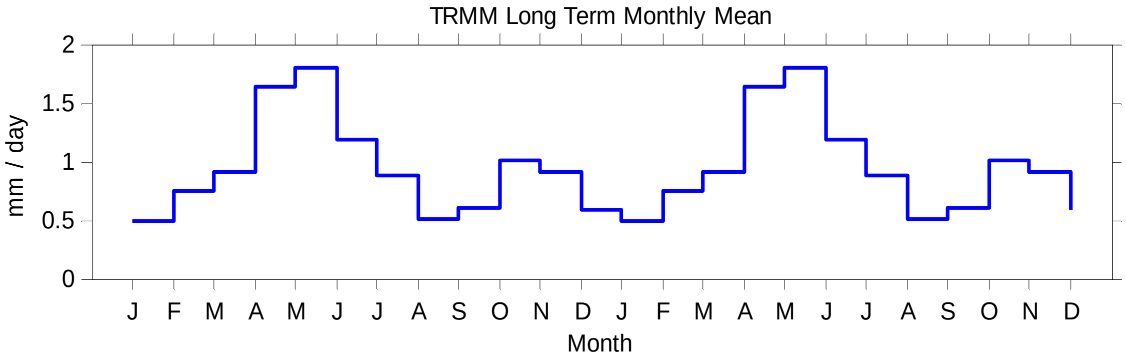

Figure 57: Two annual cycles of TRMM long term monthly mean calculated for a period of 15 years from 1998 to 2012. The TRMM-Gauge bias corrected data is used in this calculation and the plot is made by taking monthly averages of daily precipitation in mm.

The two annual cycles of TRMM long term monthly mean are presented in Figure 57. The plot shows that the study area receives higher summer precipitation in April and May and higher early winter precipitation in October and November. The first graph in Figure 58 shows TRMM running monthly mean. The precipitation was low in 2000, 2001, 2004, 2006, 2008 and 2012. The long term monthly mean was subtracted from running monthly mean of each

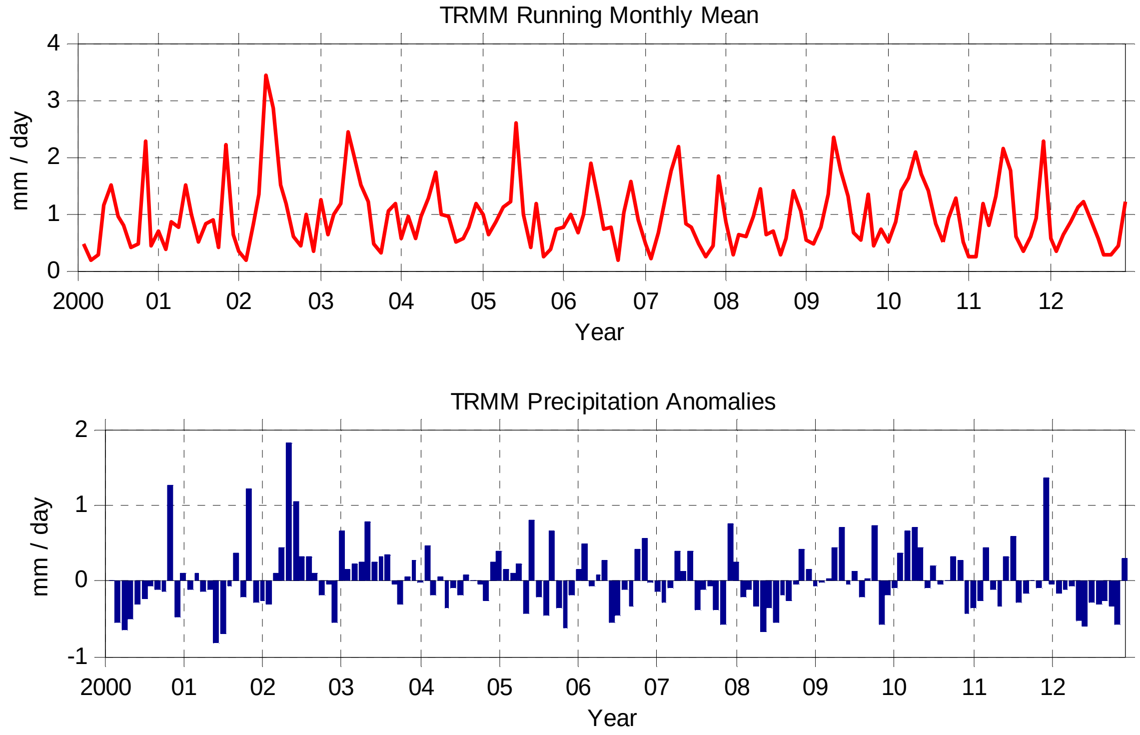

Figure 58: TRMM running monthly mean and TRMM monthly anomalies from 2000 to 2012. The TRMM-Gauge bias corrected data is used in this calculation and the plot is made by taking monthly averages of daily precipitation in mm.

year to produce the monthly anomalies plot shown in the second graph in Figure 58. The anomalies graph also reveals lower than average precipitation in these years. The precipitation is particularly below average in the summer months while it is positive in the month of October in most of the years. The precipitation was below average for most of the months in 2000 and 2001. The winter of 2005 and summer of 2006 also received less precipitation. The lower than average snowfall in 2005 led to small runoff generated from snow melt in the succeeding summer period of 2006. In addition the summer precipitation was also low in 2006. The two events of less precipitation resulted in overall low river discharge in the year 2006. A similar event took place in winter 2007 and summer 2008. This caused another year with low river runoff. The precipitation was below average all year long in 2012 except for the month of December. This figure provides one reason for extremely low observed runoff in the above mentioned years. These years were characterized by low precipitation, particularly the summer rainfall.

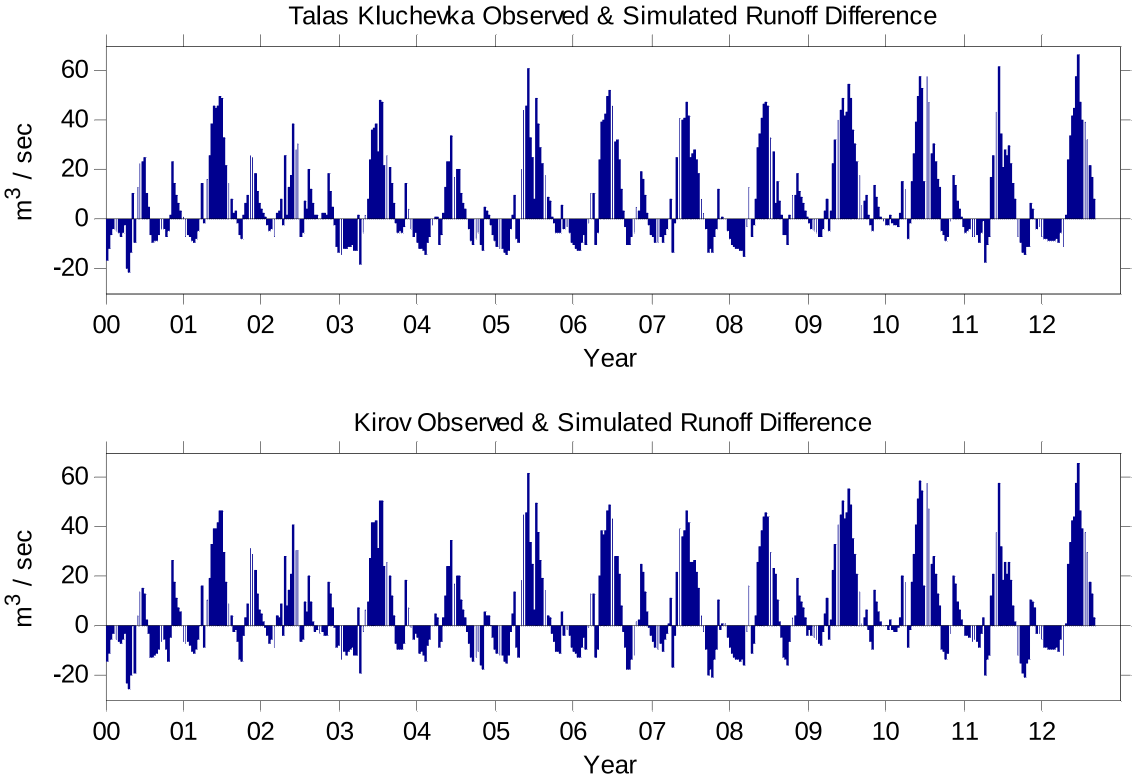

Figure 59: Difference in observed and simulated runoff at Kluchevka and Kirov reservoir gauging stations. The graphs are made after subtracting average decadal observed runoff from TOPKAPI simulated runoff.

The reason for higher simulated runoff is overestimation of precipitation by the TRMM product. The anomalies plot shows less precipitation in the low runoff years but it is still higher than the observed values. Although bias correction of TRMM data with Gauge readings helped to scale down the precipitation but it did not help in eradicating the overestimation error completely (Table 6). A detailed analysis of the precipitation anomalies for individual sub-catchments of the mountainous stations was also carried out (Figure 95, Appendix C). The results show a very similar pattern as that of the TRMM anomalies plot for Talas catchment (Figure 58) with little increase in positive and negative anomalies. This shows that the TRMM actually observed less precipitation in the low runoff years at mountainous regions of the study area but it was still higher than the actual precipitation there.

The difference in the observed and simulated runoffs at Kluchevka and Kirov gauging stations (Figure 59) shows that the simulated runoff is overestimated by more or less the same quantity throughout the time series (exception for the year 2001). This is due to higher input of water into the hydrological system in form of precipitation. The remotely sensed data overestimate precipitation by roughly the same amount every year.

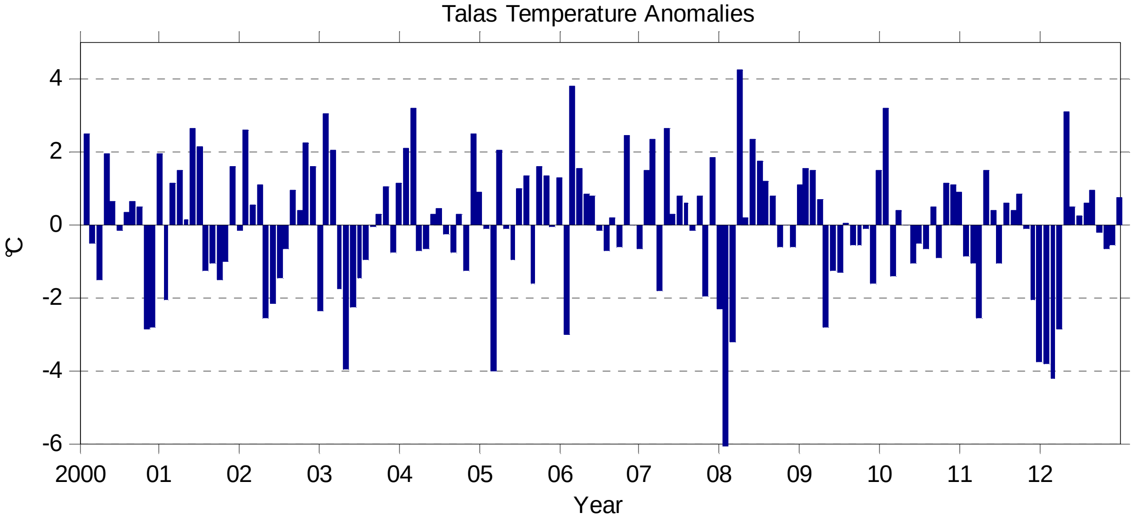

Figure 60: Temperature anomalies from 2000 to 2012. The graph shows anomalies in monthly average temperature in Talas Valley calculated by using 13 years of long term mean from 2000 to 2012.

Figure 60 shows that the temperature in Talas valley was above average in the summer months of 2001, 2005, 2006, 2007, 2008 and 2012. All of these do not correspond to the low runoff years but temperature is one of the reasons for drier summer periods in 2001, 2006, 2008 and 2012. The warmer season is especially visible in 2006 and 2008. The hotter climate combined with low precipitation resulted in decreased runoff in the river.

Higher water abstraction can be one of the important reasons for low observed runoff. Crops having higher water demand like rice and cotton are not regularly sown in Talas valley. But there is a big possibility of change in cropping pattern in these years. In order to analyze this, the difference in runoff observed at Kluchevka station and total runoff from stations located upstream of Kluchevka was calculated for 13 years. The long term difference (Figure 29) was subtracted from yearly difference to generate the anomalies plot (Figure 61). The graph shows that the water abstraction was high in the years 2000, 2001 and 2012. But the water abstraction was not high in all of the low runoff years. In addition the anomalies are positive and high in the years 2009, and 2011 also but the water flow in the river was not low in these years. This means that water abstraction for irrigation does not have a drastic effect in reducing discharge of the river.

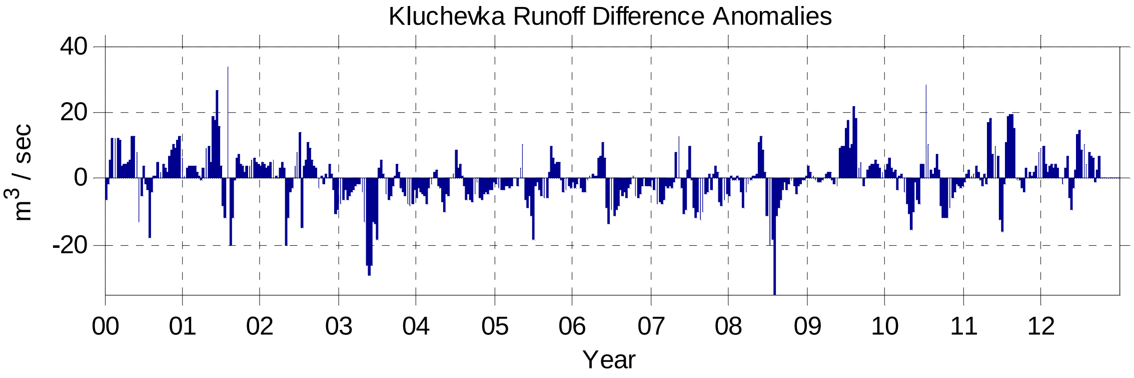

Figure 61: Talas Kluchevka runoff difference anomalies from 2000 to 2012. The plot is made after subtracting long term difference in runoff recorded at Kluchevka and total runoff from stations located upstream of it from yearly difference.

4.2. TOPKAPI Ecosystem Components

4.2.1. Precipitation

Figure 63 shows total precipitation received in the catchment and its partitioning into rain and snow according to temperature. The figure is for TRMM data bias corrected with gauge precipitation. The area receives relatively higher precipitation twice a year as can be seen in the second graph in the figure. The first high precipitation event occurs in May while the second one occurs in October. The precipitation is less during the other months. It is classified as rain or snow by adjusting the threshold air temperature for the precipitation state transition factor in the model. When the temperature is above this threshold, it rains, while it snows when the temperature is below or equal to the threshold temperature. Rainfall mostly occurs in the summer months between March and October when the temperature is high. Snowfall is dominant from November to February. This can be seen in the third and the fourth graphs in the figure and can be compared with temperature in the first graph. The snow peaks occur when the temperature lines are in depression representing cold winter climate and the rainfall approaches zero in these months. Precipitation as snowfall is zero during summer when the rainfall lines are at peak. The trend is more prominent in Figure 64 which shows results for TRMM dataset bias corrected with GPCC precipitation. The first difference between the two figures is higher total precipitation in GPCC bias corrected data. The snow and rain peaks in winter can be better seen in the latter figure which explains the change of precipitation state with temperature.

The spatial distribution of precipitation as rainfall and snowfall is also shown in Figure 62. The precipitation is dominantly rainfall in the lower elevation regions where the temperature is low. And it precipitates as snowfall at higher altitudes because of decrease in temperature due to adiabatic lapse rate and elevation.

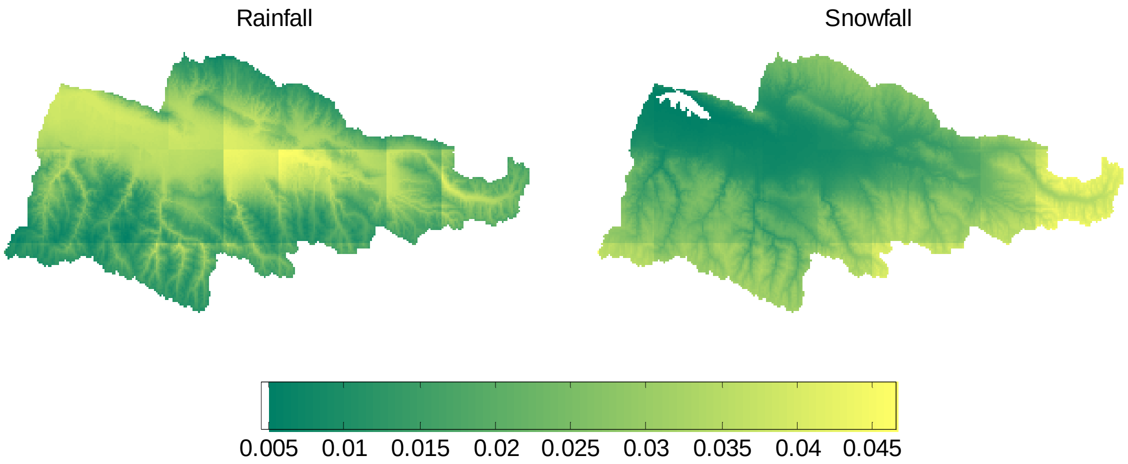

Figure 62: Distribution of precipitation into rainfall and snowfall depending upon temperature and elevation in the study area. The graphs show average hourly precipitation in mm from 2000 to 2012.

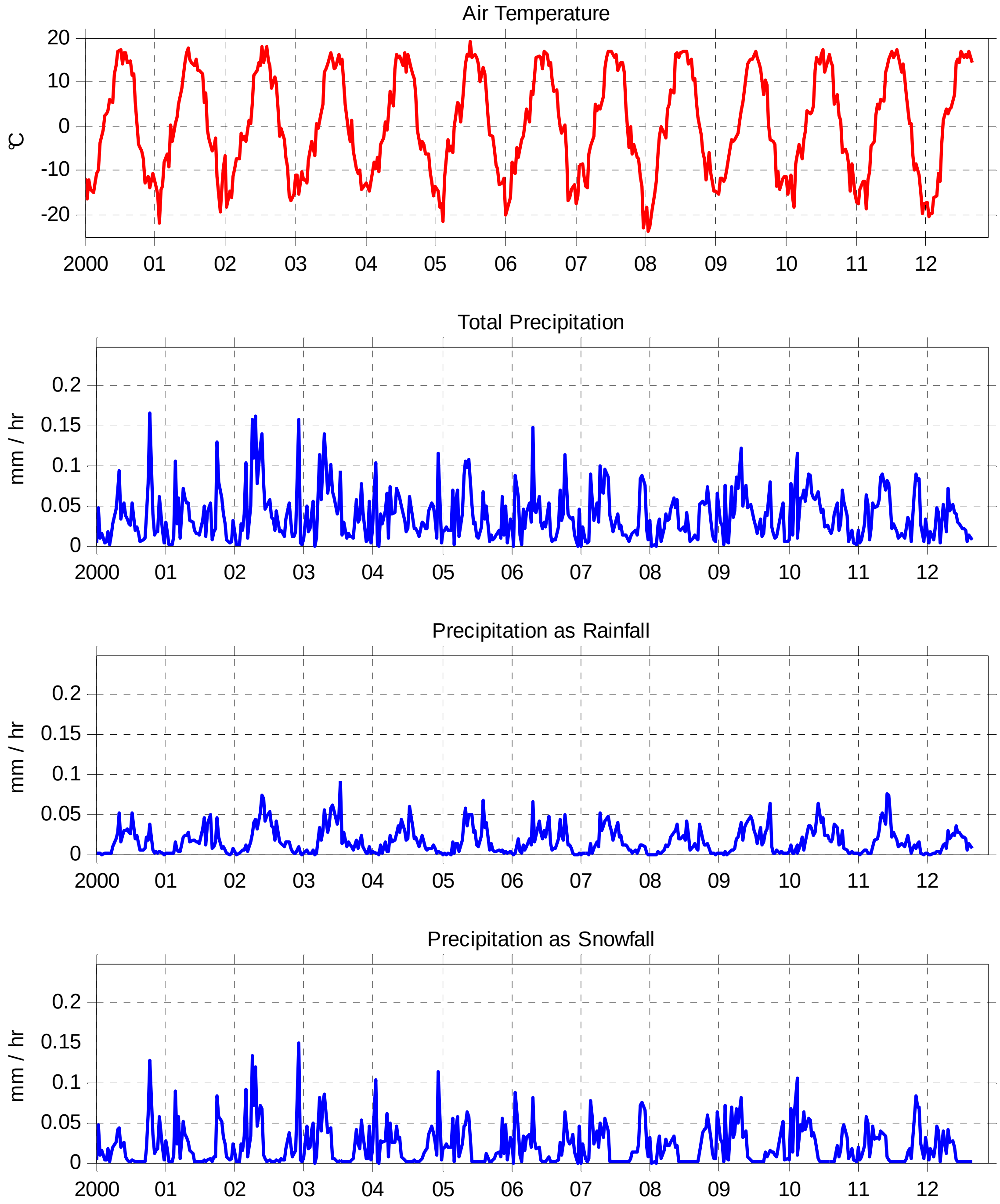

Figure 63: Total precipitation and its distribution into rain and snow depending on temperature. The time series is from 2000 to 2012 for TRMM-Gauge BC precipitation. The plotted values are ten days averages.

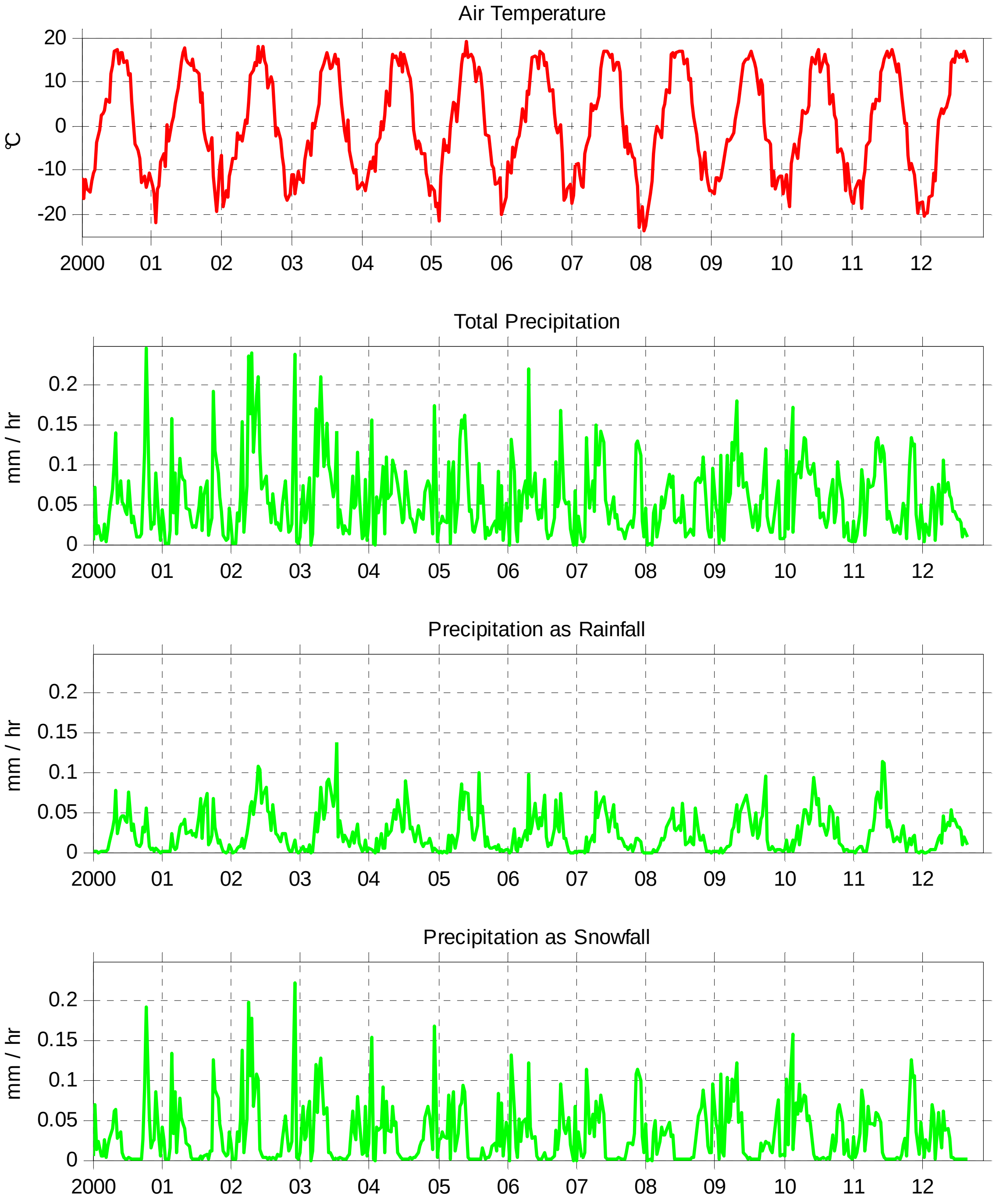

Figure 64: Total precipitation and its partitioning into rain and snow according to temperature. The time series is from 2000 to 2012 for TRMM-GPCC BC precipitation. The plotted values are ten days averages.

4.2.2. Snow melt

The seasonal change in snow melt timing is presented in Figure 65. Separate plots are made for Gauge and GPCC BC precipitations in the blue and green lines respectively. The snow melt is highest in hot summer months of May, June and July when the temperature is at its peak. The peak slowly declines till the end of each year and the snow melt is very low from November to January. The enhanced temperature index model used to calculate snow melt is a function of temperature, global irradiance, albedo and two empirical factors namely shortwave radiation factor and temperature factor. In addition the snow melt is also dependent on three factors (1) Threshold temperature for snow melt (2) Melt onset temperature (3) Number of days that should exceed the limit of melt onset temperature in order for melt to occur finally depending on threshold temperature. Since the temperature can often go above zero in the valley and mountainous regions in May and October and sufficient energy is also available from sunlight, the freshly fallen snow in these two months finds its way to the river soon. This is evident from the two peaks which occur before and after the highest peak of snow melt in the summer. The big peak occurring before the highest peak is in May and the little peak occurring after is in October. Hence a part of the precipitation which falls in the form of snow as shown in Figure 63 and Figure 64 melts earlier.

One interesting fact shown in this figure is the graph for number of grid cells covered with snow in the catchment. It is almost the same for the two datasets throughout the time series as the two lines are overlapping. The reason for this is that although the total precipitation in GPCC corrected data is higher as compared to Gauge corrected data, this high precipitation falls as snow on the same number of grid cells. It depends on temperature of the grid cells which does not change in the two model runs. This results in larger snow water equivalent content in GPCC corrected data but the number of cells covered with snow remains the same in both model runs.

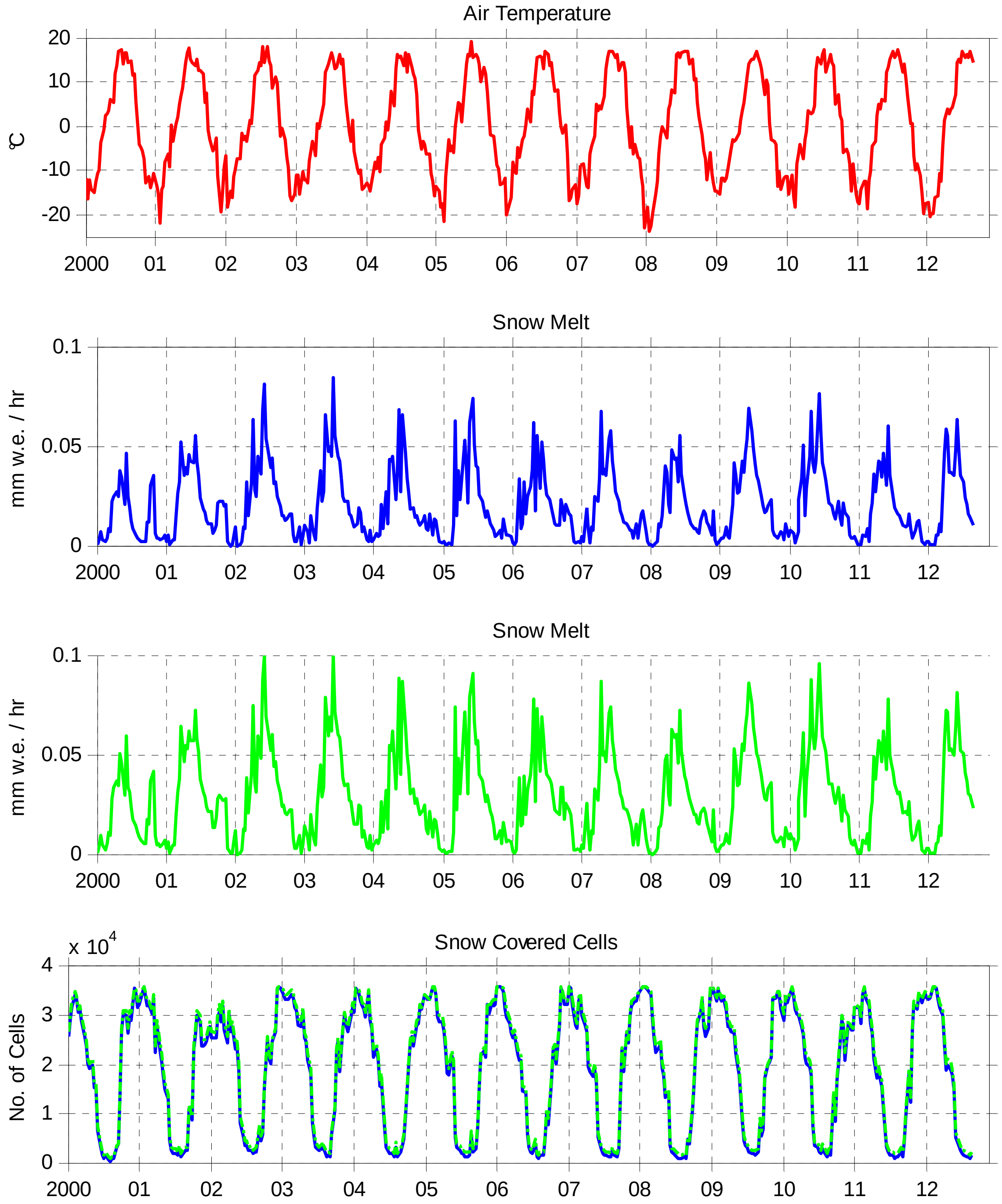

Figure 65: Snow melt in mm of water equivalent per hour and number of cells covered by snow in the catchment. The time series is from 2000 to 2012 plotted as ten days averages. The blue and green lines represent model runs from TRMM-Gauge and TRMM-GPCC bias corrected precipitation datasets.

4.2.3. Evapotranspiration

The environmental demand of evapotranspiration and actual evapotranspiration (AET) taking place in the study area is shown in Figure 66. The evapotranspiration rises in the summer with rise in temperature and global irradiance (Figure 24) and becomes zero in the winter when global irradiance is least, temperature is below freezing point and the study area is largely covered with snow. A crop factor correction is also included in the model to account for increase in potential evapotranspiration (PET) in the irrigated area. This result in slight increase in PET in the third plot compared to PET estimated without considering the crop effect in the second plot. As the temperature, cloud transmissivity and global irradiance do not change, PET is similar to the two precipitation datasets.

The AET is approximately three times less than PET indicating deficiency of water available to balance this difference. The AET from TRMM-GPCC corrected data (dashed green line) is larger than the other data because it has higher mean precipitation and supplies more water to the area that eventually results in higher AET. It is important to note here that AET is less in the years 2000, 2001, 2004, 2006, 2008 and 2012 which correspond to low runoff years also. This is because the climate was drier than usual and less water was available in form of precipitation and hence for evapotranspiration at that time.

The AET is significantly higher in the cropland area. The mountains in the catchment are mostly dry with no vegetation cover and hence the AET is lower at high altitudes. The river and streams also contribute to water losses through evaporation as shown in Figure 67. There is a considerable increase in AET with irrigation of agricultural districts.

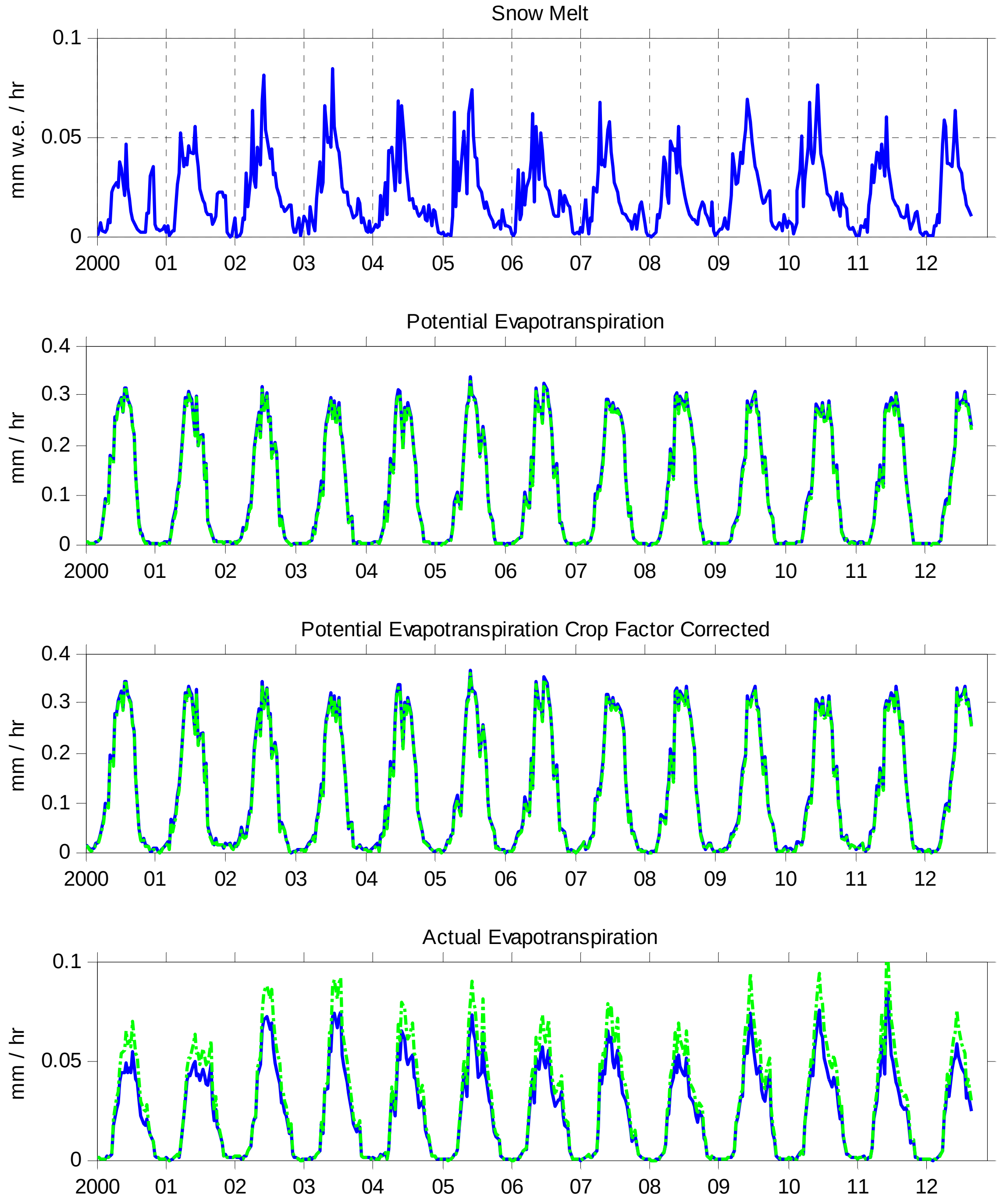

Figure 66: Seasonal variation of potential evapotranspiration, potential evapotranspiration after crop factor correction and actual evapotranspiration. Blue lines represent results of TRMM bias correction from gauge observed precipitation and broken green lines represent results from GPCC bias corrected precipitation. The values are 10 days average from year 2000 to 2012.

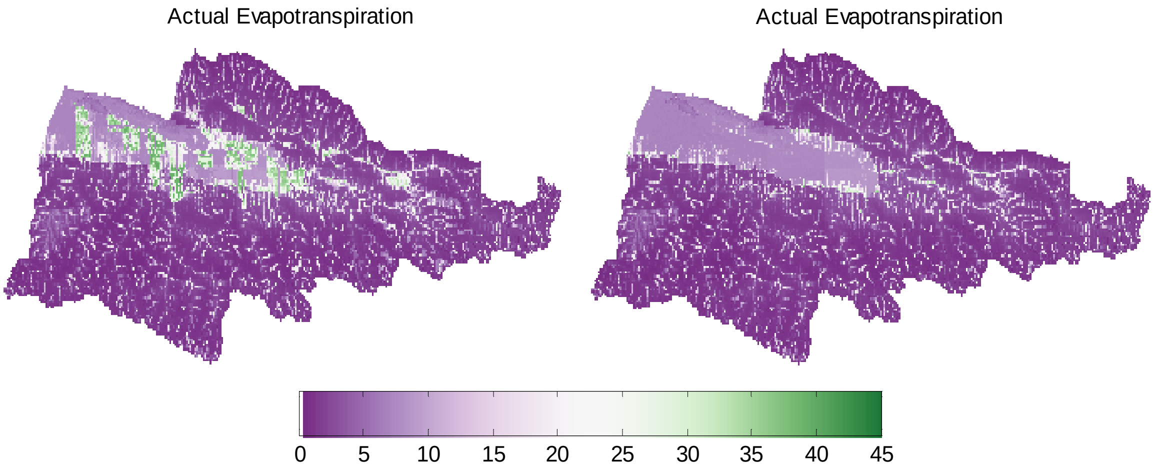

Figure 67: Spatial distribution of actual evapotranspiration in the study area. The left and the right maps are made from model runs with and without irrigation. The graphs show average daily AET in m^3 from 2000 to 2012.

4.2.4. Exfiltration

Figure 68 depicts the contribution of soil and groundwater storage to the surface and channel flow through exfiltration. The figure includes graphs for exfiltration from the top soil layer, bottom soil layer and groundwater. Exfiltration is higher in the summer when plenty of water is available through rainfall and snow melt. It is absorbed by the soil and transported to the bottom soil layer and groundwater component through hydraulic conductivity. Part of this water exfiltrates and feeds the soil layer above or the water channel. The exfiltration is less in the first soil layer as compared to the second soil layer and it is highest in case of groundwater. This is related to the soil depth and its storage capacity. The first soil layer has little depth and can store less water. The second soil layer has a larger depth than the top layer and groundwater storage is the largest. Hence the exfiltration is higher as we move from the surface to the groundwater component because of greater capacity to store and transport water. The exfiltration is higher from GPCC BC precipitation in all components as shown by green lines because of higher mean precipitation and water availability.

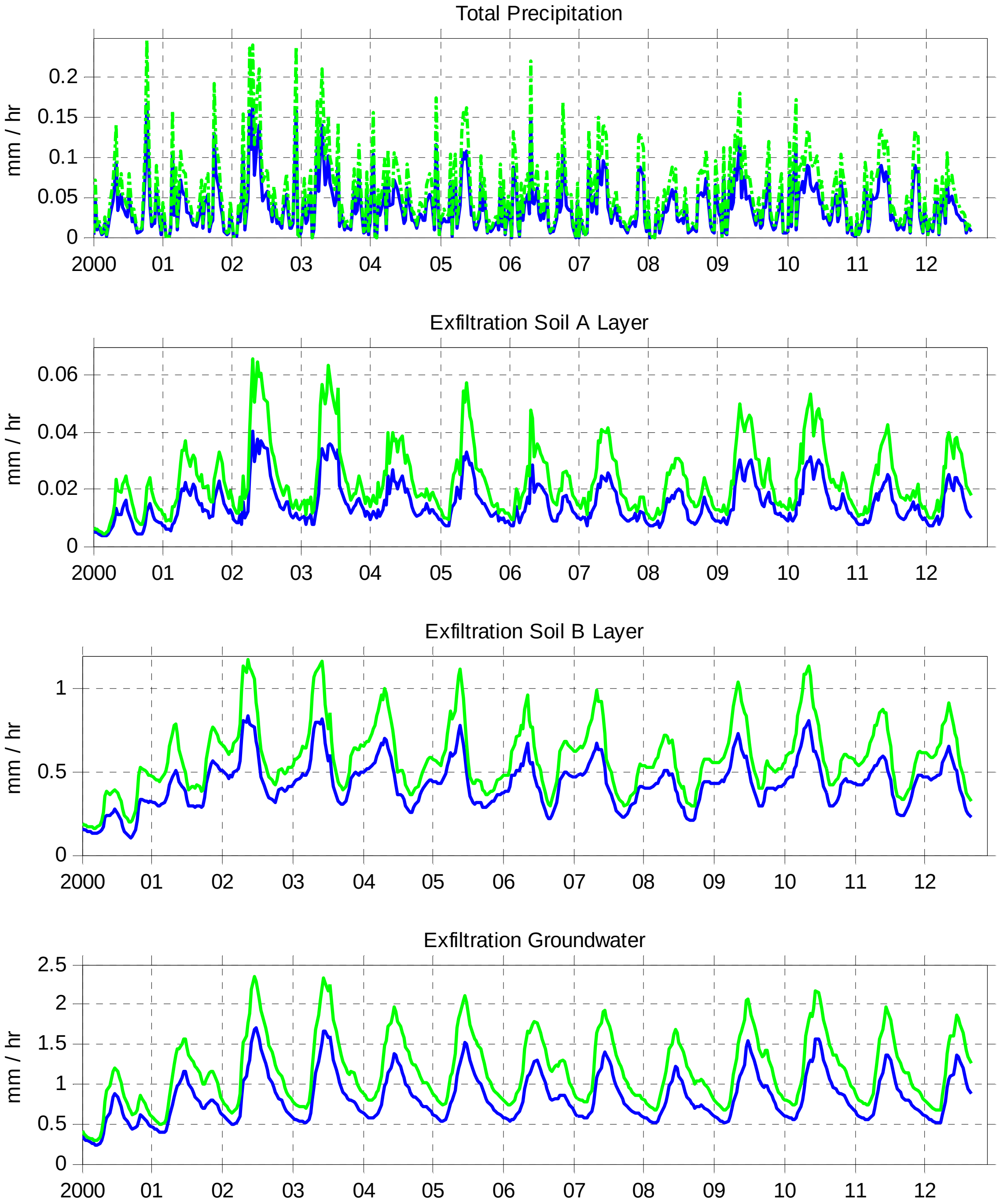

Figure 68: Exfiltration from first soil layer, second soil layer and groundwater. The time series is from 2000 to 2012 plotted as ten days averages. The blue and green lines represent model runs from TRMM-Gauge and TRMM-GPCC bias corrected precipitations respectively.

4.2.5. Water flow and water volume

The same trend is seen for water flow and water volume at the surface, in the soil layers and in groundwater i.e. they are higher in summer and decrease in winter. Figure 69 shows water flow at the surface and in the two soil layers. The surface flow is smaller as most of the water infiltrates into the soil or goes to the channel. The top soil layer has higher flow peaks because of higher conductivity and lower depth. This makes it sensitive to rainfall events and the graph shows sudden increases in May and October. The flow in the second soil layer is not as high and it shows less decrease in winter too. The lower conductivity and higher depth allows it to store and transport water at a slower rate compared to the first soil layer. It is also not very sensitive to rainfall events. The groundwater flow is significantly less because of very low conductivity.

The difference in water volume in the channel, at the surface and in the soil layers is shown in Figure 70. Please note that the y-axis in this figure is not constant for all graphs. The bottom soil layer plays an important role in feeding water to the channel as it has a higher water volume. Water stored in the second soil layer and groundwater aquifers are main sources of generating runoff in the channel during winter when there is little rain and the snow melt is small. The spatial distribution of the groundwater volume and groundwater table depth is shown in Figure 71. The floodplain area in the basin which dominantly contains the agricultural fields has higher groundwater volume. The volume is also higher along the river bed in the mountainous regions. It is minimum and close to zero at higher altitude because of steep slope and lower groundwater depth. The floodplain area is flat and serves as the collection point of groundwater flow. The groundwater table is also high in the valley and along the river and streams in the mountainous regions. The thin brown lines representing higher groundwater table at higher altitudes match well with the stream network map of the study area. This is simply because of higher seepage and discharge of groundwater into the streams.

The seasonal variation and spatial distribution of infiltration, percolation and soil saturation is also similar to the above explained variables. They are high in summer and decrease in winter (Figure 93 and Figure 94 in Appendix B). The difference in soil saturation in the floodplain and the mountains is presented in the Figure 72.

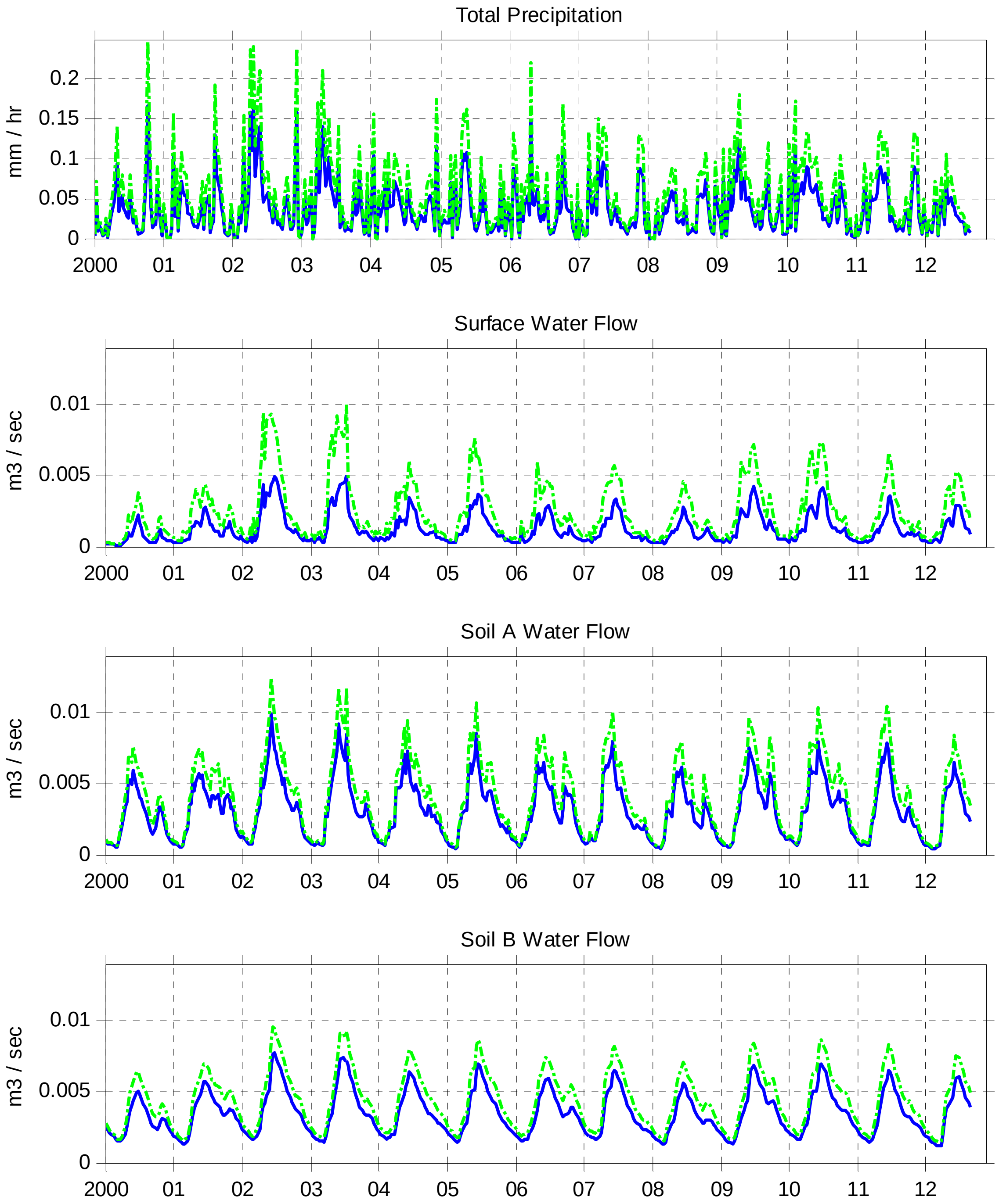

Figure 69: Flow of water at surface and in first and second soil layers. The time series is from 2000 to 2012 plotted as ten days averages. The blue and green lines represent model runs from TRMM-Gauge observed and TRMM-GPCC bias corrected precipitation respectively.

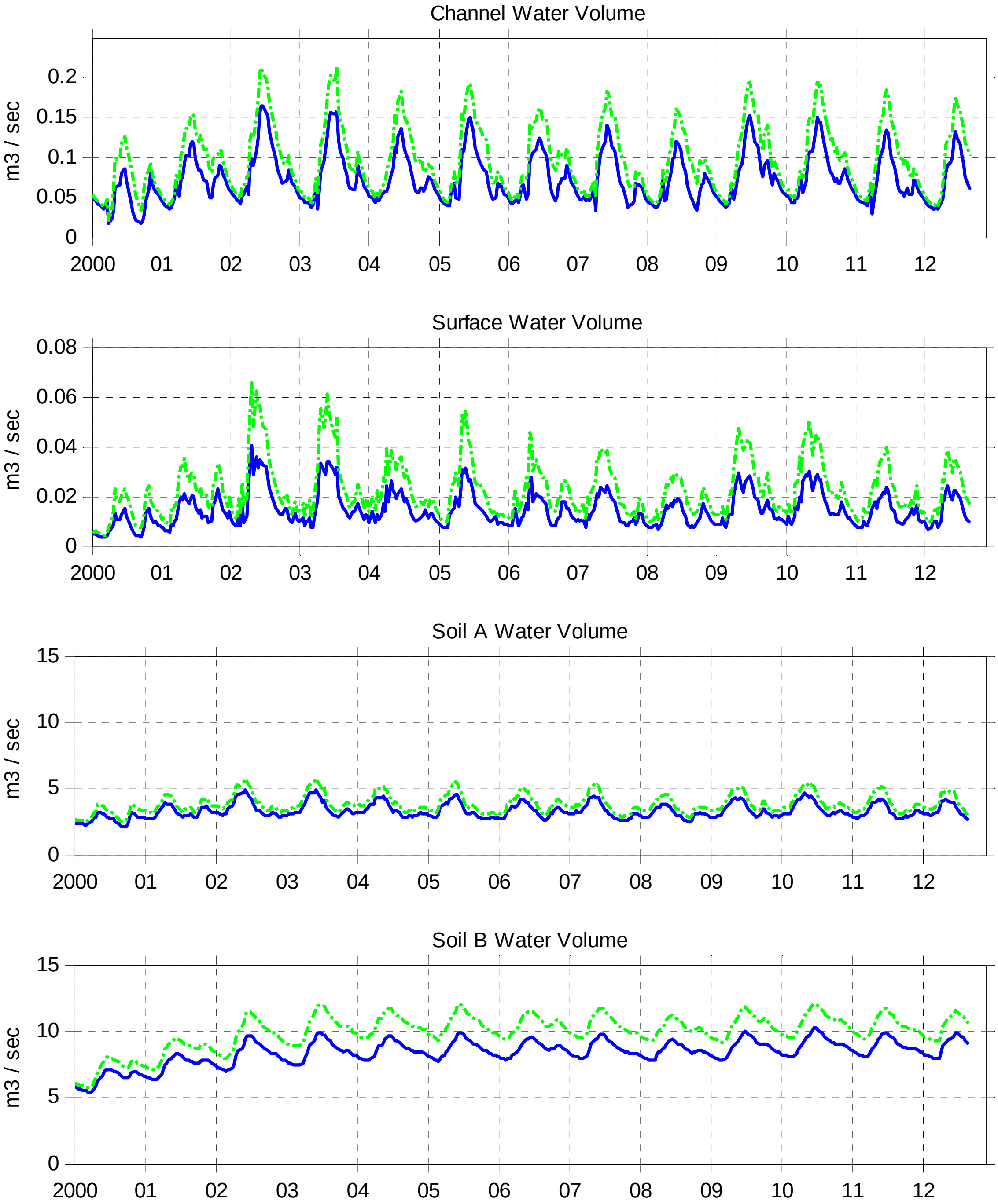

Figure 70: Seasonal variation of water volume in the channel, at the surface and in the first and second soil layers. The time series is from 2000 to 2012 plotted as ten days averages. The blue and green lines represent model runs from TRMM-Gauge observed and TRMM-GPCC bias corrected precipitation respectively.

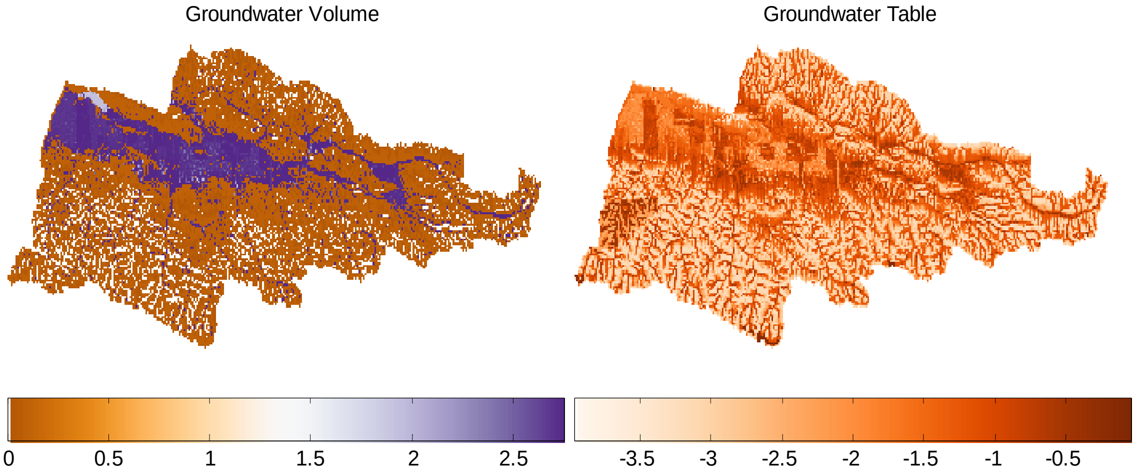

Figure 71: Mean daily groundwater volume and groundwater table from 2000 to 2012. The graphs are made from TRMM-Gauge corrected precipitation. Groundwater volume is measured in m^3 *while the table is measured in m from the surface for each pixel.*

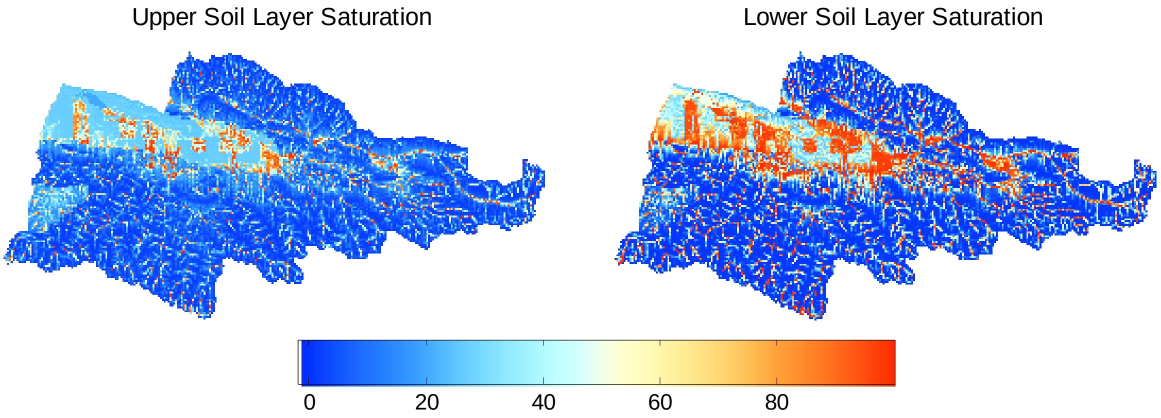

Figure 72: Saturation percentage of upper and lower soil layers and its spatial distribution in the study area. The values show average saturation (%) level from 2000 to 2012.

4.3. Irrigation Demand

The effect of water abstraction from the river to meet the irrigation demand is presented in this section. The model was run with TRMM-Gauge BC precipitation. All other inputs and parameters were kept constant while the water abstraction module was turned off only. Since there is no water abstraction before the mountainous gauging stations, they do not show any change in runoff. The cropland area in the sub-catchments of Uch Kochi and Kara Oi stations is small and the change in runoff is also little. The effect of water abstraction on river flow is prominent in the cases of Kluchevka and Kirov Reservoir gauging stations. Hence the runoff comparison is shown only for these two stations here in Figure 73. The simulated values

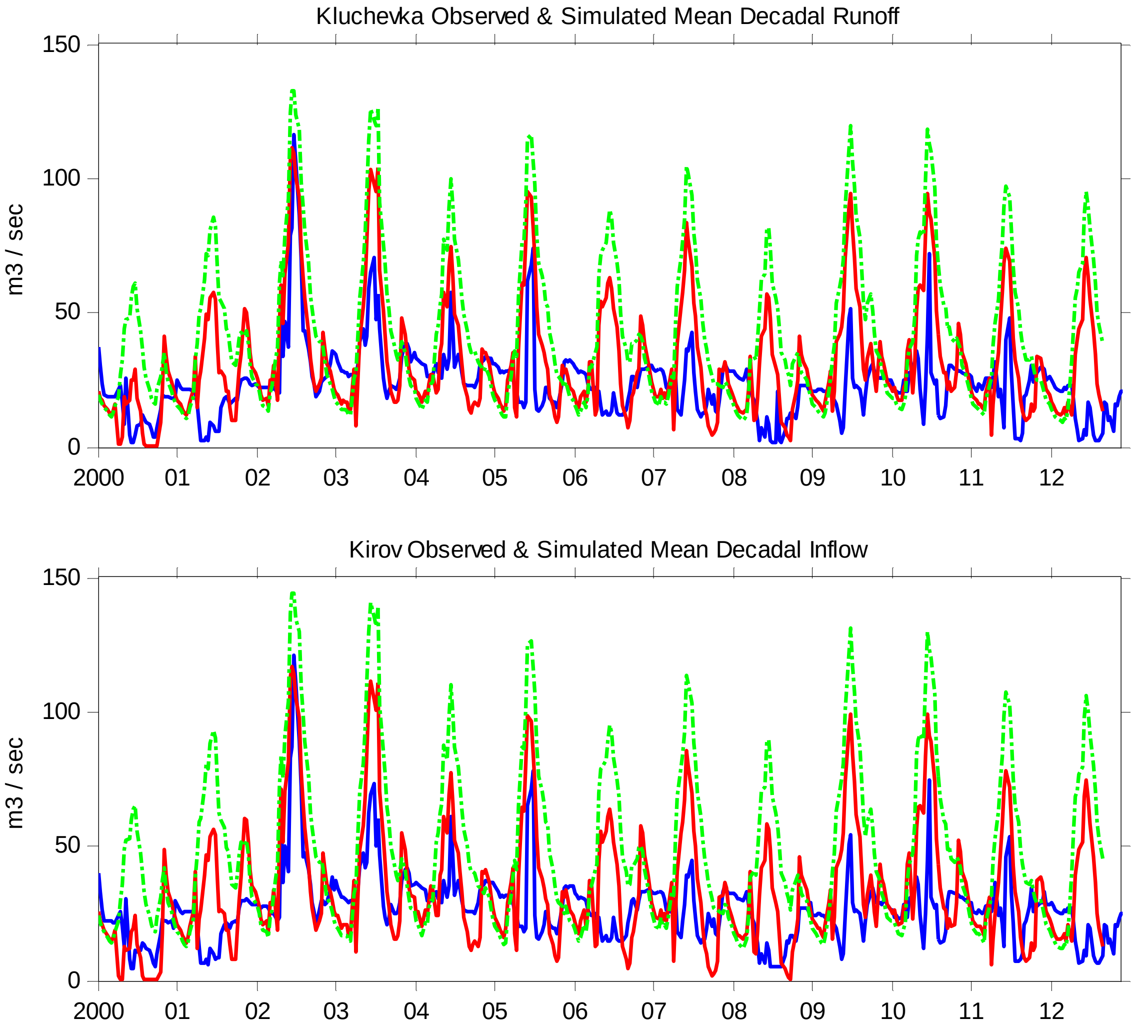

Figure 73: Observed and simulated runoff at Kluchevka and Kirov Reservoir gauging stations. The blue, red and green lines represent observed runoff, model run with irrigation and without irrigation. The time series is from 2000 to 2012 plotted as ten days average and the model was run with TRMM-Gauge bias corrected precipitation.

without water abstraction are significantly higher than the observed runoff and the modeled flow with water abstraction. The rise occurs in the summer because the water abstraction is scheduled from March to October. As the model overestimated runoff in the years 2000, 2001, 2004, 2006, 2008 and 2012, the results are already poor in case of runoff without water abstraction.

The water balance components are also examined and the results show an expected increase in channel water volume owing to absence of water use for irrigation. The surface water volume and water retained in the first and second soil layers decreases. This is shown in Figure 75 where blue and red lines represent results from model runs with and without irrigation. This causes a decrease in infiltration from the surface and percolation from soil layers. The saturation percentage of soil layers also decreases. These results are presented in Figure 94 Appendix C. Please note that the channel water volume graph shown in Figure 75 represents the average channel water volume in the whole catchment. One may think that the rise in channel water volume is not balancing the decline in surface and soil water volumes. Figure 74 shows channel water volume passing through the outlet cell of the basin. The difference is significant in this figure and the effect of water abstraction can be better understood. This graph is quite similar to runoff at Kirov because the outlet cell is very close to the reservoir gauging station.

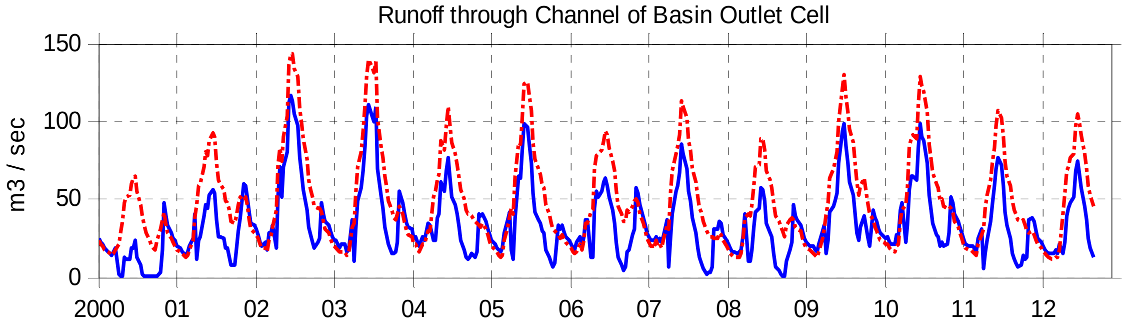

Figure 74: Water volume passing through the channel of basin's outlet cell. The results are derived from the model run with TRMM-Gauge bias corrected precipitation. The blue and broken red lines represent results for model run with and without water abstraction from the river. The time series is from 2000 to 2012 plotted as ten days averages.

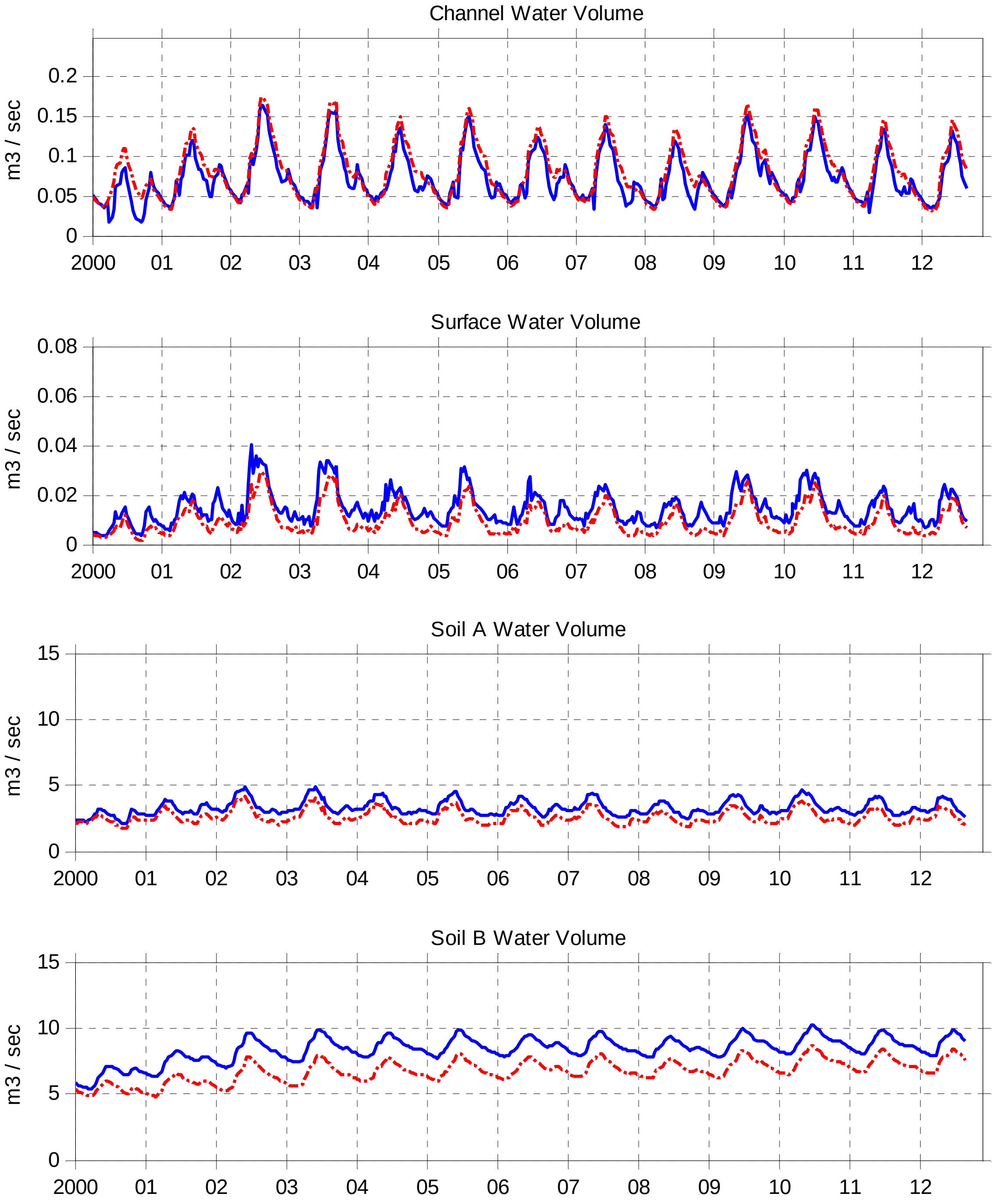

Figure 75: Variation in water volume in the channel, at surface and in the two soil layers. The results are derived from model run with TRMM-Gauge bias corrected precipitation. The blue and broken red lines represent results for model run with water abstraction and without water abstraction from the river. The time series is from 2000 to 2012 plotted as ten days averages.

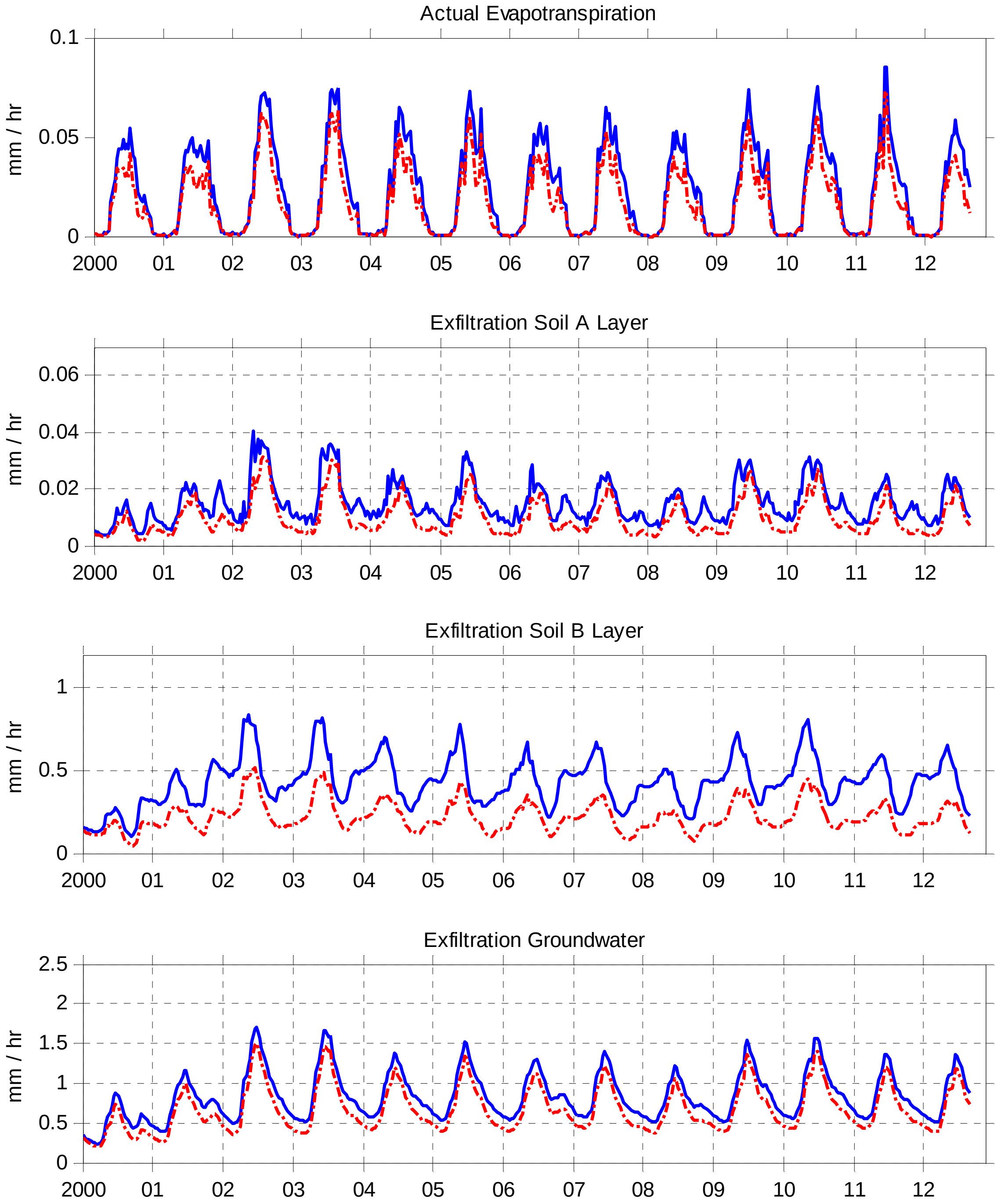

Figure 76: Difference in AET, exfiltration from the soil layers and groundwater with (blue lines) and without (broken red lines) water abstraction from the river. The results are derived from model run with TRMM-Gauge bias corrected precipitation. The time series is from 2000 to 2012 plotted as ten days averages.

The potential evapotranspiration does not change because temperature and global irradiance are identical in the two model runs. However there is a notable decrease in actual evapotranspiration in summer because less water is available in the cropland that can be transpired by the plants (Figure 76). The exfiltration from soil layers and the groundwater component also decreases because of decrease in the infiltration and surface/soil water volumes. The decrease in exfiltration is large for the second soil layer while it is small for the first soil layer and groundwater. This is related to the total water holding capacity and conductivity of each medium. The bottom soil layer has approximately double the thickness of the top layer resulting in larger decrease of water volume and exfiltration in this layer. On the other hand, the reason for small decrease in exfiltration from groundwater despite of its greater depth is because of very low hydraulic conductivity. The large water volume stored in the groundwater aquifer is still enough to keep the supply sufficient and prevent considerable decrease in exfiltration.

Table 8: Annual volumetric difference in runoff with and without irrigation. Water volume increases significantly at Kluchevka and Kirov reservoir gauging stations without irrigation. The values represent average annual volumetric difference for a period of 13 (2000 to 2012).

Station Name	Model run with Irrigation	Model run without Irrigation
Ak Tash	- 0.132	- 0.132
Besh Tash	- 0.049	- 0.051
Kumush Too	- 0.006	- 0.006
Ur Maral	- 0.084	- 0.084
Uch Kochoy	- 0.016	0.006
Kara Oi	0.019	0.080
Kluchevka	0.254	0.616
Kirov	0.219	0.700

Chapter 5

5. Annual Water Volume Forecast

Annual water volume prediction method is derived from a bachelor thesis carried out by Andreas Schmidt as part of this project (Schmidt and Farner 2013). He used Landsat images to determine snow cover area and annual water volume of Talas River. In this report, three other sources are used for forecasting annual water volume.

The snow covered area determined from MODIS was used initially to find correlation. This is the easiest method of predicting water volume as it only requires clouds free MODIS images and observed runoff. Every year the snow covered area is found by using image of 20th February because the snow cover is at maximum in this month. The area was calculated by accumulating number of pixels covered by snow and multiplying it with the pixel dimension i.e. 500 m × 500 m. The water volume is estimated by taking sum of the decadal runoff from 20 February to 31 December and converting it m^3 / year. The scatter plots between these two variables are generated for the whole basin as well as the sub-catchments on annual basis as shown in Figure 77. The gauging stations with small catchment area like Besh Tash and Kumush Too appear close to the origin while Kluchevka and Kirov show highest snow area and water volume every year due to bigger catchment area. The plots for the year 2000 have not been added to save space.

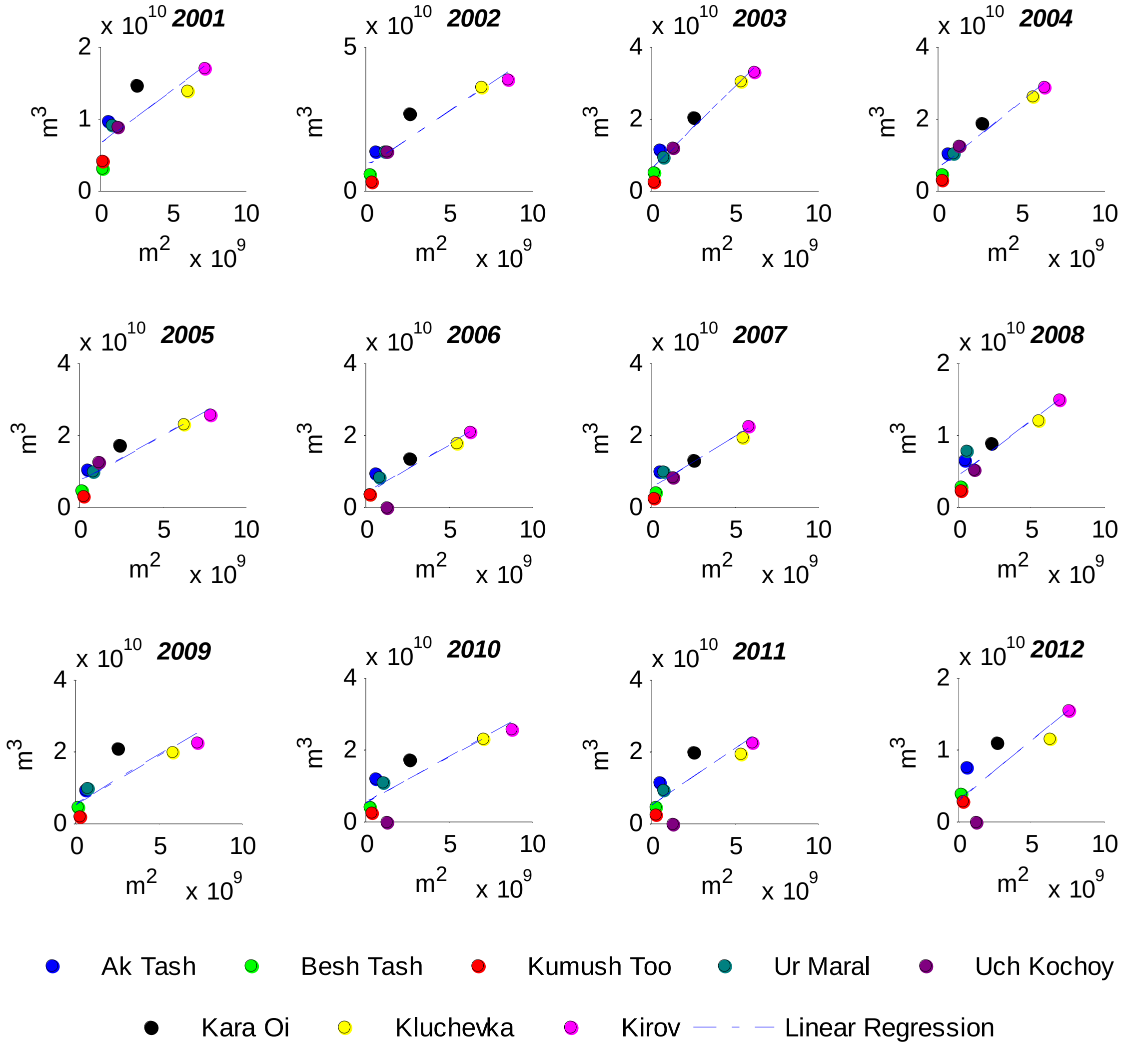

Figure 77: Correlation between MODIS snow cover and annual water volume observed at gauging stations. The scatter plots are made by calculating area covered by snow (square meter) in each sub-catchment and plotting it against the sum of water volumes (cubic meter) observed till the end of the respective year.

Figure 78 shows scatter plots made in exactly the same way but with snow cover area simulated by TOPKAPI using TRMM-Gauge corrected precipitation. The snow depth information produced by TOPKAPI is also used to find a correlation with observed runoff. The snow depth is always measured as mm of water equivalent in the model for each day. The water content of the snow was converted to volume in m^3 and scatter plots were made (Figure 79). The latter two runoff prediction strategies from snow cover and snow depth information provided by TOPKAPI require temperature, precipitation, cloud transmissivity etc. data in order to run the model. Hence extensive data is needed compared to the runoff prediction from MODIS snow cover images.

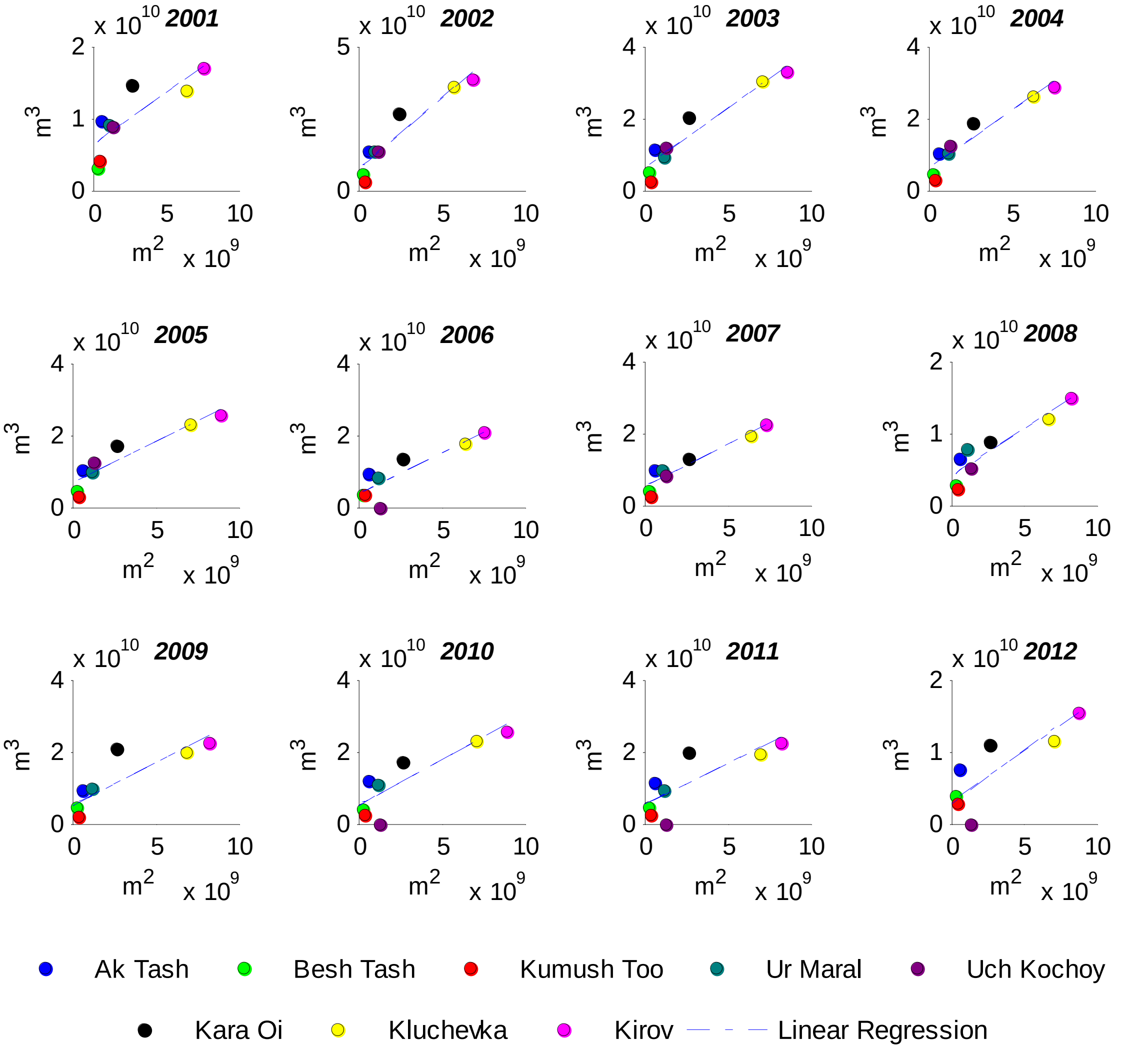

Figure 78: Correlation between TOPKAPI simulated snow cover and annual water volume observed at gauging stations. The scatter plots are made by calculating area covered by snow (square meter) in each sub-catchment and plotting it against the sum of water volumes (cubic meter) observed till the end of the respective year.

The goodness of fit between the variables in the scatter plots made by these three methods is assessed by calculating coefficient of determination (r^2). A comparison of this is presented in Table 9. All of the three methods show strong correlation and it is highest when using TOPKAPI snow water equivalent data. The correlation is low in the low runoff years particularly in 2000 and 2001. The x and y axis is not constant in the plots and a decrease in snow cover area and runoff can be observed in the low runoff years.

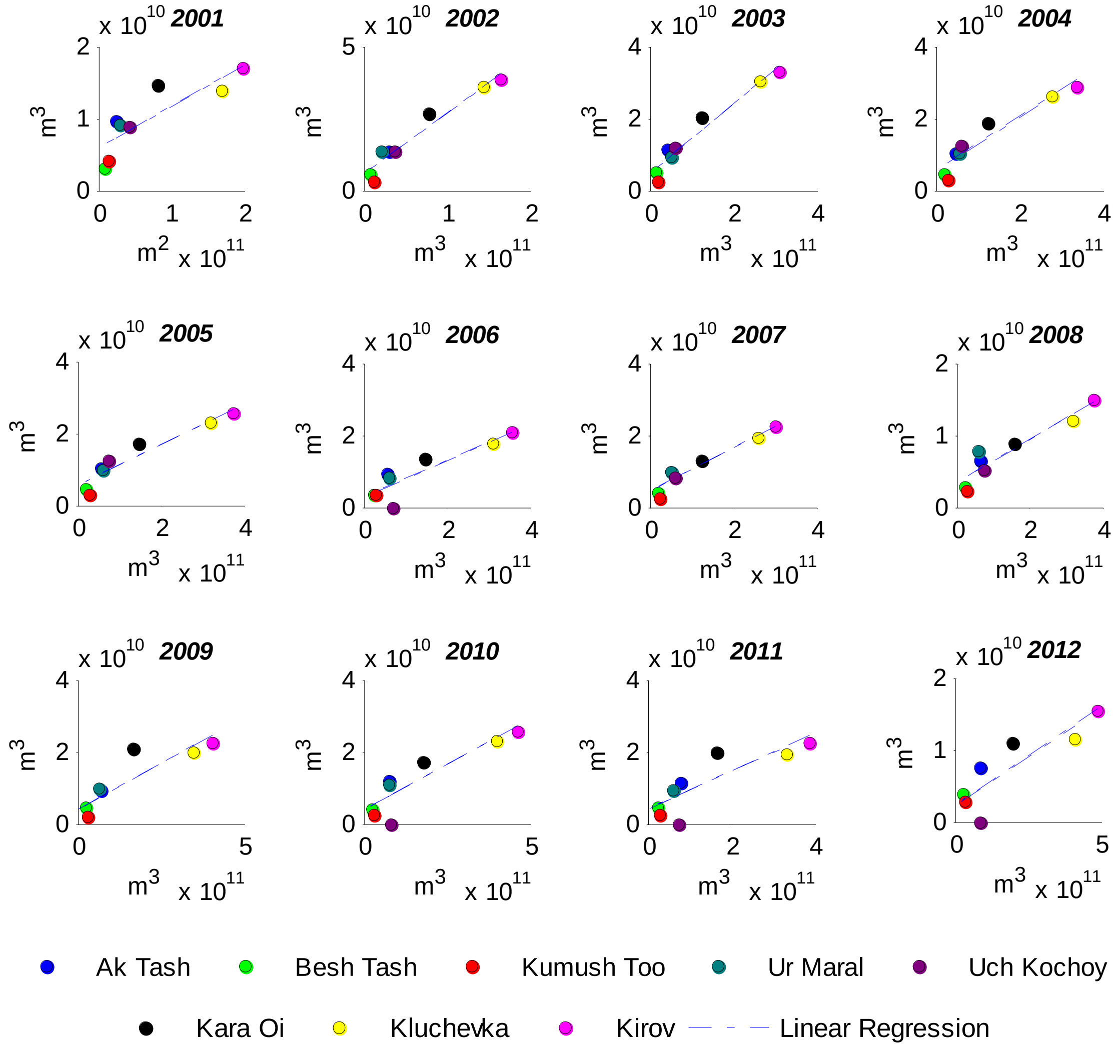

Figure 79: Correlation between TOPKAPI simulated snow water equivalent and annual water volume observed at gauging stations. The scatter plots are made by calculating snow water equivalent (cubic meter) in each sub-catchment and plotting it against the sum of water volumes (cubic meter) observed till the end of the respective year.

The correlation comparison depicts that this method can be successfully used to predict total water volume that will flow in the Talas River. It can help in managing water resources by drafting plans of water allocation for irrigation, residential area, winter release for salts flushing and decisions about sowing of crops (high or low water requirement) depending on water availability. However it has the drawback of completely ignoring runoff generation from summer and early winter precipitation. The strong correlation despite the fact that the precipitation is not considered is due to exclusion of water uses for irrigation and household purposes in the Talas city. Hence the ignorance of water addition from precipitation and water use in the city balance each other leaving a small change in the total water volume. This method cannot be used to forecast the time associated with discharge peak and decline. The only way is to use average runoff seasonality graphs from previous years to get an idea of rise and fall in the flow by rule of the thumb.

Table 9: Coefficient of determination (r^2) between snow cover/snow water equivalent and annual sum of water volume observed at runoff gauging stations from 2000 to 2012.

Year	**Coefficient of Determination (r^2)**		
	MODIS Snow Cover	***TOPKAPI Snow Cover***	***TOPKAPI Snow Water Equivalent***
2000	0.54	0.53	0.52
2001	0.70	0.69	0.74
2002	0.88	0.90	0.95
2003	0.96	0.91	0.95
2004	0.93	0.91	0.91
2005	0.86	0.86	0.90
2006	0.78	0.77	0.81
2007	0.90	0.90	0.93
2008	0.85	0.86	0.89
2009	0.75	0.73	0.80
2010	0.83	0.83	0.88
2011	0.78	0.73	0.82
2012	0.79	0.78	0.85
Mean	**0.81**	**0.80**	**0.84**

Chapter 6

6. Synthesis

6.1. Discussion

In this thesis the TOPopographic Kinematic wave APproximation and Integration (TOPKAPI) model is used to simulate the snow melt and river discharge of Talas river basin. The river flows through the cities of Talas and Taraz and supplies water to 242,600 ha of agricultural land in the two countries. The fully distributed, physically based, rainfall-runoff model was fed with the remotely sensed digital elevation map (DEM), land cover map, cloud transmissivity and precipitation data. The other data prepared includes temperature and soil map. Accuracy of the simulated discharge and snow cover area was assessed against the observed runoff from eight gauging stations and MODIS snow cover images.

The simulated discharge shows high correlation with observed data at mountainous stations while the correlation is low for floodplain gauging stations. The average snow cover efficiency was found equal to 80 % when a pixel to pixel comparison was done. Keeping in mind the limitations of observed precipitation data, no field experiments being performed and running the model from remotely sensed products, the results are very good and encouraging.

Water abstraction for irrigation purpose and inadequate precipitation and soil data are the main reasons for low correlation of floodplain gauging stations. Water abstraction causes depressions in the flow peak in May, June and August. It was also included in the model by distributing cropland into 71 irrigation districts and supplying water to them in the summer. This helped to decrease the volumetric difference in the observed and the simulated runoffs but the seasonality in the flow depression and rise could not be exactly captured.

Overestimation of precipitation in the TRMM data is the most important reason for volumetric difference and low correlation between observed and modeled discharge at Kluchevka and Kirov reservoir gauging stations. TRMM precipitation was reduced by 33 % with gauge bias correction but it is still half time (46 %) more than the observed precipitation at Talas meteorological station. This results in higher water in the hydrological system of the catchment. Provided that the water losses through evapotranspiration, infiltration are physically oriented in the model and are dependent on temperature and soil properties of each pixel, they cannot exceed a certain limit. The excess water brought through precipitation ultimately reaches Kluchevka and Kirov stations and results in moderately high volumetric difference and low correlation.

The 67 % of study area being classified as one soil type in FAO soil map resulted in negative volumetric difference for Ak Tash and Besh Tash stations despite of excess water in the system. The runoff of these stations can be increased by changing the soil properties (hydraulic conductivity, soil moisture percentage etc.) and evapotranspiration but this causes large increase in the flow at downstream stations. Hence a tradeoff had to be made between runoff differences at mountainous and floodplain gauging stations by calibrating soil properties to intermediate level. The soil map was not divided into smaller units for sub-catchments as there was no experimental proof for this and we had to rely on what was supplied by FAO.

The simulated runoff is higher in five years (low runoff years) due to overestimation of precipitation in the TRMM data. The annual difference in observed and modeled discharge reveals that the same amount (annual difference) of water is simulated by the model in the low runoff years. It follows that if the error in precipitation data is ruled out, the model results will be good in the low runoff years also.

A runoff prediction method is also proposed in this study for Talas catchment. The total water volume that will be available in one year can be forecasted by using snow cover information from MODIS images after clouds removal, TOPKAPI simulated snow cover or TOPKAPI generated snow water equivalent data. These three techniques were applied from 2000 to 2012 and the results show good correlation (r^2) of 0.81, 0.80 and 0.84 for the three techniques respectively. The prediction can help in the efficient management of water resources and the Kirov reservoir.

6.2. Conclusion

This study focuses on the use of remotely sensed precipitation data together with a physically based rainfall-runoff model, TOPAKPI; to simulate the snow melt and river discharge in Talas catchment. The major findings of the thesis are that remotely sensed data can be used to model hydrology of the basin with fair accuracy and there exists a strong coupling between the snow melt and Talas river flow. The study area is semi-arid and snowmelt is the major source of river flow in the summer. The study also shows that MODIS snow cover images can help in simulating the snow cover area and the snow melt at correct time. The information available through MODIS is a key to success in modeling un-gauged basins like our study area having tough topography and sparse weather stations.

In addition the snow cover area and snow water equivalent estimated from MODIS and TOPKAPI can be used to predict the annual water volume of Talas River. The method was successfully applied to the study area and the results showed high accuracy. This can be of great help in proper allocation of water resources and establishing management plans in well advance to consume the available water in the best possible manner. The snow melt modeling and runoff prediction strategies used in this work can be instrumental in removing the conflict between Kyrgyzstan and Kazakhstan. It can lay down foundation stone for starting a new era of friendship and trust among the two countries that have been in dispute since independence over water resources.

6.3. Further Research

There are a lot of options for further research on this study area. The future research projects can focus on the whole Talas basin which can include allocation of water for residential areas, industrial use, irrigation demand, ecosystem requirements and quantity of water that should be passed down to the salt lakes at the tail end of the catchment in Kazakhstan. This is important in order to prevent salinization of the upstream area.

We have come to know that there are more precipitation gauges distributed in the catchment but their data is not available on the internet. One has to contact Kyrgyz Hydromet Office in order to obtain this data. The precipitation information from different locations in the study area can better help in bias correcting the satellite data. This will dramatically improve the results and overestimation of runoff in the present study can be resolved.

In this thesis the basin was modeled as one unit which makes the calibration difficult as some of the parameters should not be kept constant for the whole area. Dividing the basin into sub-catchments can solve this problem. It will help in calibrating the soil and other parameters for each individual gauging station without influencing the flow of the other stations.

Real time temperature and precipitation data available from weather satellites can be a good option for forecasting runoff of the river.

Acknowledgement

There are numerous people who helped me in carrying out the project and it would have been very difficult to finish it without their kind support and guidance. I was very lucky to have five supervisors for the thesis.

First of all, I would like to extend deep gratitude for my supervisor Mr Wolfgang Kinzelbach who gave me the chance to work on this project and be part of a prestigious research group. He supported me throughout the thesis duration with his knowledge and guidance to keep me on the right track and always managed time for me despite of his busy schedule. He is not only a remarkable scientist but a very nice person also. I am thankful to him for extending the project duration and giving me enough time to finish the report. I wish to become good in time management like him.

I am grateful to my co-supervisors Tobias Siegfried and Haijing Wang for proposing the project. They helped me out whenever I got stuck, with their scientific advice and knowledge of Central Asian rivers hydrology. I always felt like being part of a family with them and will never forget the jokes we shared together. Bundle of thanks to Simone Fatichi from the core of my heart for co-supervising the thesis and for his precious time and help in setting up the TOPKAPI model (in fact three times). He helped and guided me in every step of the project from data preparation and running the model to calibration of the model and analysing the results. I hope one day I will be an expert in MatLab like him.

I would like to thank my co-supervisor Andreas Persson and master thesis coordinator Harry Lankreijer from Lund University for their valuable support and administrative assistance in carrying out the project as exchange student. I am grateful to Ms Olga Kalashnikova in Kyrgyzstan for her guidance about the study area and providing us data from Kyrgyz Hydromet Office. Thanks to Andrey Yakovlev from Kazakhstan for sharing his first-hand knowledge of the study area and Kirov reservoir as a former employee.

I am thankful to Stefan Rimkus for his guidance about data preparation for TOPKAPI model. Thanks to Peter Molnar for his cooperation in the initial phase of the project. I am grateful to Andreas Schmidt and David Farner for conducting bachelor thesis on Talas River Basin. Their work was of great help especially in the annual water volume forecast method.

I would like to extend my gratitude for Ms Vera Loehle and Erasmus exchange offices in Lund University and ETH Zurich for their assistance in completing the formal paper and administrative requirements. I feel blessed to meet helpful and cooperative people like them.

In the end, I would like to express sheer love and respect for my parents. I am hard pressed for words to extend my gratitude for their care and support. They helped and guided me through all the difficult phases of life and nurtured me to become a better person. I am grateful to my brother and sisters for their prayers and encouragement to carry out my studies with devotion.

Appendix A

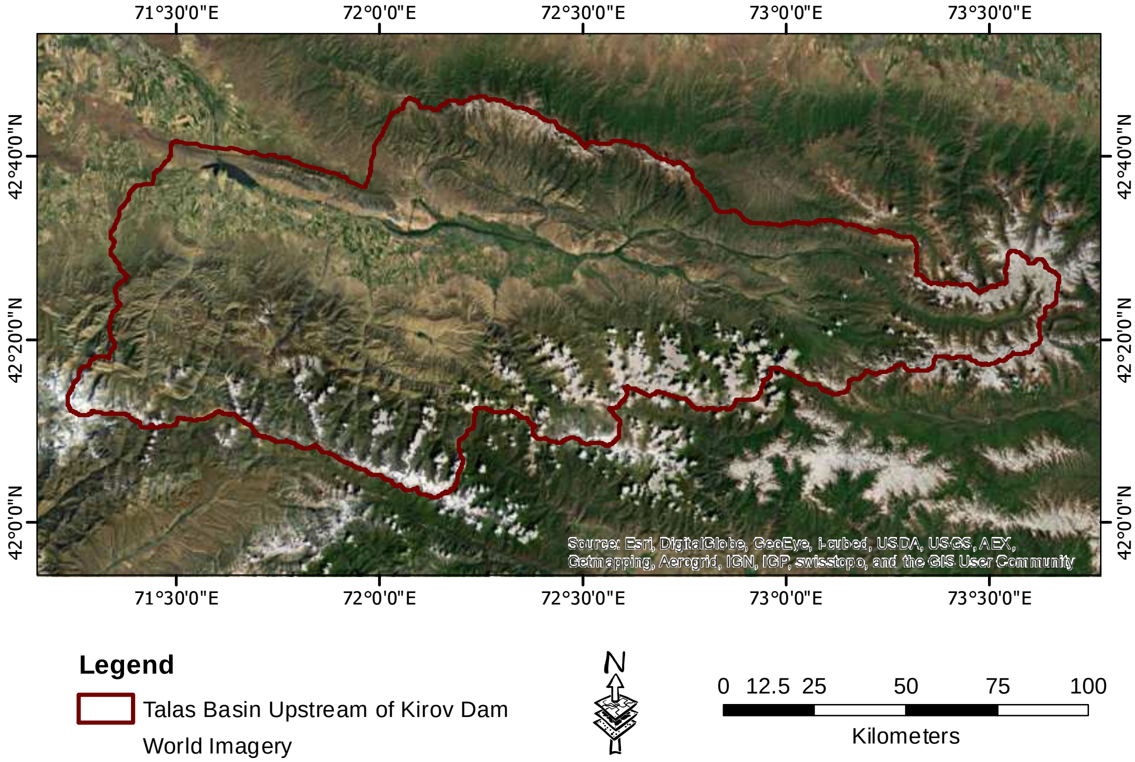

Figure 80: Landsat image of study area. Talas valley is shrouded with mountains in the north, south and east direction.

Figure 81: Huge agricultural area in Talas valley. The dry mountains and Kirov reservoir are also clearly visible.

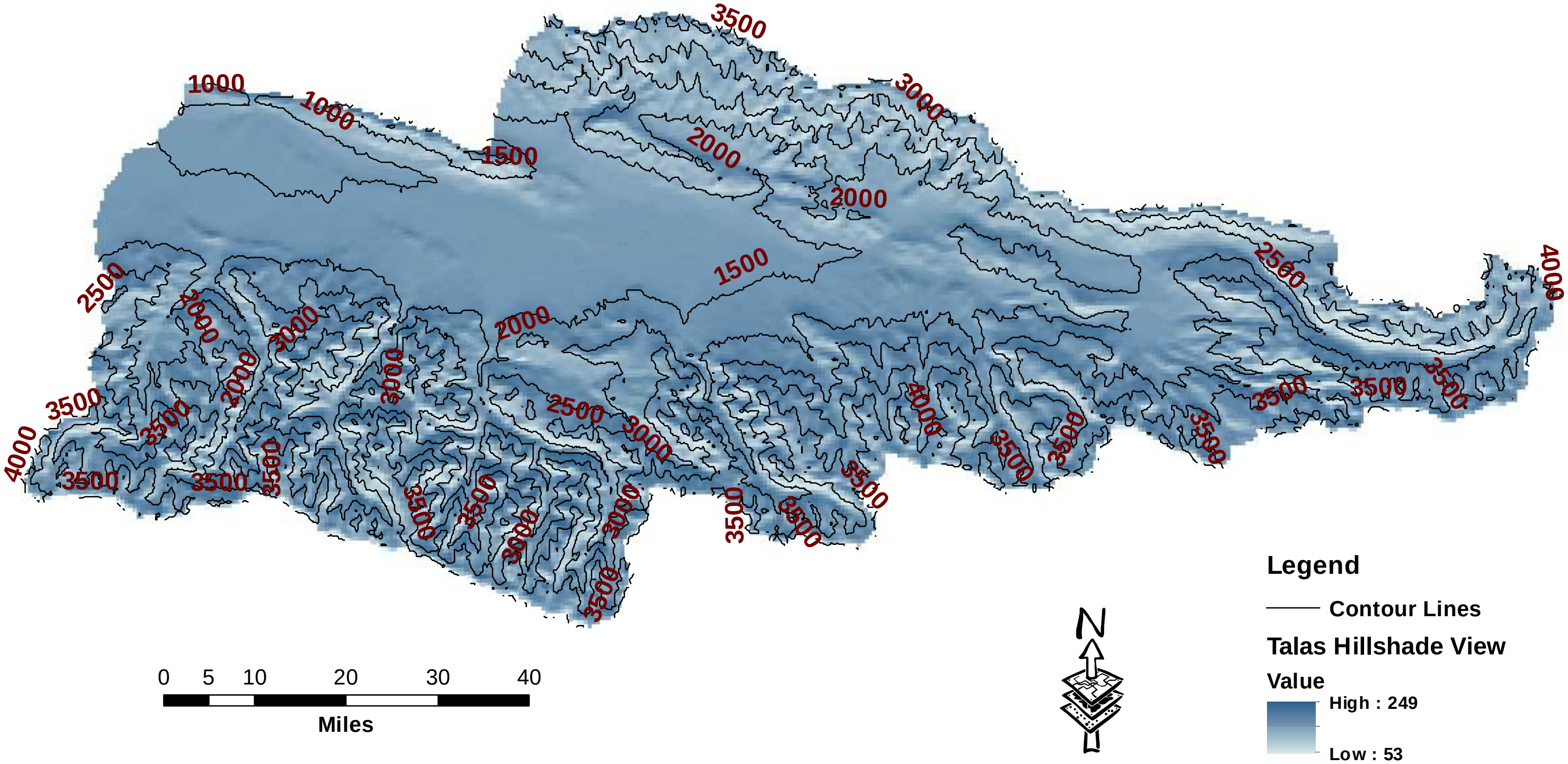

Figure 82: Contour map of Talas River Basin. The contour lines are overlayed on the hill shade view of the catchment.

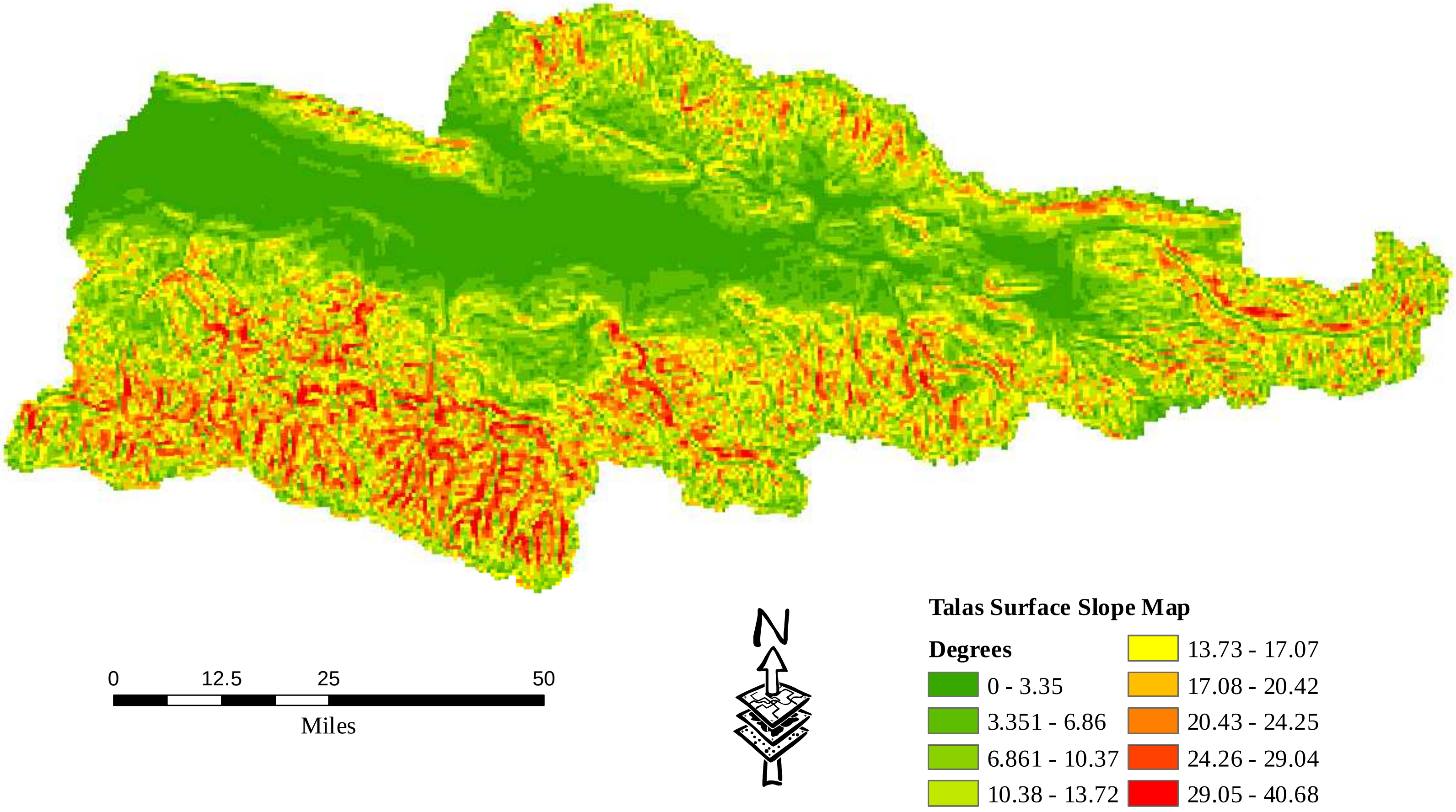

Figure 83: Variation in surface slope of the study area. The slope angle is measured in degrees.

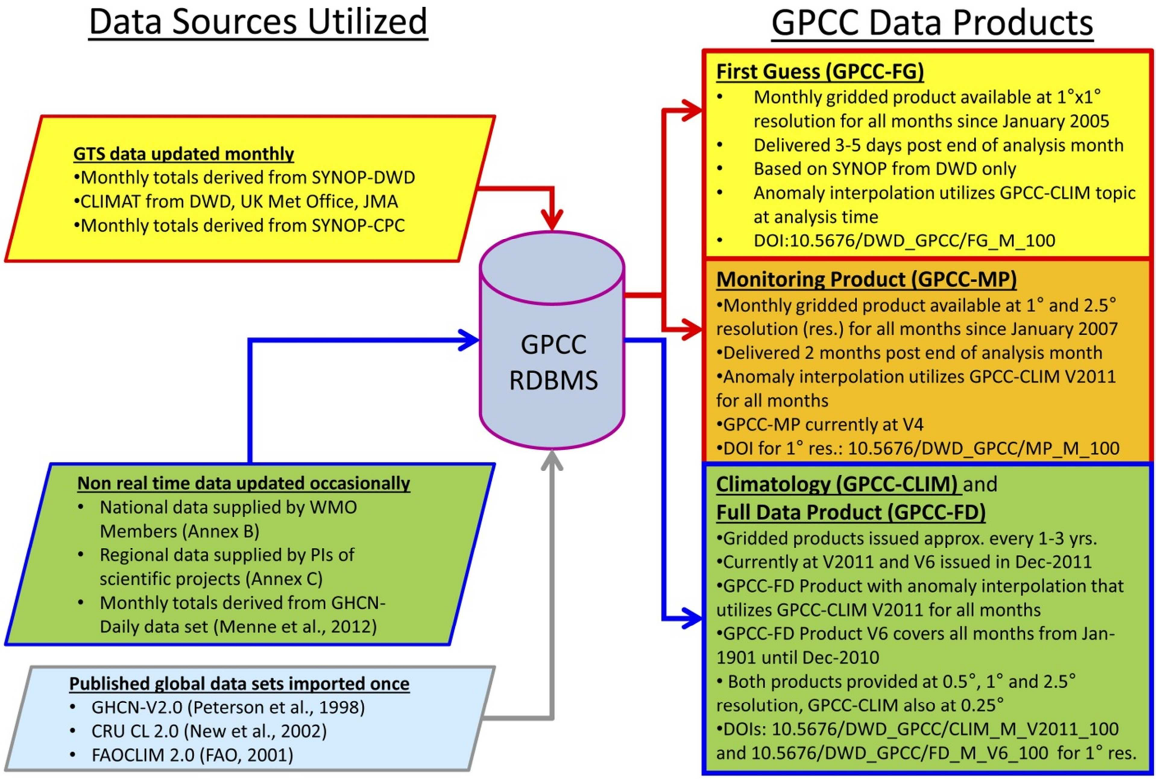

GTS data updated monthly
- Monthly totals derived from SYNOP-DWD
- CLIMAT from DWD, UK Met Office, JMA
- Monthly totals derived from SYNOP-CPC

Non real time data updated occasionally
- National data supplied by WMO Members (Annex B)
- Regional data supplied by PIs of scientific projects (Annex C)
- Monthly totals derived from GHCN-Daily data set (Menne et al., 2012)

Published global data sets imported once
- GHCN-V2.0 (Peterson et al., 1998)
- CRU CL 2.0 (New et al., 2002)
- FAOCLIM 2.0 (FAO, 2001)

First Guess (GPCC-FG)
- Monthly gridded product available at 1°x1° resolution for all months since January 2005
- Delivered 3-5 days post end of analysis month
- Based on SYNOP from DWD only
- Anomaly interpolation utilizes GPCC-CLIM topic at analysis time
- DOI:10.5676/DWD_GPCC/FG_M_100

Monitoring Product (GPCC-MP)
- Monthly gridded product available at 1° and 2.5° resolution (res.) for all months since January 2007
- Delivered 2 months post end of analysis month
- Anomaly interpolation utilizes GPCC-CLIM V2011 for all months
- GPCC-MP currently at V4
- DOI for 1° res.: 10.5676/DWD_GPCC/MP_M_100

Climatology (GPCC-CLIM) and
Full Data Product (GPCC-FD)
- Gridded products issued approx. every 1-3 yrs.
- Currently at V2011 and V6 issued in Dec-2011
- GPCC-FD Product with anomaly interpolation that utilizes GPCC-CLIM V2011 for all months
- GPCC-FD Product V6 covers all months from Jan-1901 until Dec-2010
- Both products provided at 0.5°, 1° and 2.5° resolution, GPCC-CLIM also at 0.25°
- DOIs: 10.5676/DWD_GPCC/CLIM_M_V2011_100 and 10.5676/DWD_GPCC/FD_M_V6_100 for 1° res.

Figure 84: Different sources used to feed GPCC relational database and output products.

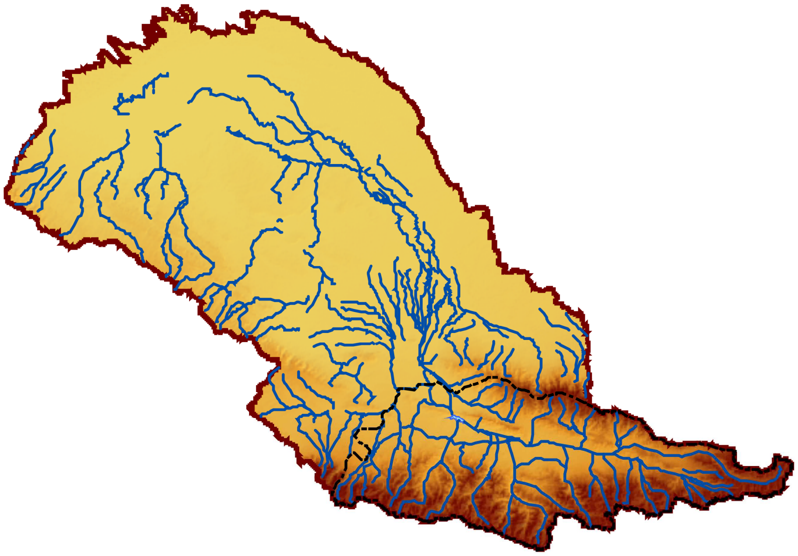

Figure 85: Generalized map of Talas River.

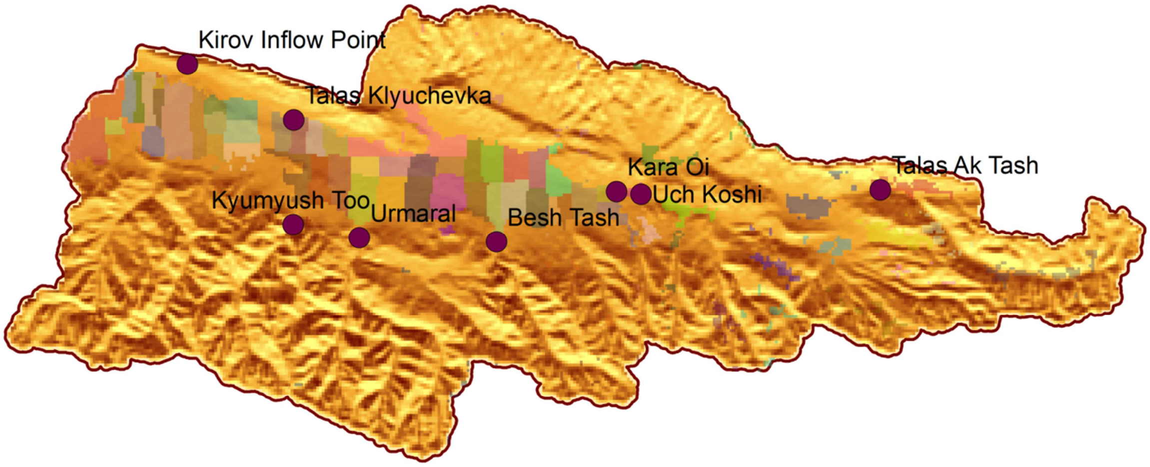

Figure 86: Talas irrigation districts (partially transparent) overlayed on the hill-shade view of the catchment. The figure shows that the agricultural area is present in the flat regions of the basin.

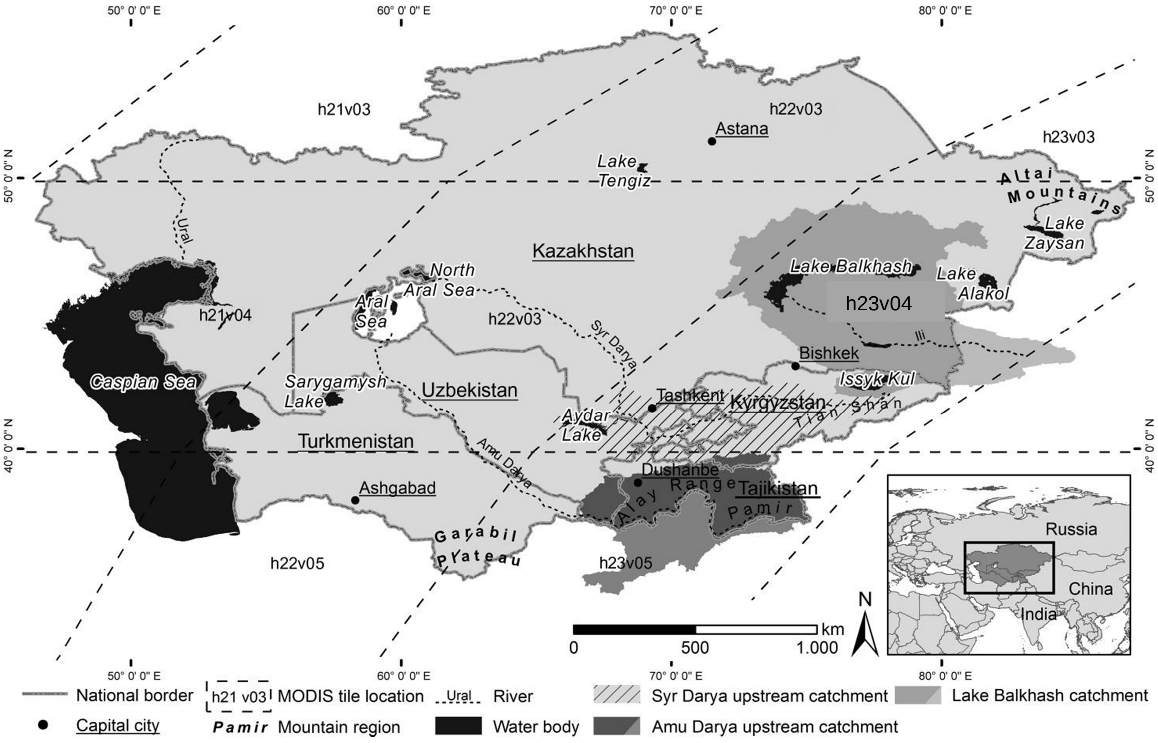

Figure 87: Scanning line of MODIS sensor. The study area is covered by the tile ***h23v04*** *(Dietz et al. 2013).*

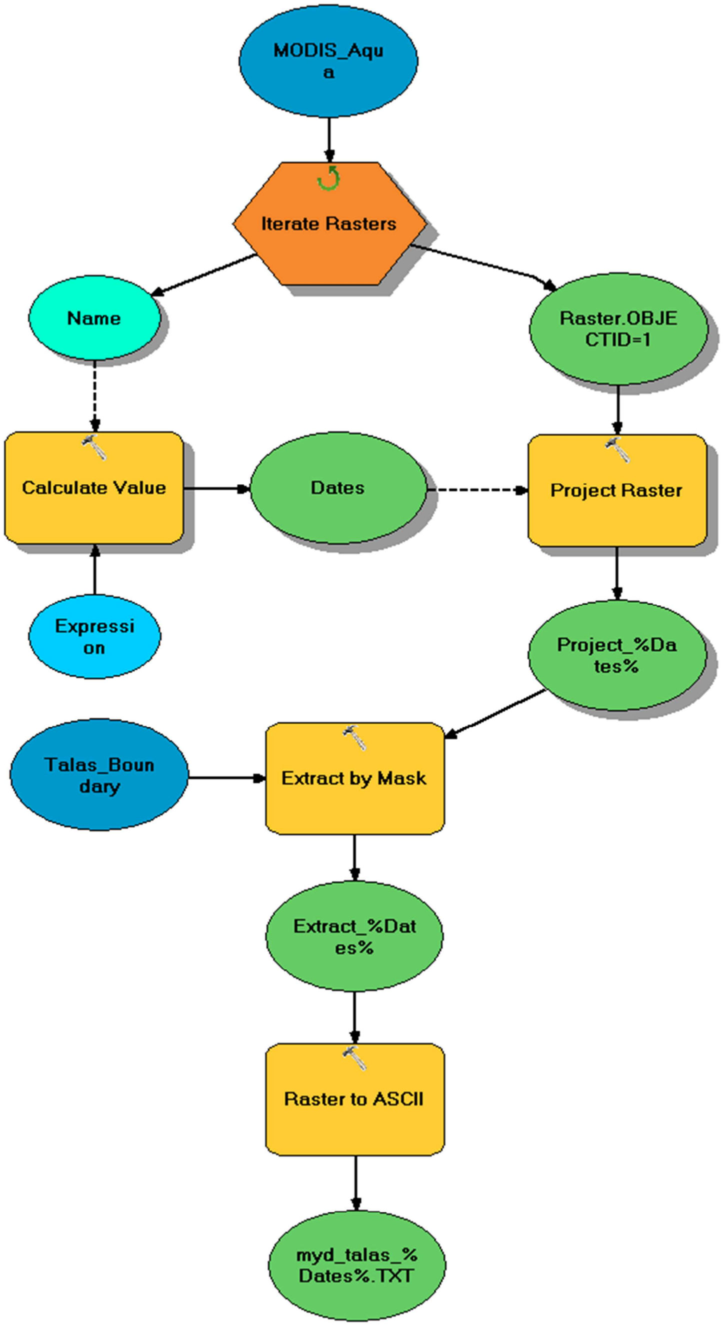

Figure 88: Flowchart of ArcGIS model designed for pre-processing of MODIS data. The preprocessing of precipitation, cloud transmissivity was also performed using similar kind of models

Appendix B

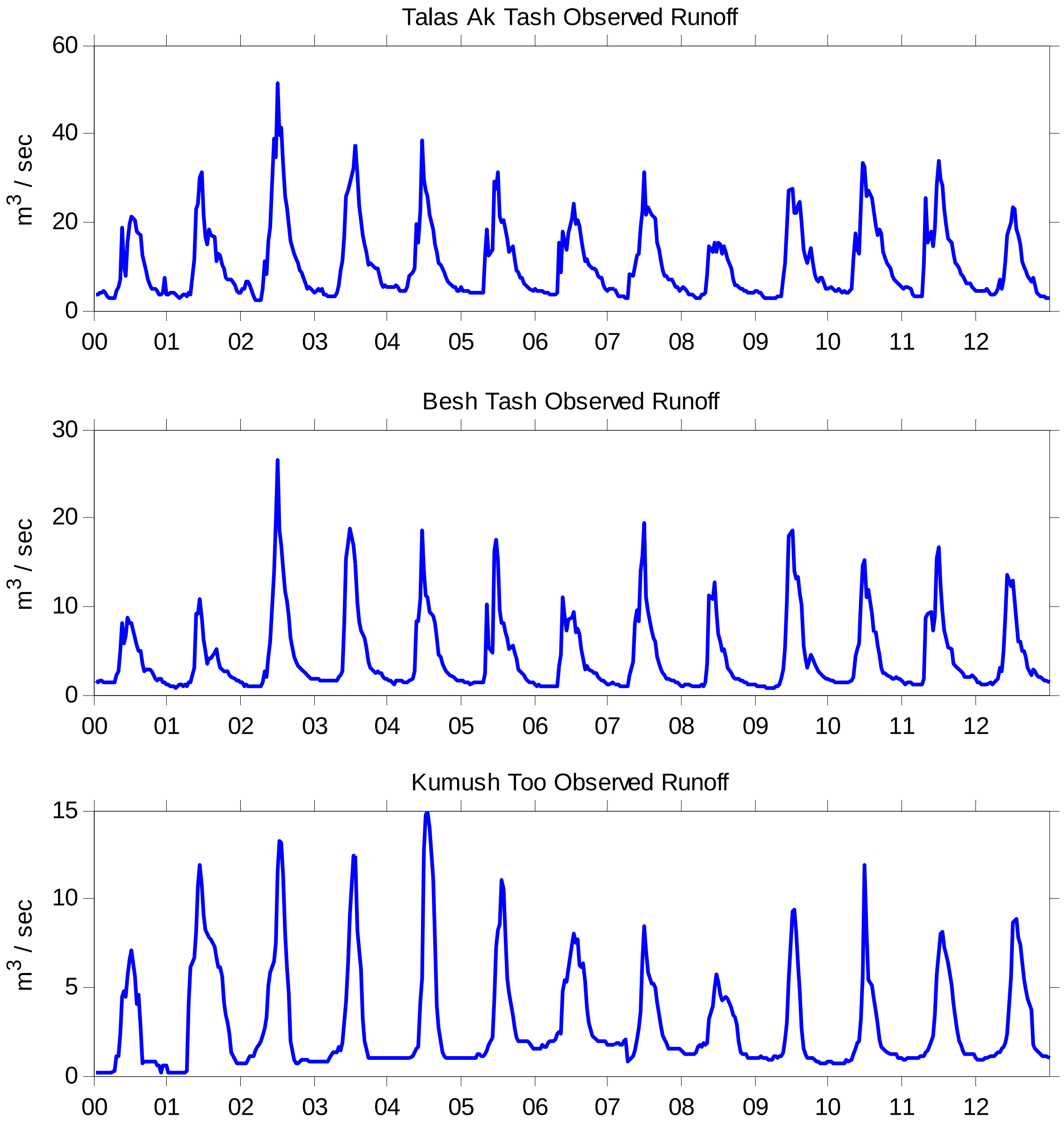

Figure 89: Observed runoffs at Ak Tash, Besh Tash and Kumush Too gauging stations. The observed data was obtained as ten days average values in m^3 */ sec from 2000 to 2012.*

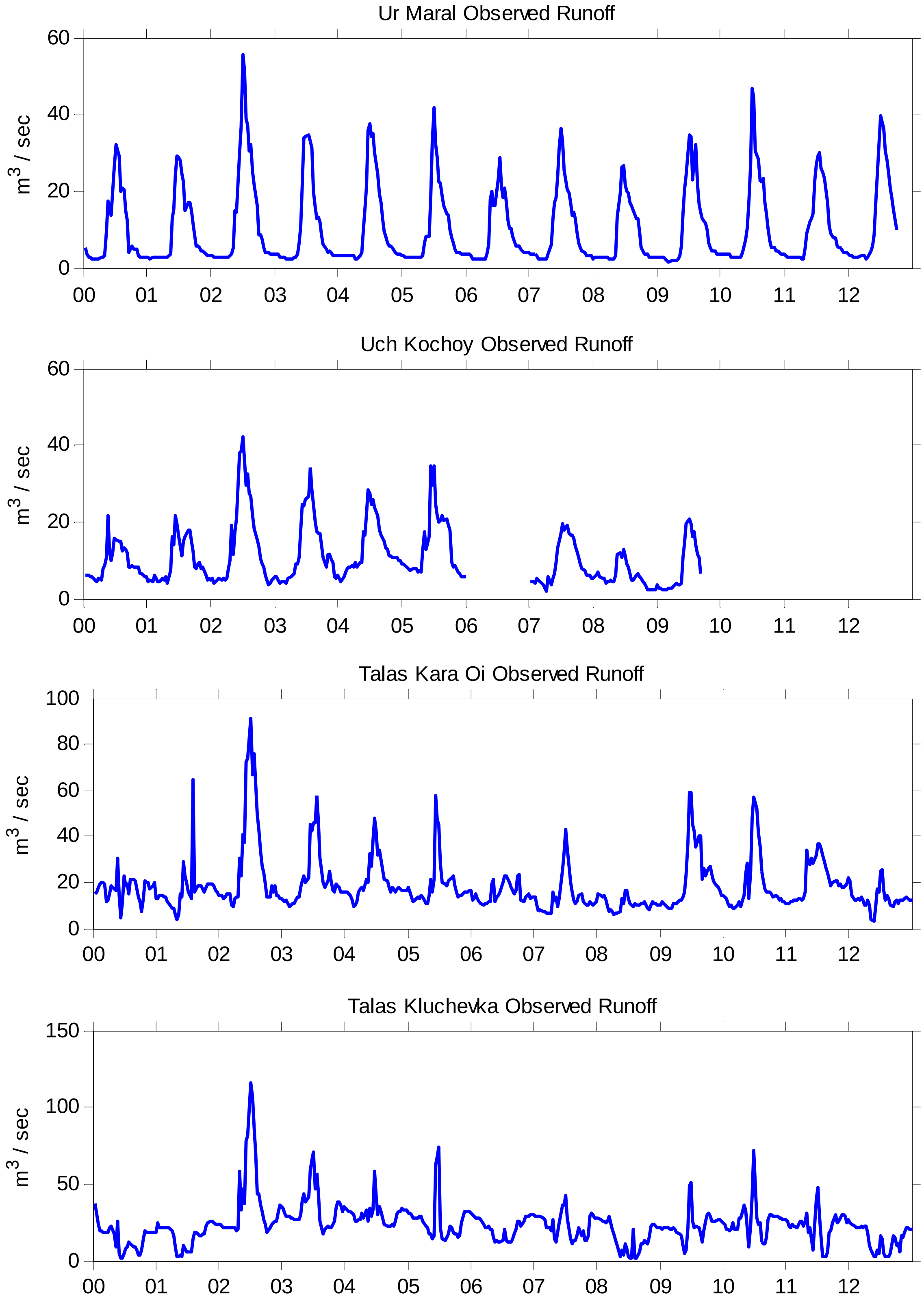

Figure 90: Observed runoffs at Ur Maral, Uch Kochoy, Kara Oi and Kluchevka gauging stations. The data was obtained as ten days average values in m^3 / sec from 2000 to 2012.

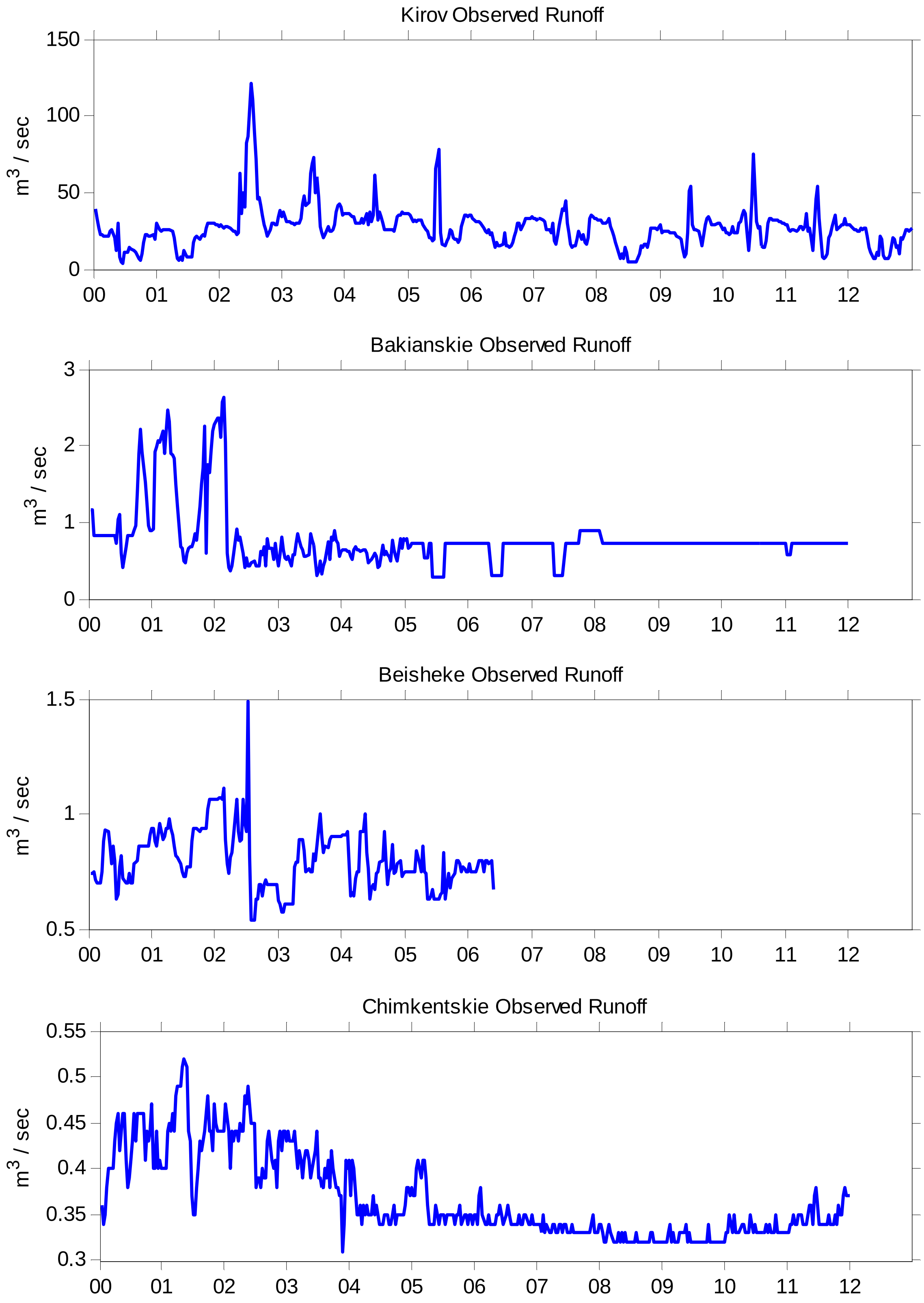

Figure 91: Observed runoffs at Kirov Reservoir, Bakianskie, Beisheke and Chimkentskie gauging stations. The data was obtained as ten days average values from 2000 to 2012.

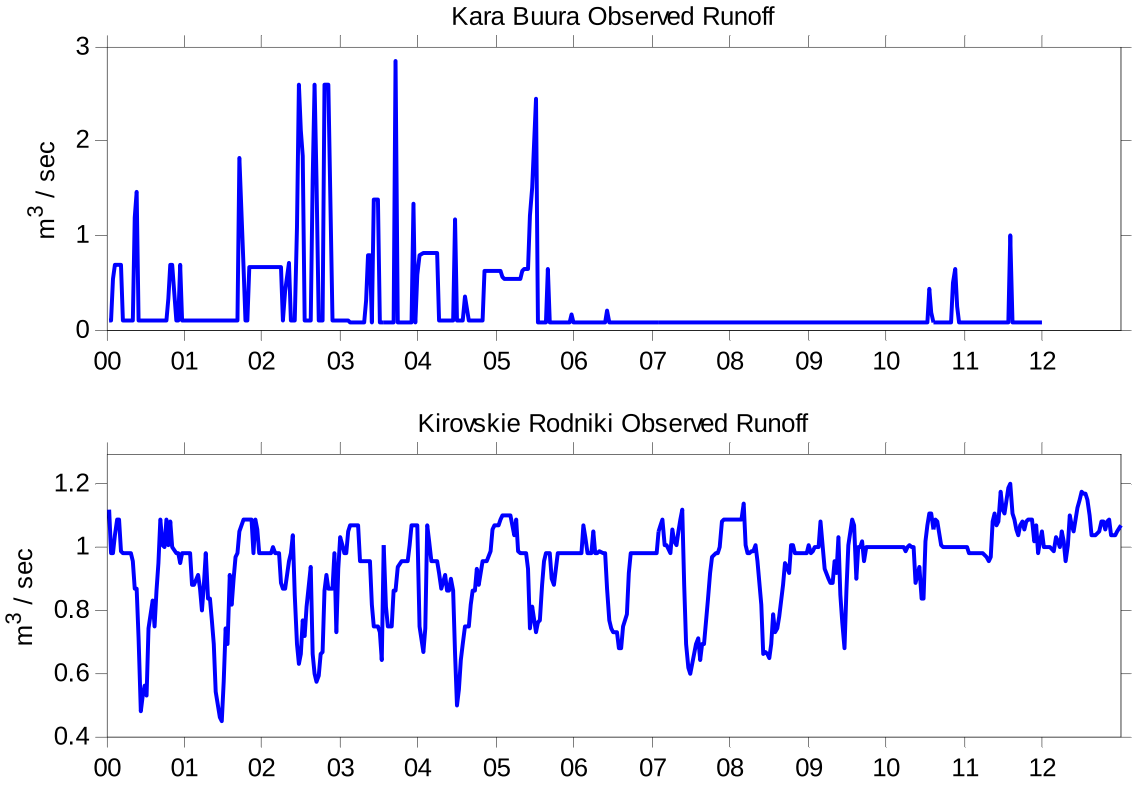

Figure 92: Observed runoffs at Kara Buura and Kirovshie Rodniki gauging stations. The data was obtained as ten days average values in m^3 / sec from 2000 to 2012.

Appendix C

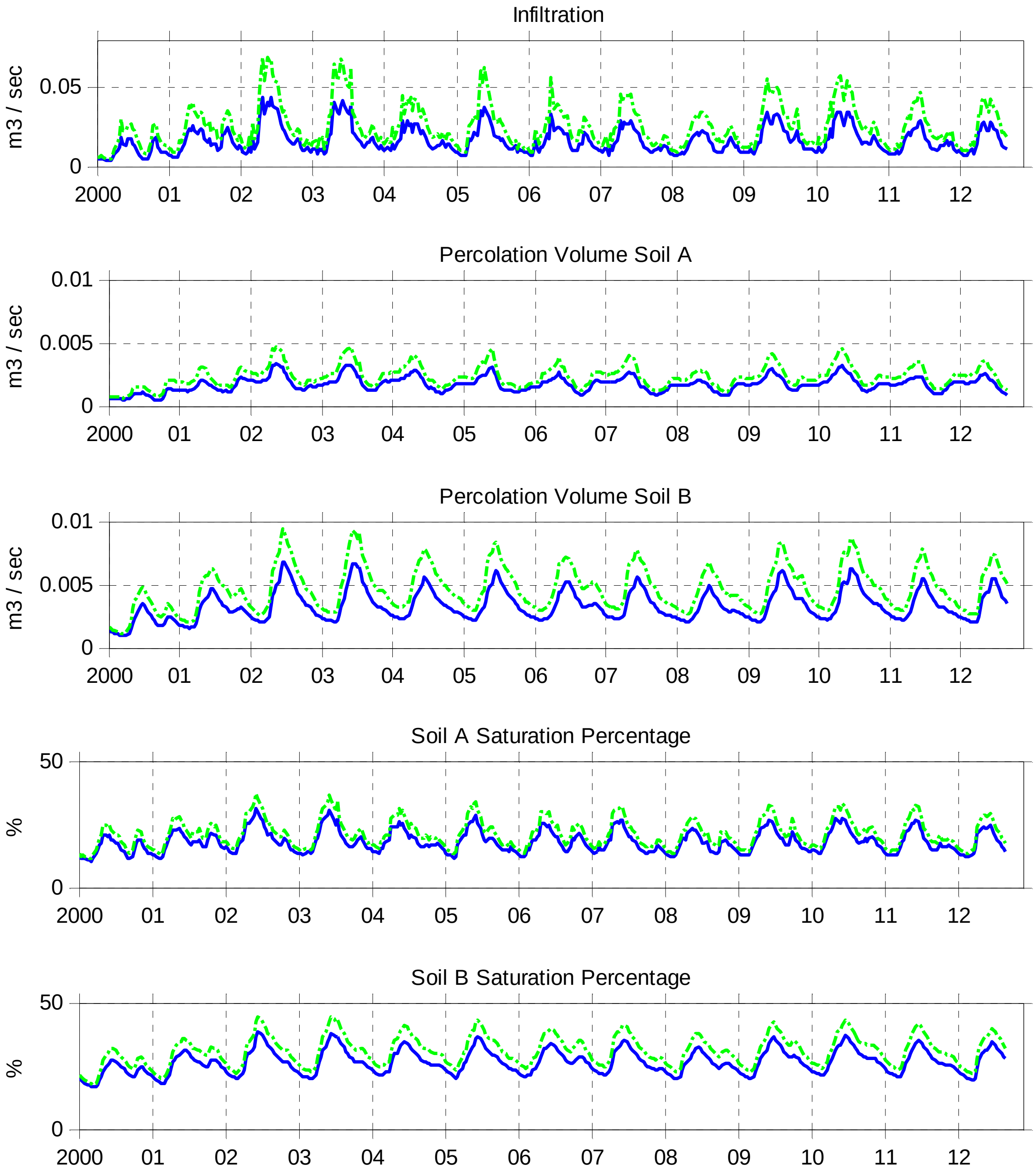

Figure 93: Total infiltration, percolation and saturation level of the first and the second soil layers. The time series is from 2000 to 2012 plotted as ten days averages. The blue and green lines represent model runs from TRMM-Gauge and TRMM-GPCC z precipitation datasets.

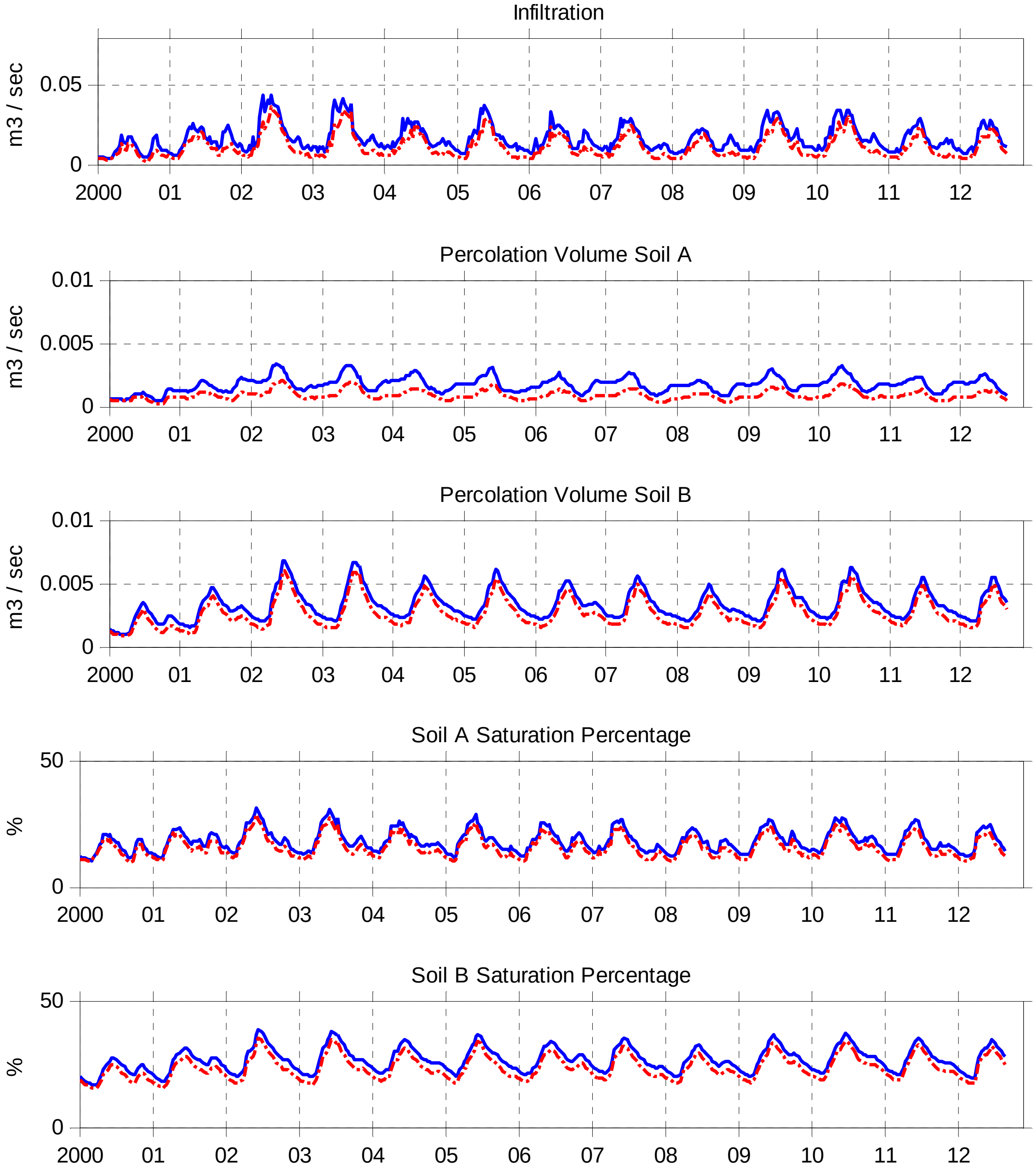

Figure 94: Change in infiltration, percolation and saturation level of the first and the second soil layers with (blue lines) and without (broken red lines) water abstraction from the river. The results are derived from model run with TRMM-Gauge bias corrected precipitation. The time series is from 2000 to 2012 plotted as ten days averages.

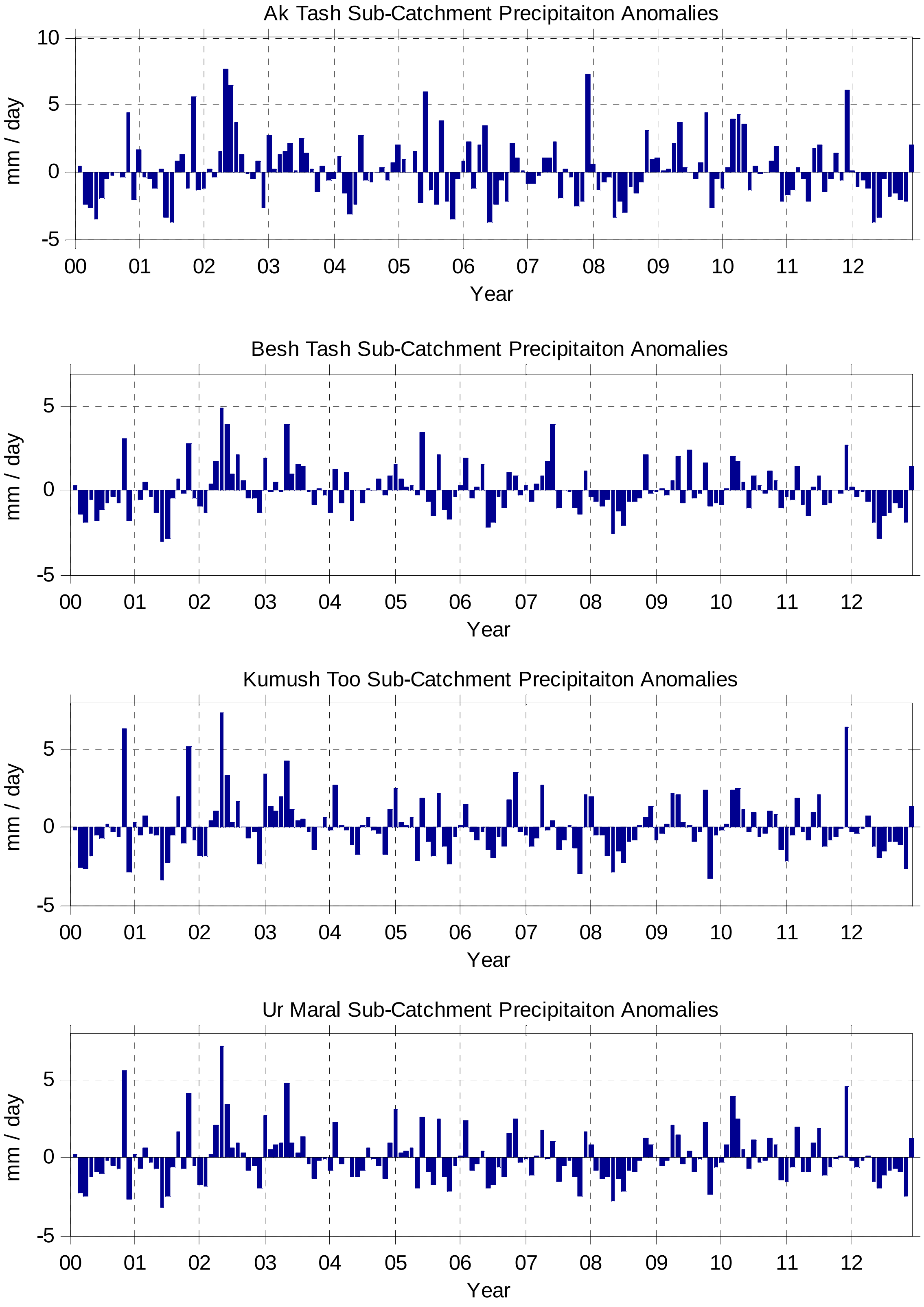

Figure 95: TRMM monthly precipitation anomalies for sub-catchments of mountainous stations. The TRMM-Gauge BC data is used in this calculation and the plot is made by taking monthly average of daily precipitation in mm.

Bibliography

Becker, A., Finger, P., Christoffer, A.M., Rudolf, B., Schamm, K., Schneider, U., and Ziese, M. 2013. A description of the global land-surface precipitation data products of the Global Precipitataion Climatology Centre with sample applications including centennial (trend) analusis from 1901 - present. *Earth System Science Data*, 5**:** 71 - 99.

Bontemps, S., P. Defourny, E. V. Bogaert, O. Arino, V. Kalogirou, and J. R. Perez (2011) GLOBCOVER 2009 Products Description and Validation *GLOBCOVER Website*. http://due.esrin.esa.int/globcover/LandCover2009/GLOBCOVER2009_Validation_Report_2.2.pdf (last accessed February 18).

Boushaki, F. I., K.-L. Hsu, S. Sorooshian, G.-H. Park, S. Mahani, and W. Shi. 2009. Bias adjustment of satellite precipitation estimation using ground-based measurement: A case study evaluation over the southwestern United States. *Journal of Hydrometeorology*, 10**:** 1231-1242. DOI: 10.1175/2009JHM1099.1

Bowman, K. P. 2005. Comparison of TRMM precipitation retrievals with rain gauge data from ocean buoys. *Journal of Climate*, 18**:** 178-190. DOI: 10.1175/JCLI3259.1

Corripio, J. 2002. *Modelling the Energy Balance of High Altitude Glacierised Basins in the Central Andes*. Phd thesis, The University of Edinburgh.

Corripio, J. 2003. Vectorial algebra algorithms for calculating terrain parameters from DEMs and solar radiation modelling in mountainous terrain. *International Journal of Geographic Information Science*, 17**:** 1 - 23.

CTWC, 2006. Report of the comission of the Republic of Kazakhstan and the Kyrgyz Republic on the use of water management facilities of intergovernmental status on the Chu and Talas rivers on its activities 2006 - 2007., Chu Talas Water Commission Report, Bishkek. [in Swedish, English summary]

CTWC, 2008. Report of the comission of the Republic of Kazakhstan and the Kyrgyz Republic on the use of water management facilities of intergovernmental status on the Chu and Talas rivers on its activities 2008 - 2009., Chu Talas Water Commission Report, Bishkek. [in Swedish, English summary]

Dietz, A. J., C. Kuenzer, and C. Conrad. 2013. Snow-cover variability in central Asia between 2000 and 2011 derived from improved MODIS daily snow-cover products. *International Journal of Remote Sensing*, 34**:** 3879-3902. DOI: 10.1080/01431161.2013.767480

Hall, D. K., G. A. Riggs, V. V. Salomonson, N. E. DiGirolamo, and K. J. Bayr. 2002. MODIS snow-cover products. *Remote Sensing of Environment*, 83**:** 181-194. DOI: 10.1016/S0034-4257(02)00095-0

Huffman, G. J., R. F. Adler, P. Arkin, A. Chang, R. Ferraro, A. Gruber, J. Janowiak, A. McNab, et al. 1997. The Global Precipitation Climatology Project (GPCP) Combined Precipitation Dataset. *Bulletin of the American Meteorological Society*, 78**:** 5-20. DOI: 10.1175/1520-0477(1997)078<0005:TGPCPG>2.0.CO;2

Joyce, R. J., J. E. Janowiak, P. A. Arkin, and P. Xie. 2004. CMORPH: A method that produces global precipitation estimates from passive microwave and infrared data at high spatial and temporal resolution. *Journal of Hydrometeorology*, 5**:** 487-503. DOI: 10.1175/1525-7541(2004)005<0487:CAMTPG>2.0.CO;2

Karlsson, K. G., and R. Hollmann (2012) Cloud Products User Manual: EUMETSAT Satellite Application Facility on Climate Monitoring. *EUMETSAT Satellite Application Facility on Climate Monitoring Website*. http://www.cmsaf.eu/bvbw/generator/CMSAF/Content/Publication/SAF__CM__DWD__PUM__GAC__CLD__1__2,templateId=raw,property=publicationFile.pdf/SAF_CM_DWD_PUM_GAC_CLD_1_2.pdf (last accessed May 30).

Kasten, F., and G. Czeplak. 1980. Solar and terrestrial radiation dependent on the amount and type of cloud. *Solar Energy*, 24**:** 177-189. DOI: 10.1016/0038-092X(80)90391-6

Konz, M., D. Finger, C. Burgi, S. Normand, W. W. Immerzeel, J. Merz, A. Giriraj, and P. Burlando. 2010. Calibration of a distributed hydrological model for simulations of remote glacierized Himalayan catchments using MODIS snow cover data. In *6th World FRIEND Conference "Global Change: Facing Risks and Threats to Water Resources", FRIEND 2010, October 25, 2010 - October 29, 2010*, 465-473. Fez, Morocco: IAHS Press.

Kummerow, C., W. Barnes, T. Kozu, J. Shiue, and J. Simpson. 1998. Tropical rainfall measuring mission (TRMM) sensor package. *Journal of Atmospheric and Oceanic Technology*, 15**:** 809-817. DOI: 10.1175/1520-0426(1998)015<0809:TTRMMT>2.0.CO;2

Lewis, R. 1962. The Irrigation Potential of Soviet Central Asia. *Annals of the Association of American Geographers*, 52**:** 99 - 114.

Libert, B., and A. Lipponen. 2012. Challenges and opportunities for transboundary water cooperation in Central Asia: Findings from UNECE's regional assessment and project work. *International Journal of Water Resources Development,* 28**:** 565-576. DOI: 10.1080/07900627.2012.684527

Nachtergaele, F., H. V. Velthuizen, and L. Verelst (2009) FAO HWSD Database User Guide. *Food and Agriculture Organization*. http://www.fao.org/fileadmin/templates/nr/documents/HWSD/HWSD_Documentation.pdf (last accessed March 1).

O'Hara, S. L. 2000. Central Asia's water resources: contemporary and future management issues. *International Journal of Water Resources Development*, 16**:** 423-441.

Pellicciotti, F. 2004. *Development of an ice and snow melt model for long-term analysis of water resources from highly glacierised basins.* . Phd thesis, Swiss Federal Institute of Technology Zurich.

Pellicciotti, F., B. Brock, U. Strasser, P. Burlando, M. Funk, and J. Corripio. 2005. An enhanced temperature-index glacier melt model including the shortwave radiation balance; development and testing for Haut Glacier d'Arolla, Switzerland. *Journal of Glaciology,* 51**:** 573-587.

Pellicciotti, F., C. Buergi, W. W. Immerzeel, M. Konz, and A. B. Shrestha. 2012. Challenges and uncertainties in hydrological modeling of remote hindu KushKarakoramHimalayan (HKH) Basins: Suggestions for calibration strategies. *Mountain Research and Development,* 32**:** 39-50. DOI: 10.1659/MRD-JOURNAL-D-11-00092.1

Porkka, M., M. Kummu, S. Siebert, and M. Florke. 2012. The role of virtual water flows in physical water scarcity: The case of Central Asia. *International Journal of Water Resources Development,* 28**:** 453-474. DOI: 10.1080/07900627.2012.684310

Rasskazchikov, V. A. 2010. Hydrotechnical construction: Condition of the concrete in the dam retaining the kirov reservoir on the talas river in kyrgyzstan. *Power Technology and Engineering,* 44**:** 1 - 6.

Riggs, G. A., D. K. Hall, and V. V. Salomonson (2006) MODIS snow products user guide to collection 5. *National Snow and Ice Data Center (NSIDC)* http://nsidc.org/data/docs/daac/modis_v5/dorothy_snow_doc.pdf (last accessed November 1).

Rodina, E., M. Anna, and K. Sergi. 2008. Integrated Water Resource Management of Transboundary Chu and Talas River Basins. *Transboundary Water Resources: A Foundation for Regional Stability in Central Asia***:** 123 - 129.

Schmidt, A., and D. Farner, 2013. Predicting Summer Streamflow from Spring Snowpack in a Catchment in Kyrgyzstan. Report, Zurich. [in Swedish, English summary]

Smith, T. M., P. A. Arkin, J. J. Bates, and G. J. Huffman. 2006. Estimating bias of satellite-based precipitation estimates. *Journal of Hydrometeorology*, 7**:** 841-856. DOI: 10.1175/JHM524.1

Tesfagiorgis, K., S. E. Mahani, N. Y. Krakauer, and R. Khanbilvardi. 2011. Bias correction of satellite rainfall estimates using a radar-gauge product – a case study in Oklahoma (USA). *Hydrol. Earth Syst. Sci.*, 15**:** 2631-2647. DOI: 10.5194/hess-15-2631-2011

UNECE, 2007. OUR WATERS: JOINING HANDS ACROSS BORDERS, First Assessment of Transboundary Rivers, Lakes and Groundwaters. United Nations Publications Report, Geneva. [in Swedish, English summary]

UNECE, 2011. Second Assessment of Transboundary Rivers, Lakes and Groundwaters. United Nations Publications Report ISBN 978-92-1-117052-8, Geneva. [in Swedish, English summary]

WARMAP, 1996. Water Resources Management and Agricultural Production in the Central Asian Republic. Report, Tashkent. [in Swedish, English summary]

HAMMAD JAVID

Tiechestrasse 49
8037, Zurich
Switzerland
Mob: +41 78 65 80 542
hammad_precocious@hotmail.com

Summary

- ✓ Superior knowledge in snow ablation, surface and groundwater hydrology.
- ✓ Advance knowledge in GIS, Satellite Remote Sensing and MatLab.
- ✓ Experience of working as a Water Resources Engineer and vast academic projects work.
- ✓ Good interpersonal, analytical, communicational, technical and management skills.
- ✓ Good teamwork ability, goal oriented and excellent learning attitude.

Education

M.Sc Physical Geography & Ecosystem Analysis (Continued) Jan 2011 – …… 2014
ETH, Zurich - Lund University, Sweden

Major: Hydrology, hydrologic cycle, ecosystem modeling, GIS, satellite remote sensing.
Minor: Image processing, cartographic and spatial analysis, map projections, interpolations, greenhouse gases, climate system, meteorology, palaeo-climate, radiation balance, vegetation dynamics.

B.Sc Agricultural Engineering Sep 2005 – Aug 2009
University of Agriculture, Faisalabad

Major: Surface & groundwater hydrology, machine designing, waste water treatment, thermodynamics, farm structures
Minor: Engineering statics & dynamics, soil mechanics & dynamics, Engineering drawing, surveying & leveling, field crops, biogas, remote sensing, turbines, pumps, I.C engines, drainage.

Experience

Snow Melt & Runoff Assessment of Talas River Basin, Kyrgyzstan Dec 2012 – Nov 2013
Swiss Federal Institute of Technology (ETH) Zurich
Responsibilities: This project is part of master thesis being carried out at ETH, Zurich. The runoff of Talas River is determined by snow melt and precipitation in the mountains. Rainfall data was obtained from remotely sensed TRMM, CMORPH & GPCC products. Digital Elevation Model, Soil map, Land Cover map & Fractional Cloud Cover data were obtained from ASTER DEM, FAO, Globe Cover and CF-SAM datasets respectively. All these inputs together with real time temperature data from NCDC were fed to TOPKAPI (Topographic kinematic approximation and integration) model to simulate runoff and snow covered area of Talas Basin from 1998 – 2012. The modeled runoff is compared with observed runoff from 8 Gauging Stations. Snow cover maps generated by the model are compared with MODIS Cryosphere product.
Contact: Tel.: + 41 44 63 33 075 – Fax: + 41 44 63 31 061
Web Link: http://www.ethz.ch/index_EN , http://www.ifu.ethz.ch/index_EN

Bachelor Thesis Co - Supervision Mar 2013 – Jun 2013
Predicting Summer Stream Flow from Spring Snowpack in a Catchment in Kyrgyzstan
Students: Andreas Schmidt and David Farner
Abstract: Correlation between snow covered area in spring and runoff volume in summer is found by developing a simple model. The predictions of runoff from the model are used as basis for reservoir management plan.

National Internship Program Mar 2010 – Feb 2011
Chief Engineer Faisalabad Irrigation Zone
Responsibilities: The internship was mainly aimed at managing flow of water in canals depending on season and amount of area to be irrigated. Apart from that lining of canals and designing of outlets for supplying water from canals to the fields was also carried out.
Contact: Tel.: (92-41) 92 00 268, 92 00 270 – Fax: (92-41) 92 00 277

Internship Jul 2008
Pakistan Council of Research in Water Resources (PCRWR)
Responsibilities: The main responsibilities included study of surface, ground water resources, annual inflow through precipitation, snowfall and melting of glaciers. Water required for irrigation and hydropower purposes.
Contact: Tel.: (92-51) 92 58 477 – Fax: (92-51) 92 58 963 – Website: http://www.pcrwr.gov.pk

Computer Skills

- Proficient user of **ArcGIS**, **MatLab**, Microsoft Office, IDRISI
- Beginner level of ERDAS Imagine, Pro-Engineering, AutoCAD, C++, Adobe Photoshop

Hobbies

- Extra-Curricular activities I have been doing so far are Equitation, Swimming, Cricket, Badminton, Photography, Reading, Movies and Songs. Big plans for future ☺

Seminar Series

Institutionen för naturgeografi och ekosystemvetenskap, Lunds Universitet.

Student examensarbete (Seminarieuppsatser). Uppsatserna finns tillgängliga på institutionens geobibliotek, Sölvegatan 12, 223 62 LUND. Serien startade 1985. Hela listan och själva uppsatserna är även tillgängliga på LUP student papers (www.nateko.lu.se/masterthesis) och via Geobiblioteket (www.geobib.lu.se)

The student thesis reports are available at the Geo-Library, Department of Physical Geography and Ecosystem Science, University of Lund, Sölvegatan 12, S-223 62 Lund, Sweden. Report series started 1985. The complete list and electronic versions are also electronic available at the LUP student papers (www.nateko.lu.se/masterthesis) and through the Geo-library (www.geobib.lu.se)

245 Linnea Jonsson (2012). Impacts of climate change on Pedunculate oak and Phytophthora activity in north and central Europe

246 Ulrika Belsing (2012) Arktis och Antarktis föränderliga havsistäcken

247 Anna Lindstein (2012) Riskområden för erosion och näringsläckage i Segeåns avrinningsområde

248 Bodil Englund (2012) Klimatanpassningsarbete kring stigande havsnivåer i Kalmar läns kustkommuner

249 Alexandra Dicander (2012) GIS-baserad översvämningskartering i Segeåns avrinningsområde

250 Johannes Jonsson (2012) Defining phenology events with digital repeat photography

251 Joel Lilljebjörn (2012) Flygbildsbaserad skyddszonsinventering vid Segeå

252 Camilla Persson (2012) Beräkning av glaciärers massbalans – En metodanalys med fjärranalys och jämviktslinjehöjd över Storglaciären

253 Rebecka Nilsson (2012) Torkan i Australien 2002-2010 Analys av möjliga orsaker och effekter

254 Ning Zhang (2012) Automated plane detection and extraction from airborne laser scanning data of dense urban areas

255 Bawar Tahir (2012) Comparison of the water balance of two forest stands using the BROOK90 model

256 Shubhangi Lamba (2012) Estimating contemporary methane emissions from tropical wetlands using multiple modelling approaches

257 Mohammed S. Alwesabi (2012) MODIS NDVI satellite data for assessing drought in Somalia during the period 2000-2011

258 Christine Walsh (2012) Aerosol light absorption measurement techniques:

A comparison of methods from field data and laboratory experimentation

259 Jole Forsmoo (2012) Desertification in China, causes and preventive actions in modern time

260 Min Wang (2012) Seasonal and inter-annual variability of soil respiration at Skyttorp, a Swedish boreal forest

261 Erica Perming (2012) Nitrogen Footprint vs. Life Cycle Impact Assessment methods – A comparison of the methods in a case study.

262 Sarah Loudin (2012) The response of European forests to the change in summer temperatures: a comparison between normal and warm years, from 1996 to 2006

263 Peng Wang (2012) Web-based public participation GIS application – a case study on flood emergency management

264 Minyi Pan (2012) Uncertainty and Sensitivity Analysis in Soil Strata Model Generation for Ground Settlement Risk Evaluation

265 Mohamed Ahmed (2012) Significance of soil moisture on vegetation greenness in the African Sahel from 1982 to 2008

266 Iurii Shendryk (2013) Integration of LiDAR data and satellite imagery for biomass estimation in conifer-dominated forest

267 Kristian Morin (2013) Mapping moth induced birch forest damage in northern Sweden, with MODIS satellite data

268 Ylva Persson (2013) Refining fuel loads in LPJ-GUESS-SPITFIRE for wet-dry areas - with an emphasis on Kruger National Park in South Africa

269 Md. Ahsan Mozaffar (2013) Biogenic volatile organic compound emissions from Willow trees

270 Lingrui Qi (2013) Urban land expansion model based on SLEUTH, a case study in Dongguan City, China

271 Hasan Mohammed Hameed (2013) Water harvesting in Erbil Governorate, Kurdistan region, Iraq - Detection of suitable sites by using Geographic

Information System and Remote Sensing

272 Fredrik Alström (2013) Effekter av en havsnivåhöjning kring Falsterbohalvön.

273 Lovisa Dahlquist (2013) Miljöeffekter av jordbruksinvesteringar i Etiopien

274 Sebastian Andersson Hylander (2013) Ekosystemtjänster i svenska agroforestrysystem

275 Vlad Pirvulescu (2013) Application of the eddy-covariance method under the canopy at a boreal forest site in central Sweden

276 Malin Broberg (2013) Emissions of biogenic volatile organic compounds in a Salix biofuel plantation – field study in Grästorp (Sweden)

277 Linn Renström (2013) Flygbildsbaserad förändringsstudie inom skyddszoner längs vattendrag

278 Josefin Methi Sundell (2013) Skötseleffekter av miljöersättningen för natur- och kulturmiljöer i odlingslandskapets småbiotoper

279 Kristín Agustsdottír (2013) Fishing from Space: Mackerel fishing in Icelandic waters and correlation with satellite variables

280 Cristián Escobar Avaria (2013) Simulating current regional pattern and composition of Chilean native forests using a dynamic ecosystem model

281 Martin Nilsson (2013) Comparison of MODIS-Algorithms for Estimating Gross Primary Production from Satellite Data in semi-arid Africa

282 Victor Strevens Bolmgren (2013) The Road to Happiness – A Spatial Study of Accessibility and Well-Being in Hambantota, Sri Lanka

283 Amelie Lindgren (2013) Spatiotemporal variations of net methane emissions and its causes across an ombrotrophic peatland - A site study from Southern Sweden

284 Elisabeth Vogel (2013) The temporal and spatial variability of soil respiration in boreal forests - A case study of Norunda forest, Central Sweden

285 Cansu Karsili (2013) Calculation of past and present water availability in the Mediterranean region and future estimates according to the Thornthwaite water-balance model

286 Elise Palm (2013) Finding a method for simplified biomass measurements on Sahelian grasslands

287 Manon Marcon (2013) Analysis of biodiversity spatial patterns across multiple taxa, in Sweden

288 Emma Li Johansson (2013) A multi-scale analysis of biofuel-related land acquisitions in Tanzania - with focus on Sweden as an investor

289 Dipa Paul Chowdhury (2013) Centennial and Millennial climate-carbon cycle feedback analysis for future anthropogenic climate change

290 Zhiyong Qi (2013) Geovisualization using HTML5 - A case study to improve animations of historical geographic data

291 Boyi Jiang (2013) GIS-based time series study of soil erosion risk using the Revised Universal Soil Loss Equation (RUSLE) model in a micro-catchment on Mount Elgon, Uganda

292 Sabina Berntsson & Josefin Winberg (2013) The influence of water availability on land cover and tree functionality in a small-holder farming system. A minor field study in Trans Nzoia County, NW Kenya

293 Camilla Blixt (2013) Vattenkvalitet - En fältstudie av skånska Säbybäcken

294 Mattias Spångmyr (2014) Development of an Open-Source Mobile Application for Emergency Data Collection

295 **Hammad Javid (2013) Snowmelt and Runoff Assessment of Talas River Basin Using Remote Sensing Approach**

296 Kirstine Skov (2014) Spatiotemporal variability in methane emission from an Arctic fen over a growing season – dynamics and driving factors

297 Sandra Persson (2014) Estimating leaf area index from satellite data in deciduous forests of southern Sweden

298 Ludvig Forslund (2014) Using digital repeat photography for monitoring the regrowth of a clear-cut area

299 Julia Jacobsson (2014) The Suitability of Using Landsat TM-5 Images for Estimating Chromophoric Dissolved Organic Matter in Subarctic Lakes

300 Johan Westin (2014) Remote sensing of deforestation along the trans-Amazonian highway

301 Sean Demet (2014) Modeling the evolution of wildfire: an analysis of short term wildfire events and their relationship to meteorological variables